Diss. ETH N° 18'192

Laser-Induced Forward Transfer for the Fabrication of Patterned Organic Light-Emitting Diodes

A dissertation submitted to

ETH Zurich

for the degree of

Doctor of Sciences

presented by

Romain Fardel

Master of Science en Génie chimique et biologique,
Ecole Polytechnique Fédérale de Lausanne

born 10.05.1982

citizen of Mutrux, Vaud

accepted on the recommandation of

Prof. Dr Alexander Wokaun, examiner
Prof. Dr Detlef Günther, co-examiner
PD Dr Thomas Lippert, co-examiner

2009

Acknowledgements

Contents

Abstract

The use of organic compounds as active materials in flat panel displays represents the next generation technology in the field, enabling an improved image quality, a reduced power consumption and the ability to build flexible displays. This work presents the developement of a transfer technique based on laser ablation which is aimed at the deposition of organic light-emitting diode (OLED) pixels as the building block of displays based on organic materials.

The deposition technique is based on LIFT (laser-induced forward transfer), whose working principle involves a transparent substrate coated with the material to transfer. The material is irradiated through the substrate by a high power laser pulse, which triggers the removal and ejection of the material from the substrate. The ejected material is then collected onto a receiver substrate placed in front of the donor film. In this way, precise patterns defined by the shape of the laser beam can be transferred.

Direct irradiation of the transfer material is not admissible for sensitive compounds, therefore a modification of the technique was introduced to solve this limitation. The modification involves the use of a sacrificial layer of a triazene polymer, which has been specifically designed for laser ablation in the ultraviolet region. The triazene layer is coated between the substrate and the transfer material, and upon irradiation, it absorbs the laser pulse, decomposes into gaseous products and propels the sensitive materials onto the receiver substrate, while protecting them from irradiation.

In this work, the application of the triazene polymer as sacrificial layer for LIFT has been studied with the goal of transferring functional OLED pixels.

Laser ablation of the triazene layer has been investigated over a broad thickness range and reveals that a dramatic increase of the laser energy density is required to ablate very thin films. This result is confirmed by theroretical modelling, which shows that heat diffusion into the substrate as well as the reduced absorption length play a crucial role for the ablation of very thin films.

Ablation of the triazene layer from the back side has been investigated by time-resolved shadowgraphy. The ejection of a flyer of undecomposed polymer was observed, which appears when the laser fluence is not sufficient to ablate the complete layer. An analysis of the trajectories of the flyer and the shock wave created by the ablation was performed and allowed to estimate the energy balance of the process.

Back side ablation of a triazene/metal film produced the ejection of a metal flyer, whose

stability in flight can be improved when the flyer contains a layer of undecomposed triazene polymer. The stabilisation is provided by the composite structure of metal/polymer film. The ejection of a flyer from a triazene/metal/luminescent polymer film, selected as building block of an OLED pixel, shows an increased stability of the flyer as well, thus confirming the effect of a polymer layer on the metal flyer.

The transfer was investigated with different separation distances between the donor and the receiver substrates and shows that close contact between the substrates is the most favourable condition for a successful transfer. A very good deposition of metal/luminescent polymer pixels was achieved with this configuration.

The transfer of pixels across a gap reveals an additional effect that complicates the system. The shock wave created by ablation is reflected from the receiver substrate and may cause the destruction of the flyer. Transfer studies in vaccum showed that the shock wave can be eliminated but that the flyer speed increases substantially, leading to the desintegration of the flyer upon impact with the receiver substrate.

Finally, the successful transfer of an OLED building block is demonstrated. The transferred pixels are fully functional and exhibit properties comparable to devices prepared by classical techniques. These results show that sensitive materials can be transferred with the LIFT technique using a triazene polymer as sacrifical layer, without altering the functional properties of the materials. This work suggests that LIFT is a possible industrial process for the deposition of organic light-emitting diode pixels.

Zusammenfassung

Die Verwendung organischer Verbindungen als Aktivschichten für die nächste Generation von Flachbildschirmen ermöglicht eine verbesserte Bildqualität bei vermindertem Stromverbrauch sowie die Herstellung flexibler Bildschirme. In dieser Arbeit wird die Entwicklung einer neuen, auf Laserablation basierenden Übertragstechnik vorgestellt, deren Ziel die Deposition von Pixeln aus organischen Leuchtdioden (OLED) als Baublöcke für organische Bildschirme ist.

Diese Übertragstechnik beruht auf LIFT (*laser-induced forward transfer*), wobei ein transparentes Substrat zunächst mit dem zu transferierenden Material beschichtet wird. Dann wird diese Materialschicht durch das Substrat mit einem Hochleistungslaser-Puls bestrahlt, wodurch das Material herausgeschleudert wird. Das beschleunigte Material trifft auf ein dem Donorsubstrat gegenüberliegendes Empfängersubstrat auf. So lassen sich auf präzise Art Muster übertragen, deren Form dem Laserstrahl entspricht.

Um eine für sensitive Materialien unzumutbare direkte Bestrahlung zu vermeiden wurde eine Änderung der Technik eingeführt, deren Prinzip auf der Ablation einer Triazenpolymer-Opferschicht beruht, die sich zwischen der Materialschicht und dem Substrat befindet. Das Triazenpolymer wurde spezifisch für die Ultraviolett-Laserablation entwickelt und wird nach Absorption des Laserpulses in gasförmige Produkte zersetzt. Diese katapultieren die darüberliegende Materialschicht auf das Empfängersubstrat während die Materialschicht vor direkter Lasereinwirkung abgeschirmt wird.

In dieser Arbeit wurde die Anwendung eines Triazenpolymers als Opferschicht für LIFT untersucht, mit dem Hauptziel, OLED-Pixels unter Erhaltung der Funktion zu übertragen.

Die Laserablation des Triazenpolymers wurde für einen breiten Schichtdickenbereich untersucht, wobei sich zeigte, dass die Ablation sehr dünner Filme eine erhöte Laser-Energiedichte benötigt. Dies wurde mit Hilfe eines dafür entwickelten Modells bestätigt, das den starken Einfluss der Wärmediffusion ins Substrat sowie der reduzierten Eindrigstiefe des Laserlichtes auf die Ablation sehr dünner Schichten beweist.

Die Ablation des Triazenpolymers von der Rückseite wurde mittels eines zeitaufgelösten Schattenvisualisierungsverfahren (*shadowgraphy*) untersucht. Die Untersuchungen zeigen, dass ein Materialpixel aus Triazenpolymer herausgechleudert wird, wenn die Laser-Fluence ungenügend für eine vollständige Zersetzung des Filmes ist. Die Analyse der Flugbahn des Pixels und der bei der Ablation ausgelösten Schockwelle ermöglichte es, ein

Energiebilanz für dieses System abzuschätzen.

Bei der Ablation eines zweischichtigen Films aus Triazenpolymer und Metall wird ebenfalls ein Metallpixel herausgeschleudert, dessen Flugstabilität verbessert werden kann, wenn der Pixel noch eine Schicht von unzersetztem Triazenpolymer enthält. Diese Stabilisierung ist auf die Ausbildung eines zweischichtigen Kompositenfilms zurückzuführen. Das Herausschleudern eines dreischichtigen Films aus Triazenpolymer, Metall und Leuchtpolymer ist ebenfalls untersucht worden, und zeigt eine verbesserte Stabilität des Pixels, was den stabilisierenden Einfluss der Polymerschicht auf den Metallpixel bestätigt.

Materialübertragung wurde mit verschiedenen Abständen zwischen Donor- und Empfängersubstrat untersucht und zeigt, dass der beste Übertrag beim direkten Kontakt zwischen beiden Substraten stattfindet. Unter diesen Bedigungen wurde eine sehr gute Deposition von Metall-Leuchpolymer-Doppelschichten erreicht.

Die Pixelübertragung mit einem Abstand zwichen den Substraten hat zur Entdeckung geführt, dass die ausgelöste Schockwelle am Empfängersubstrat reflektiert wird und den Materialpixel zerstören kann, wenn die Schockwelle auf ihn trifft. Der Übertrag wurde auch unter Vakuum studiert und zeigt, dass die Schockwelle zwar eliminiert ist, aber dass der ungebremste Pixel sehr hohe Geschwindigkeiten erreicht, was seine unmittelbare Zerstörung beim Kontakt mit dem Empfängersubstrat verursacht.

Schliesslich wurde der erfolreiche Übertrag von OLED-Bauelementen demonstriert. Die übertragenen Pixel weisen vergleichbare Eigenschaften wie Leuchtdioden auf, die mit herkömmlichen Methoden hergestellt worden sind. Diese Ergebnisse beweisen, dass die auf einer Triazenpolymer-Opferschicht beruhende LIFT-Technik geeignet ist, um empfindliche Materialien zu übertragen, ohne ihre funktionellen Eigenschaften zu verändern. Die Ergebnisse dieser Arbeit weisen darauf hin, dass eine mögliche industrielle Anwendung der LIFT-Technik für die Herstellung von OLED-Pixel denkbar ist.

Chapter 1

Introduction

1.1 Organic electronics

Electronic devices find innumerable applications in our lifes, ensuring fast and efficient support in all human activites going from work to leisure. As of today, the active components in transistors, diodes or solar cells are made of inorganic materials, while organics, mostly polymers, are used as insulating packaging materials and for mechanical parts, housings or as dye to bring colours to our world. Only recently, organic semiconducting materials have been developped for optoelectronic applications and have just entered the display market. In this chapter, basic characteristics of organic semiconductors and their applications in organic electronics are reviewed.

1.1.1 Overview

Organic materials, in particular polymers, are known to be very good electrical insulators. However, a certain class of small molecules and polymers exhibit semiconductive and in some cases even metallic behaviour.

Research on semiconducting polymers was initially directed to develop and understand electrical conductivity in these materials [1]. Polyanilines were discovered more than hundred years ago and were initially used as dyestuff (aniline black). Today this material is applied as conductive electrodes in numerous applications. The field of intrinsically conductive polymers got a large impact from the understanding and theoretical description of polyacetylene which led to the Nobel prize of chemistry in 2000 [2].

Conversely, the early focus on small molecules was clearly directed towards the developement of dye or dyestuff [3] or e.g. for the photographic industry [4]. In the middle of last century, the physics of molecular single crystals emerged as a major topic in this field [5]. For the first time, metallic conductivity was found in mixed moelcular single crystals, so-called charge transfer salts [6]. Only some decades ago, the potential of using thin organic films for optoelectronic application was fully recognised. Both polymer

and small molecules perform in a similar way as light emitters, light absorbers or charge transport layers.

The origin of the semiconductive behaviour is based on the partial overlap of the delocalised π-orbitals between neighbouring molecules. The electronic structure of polyacetylene is shown in Figure 1.1 to illustrate this electronic system.
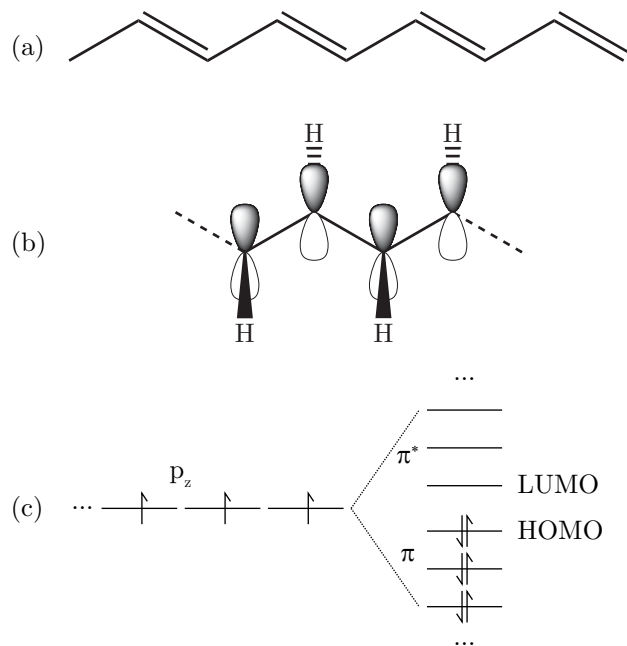
Figure 1.1 Polyacetylene: (a) chemical structure, (b) p_z atomic orbitals perpendicular to the molecule plane, (c) energy levels of the π molecular orbitals, showing the HOMO and the LUMO.

The sp^2 orbitals of the carbon atom form σ bonds with the two neighbouring carbons and one hydrogen. The remaining p_z orbitals, containing one electron each, combine together to form bonding and antibonding molecular orbitals (π and π^* respectively), which are delocalised over the conjugation length. The number of π orbitals is equal to the number of carbon atoms in the conjugated chain.

In the ground state, the electrons fill the orbitals in such a way to minimise the total energy of the molecule. The two orbitals at the limit of electron filling, so-called frontier orbitals, are of particular interest. The highest level filled with electrons is the *HOMO* (highest occupied molecular orbital) while the lowest empty level is the *LUMO* (lowest unoccupied molecular orbital). These two orbitals play an important role for the optoelectronic properties of the molecule, because the electronic transition of the lowest energy occurs then between the HOMO and the LUMO. These levels also determine the electron accepting or electron donating properties since the HOMO corresponds to the highest oxidation potential, while the LUMO relates to the highest reduction potential.

In solids, the molecules interact weakly between each other due to van der Waals forces, inducing a weak overlap of the π orbitals between neighbouring molecules. The

respective overlap of the HOMO and LUMO determines the charge carrier mobility of holes and electrons, respectively. For instance, when an electron is withdrawn from the HOMO, a positve charge or *hole* is created (see Figure 1.2), that can be transported through the organic material.
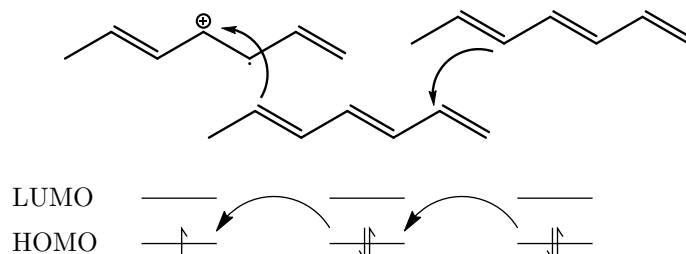
Figure 1.2 Positive charge carrier transport in polyacetylene: the weak overlap of the HOMO allows charge hopping between the molecules.

In disordered materials, as in polymers, this hole can be transported through the material by *hopping* from one conjugated chain to another. The process shown in Figure 1.2 corresponds to a positive type conduction, or hole transport. Negative charge transport is possible in the same way by hopping of an additional electron between the LUMO levels. In this way, a "two-stages" conductor is created, where current can flow through the HOMO and the LUMO. This essential property can be used in electronic devices, as shown in the following section.

1.1.2   Organic light-emitting diodes

Light-emitting diodes (LED) are devices converting electricity into light. They differentiate from thermal light sources by their ability to convert directly the electrical energy into light and do not rely on incandescence. For this reason, these "cold" light sources can now reach luminous efficiencies of 100 lm/W [7]. Organic molecules, and among them conjugated polymers, can be used as the light-emitting material for building LED, which are then called *organic light-emitting diodes* (OLED). The term OLED encompasses all light-emitting devices made of small organic molecules, while diodes made of polymers are commonly called PLED (polymer LED).

1.1.2.1   Principle

In the simplest device, a luminescent material is sandwiched between an anode and a cathode, and a voltage bias is applied between the electrodes. The scheme of such an OLED is shown in Figure 1.3 (a). The working principle can be understood with the help of the corresponding energy diagram (b), where the electron energy is shown on the vertical axis.
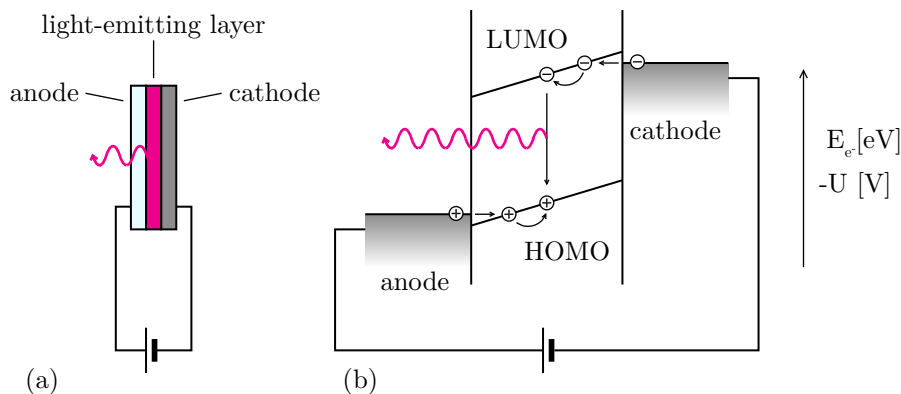
Figure 1.3 Schematics of an OLED: (a) device architecture and (b) energy diagram.

Positive charges are injected from the anode to the HOMO and start to migrate towards the cathode under the action of the electric field. In the same way, electrons are injected at the cathode into the LUMO and migrate towards the anode. Electrons and holes eventually meet and recombine to form a neutral species, the so-called *exciton*. This electronically excited state is localised on one or a few molecules and has a very short lifetime. In the most favourable case for OLED the exciton decays radiatively. The excited state of the molecule or of the molecular complex is converted to its ground state by releasing a photon of a given energy. To a first approximation, this energy ΔE corresponds to the difference between the LUMO and the HOMO levels, defining the wavelength λ of the emitted photon by

$$\Delta E = \frac{\mathrm{h}c}{\lambda}, \tag{1.1}$$

where h is the Planck constant and c the speed of light in vacuum. The emission of light from an excited molecular state is *luminescence*. When the creation of this excited state is achieved by charge injection, it is called *electroluminescence*, in contrast to *photoluminescence*, where excitation is induced by light absorption.

The charge injection in the active layer is realised by the electrodes. Materials with a low work function, mainly metals, are used a cathode in order to get an efficient electron injection. On the opposite, the anode has to have a high work function to withdraw electrons easily. Additionally, the anode must be transparent because light has to be emitted through one of the electrodes and the cathode is usually metallic, thus opaque. Common materials fulfilling these two requirements are transparent conductive oxides, mainly tin-doped indium oxide (ITO).

For achieving a high luminous efficiency, it is essential that the charge recombination occurs in the luminescent material and not at the electrodes, where the excited states are quenched. Furthermore, there should be an equilibrium of the positive and negative

currents (i.e. currents in the HOMO and the LUMO). In practice, this is difficult to achieve by using a single organic layer and the efficiency is lowered proportionally to the excess current ending at one electrode.

One way to solve the problem was proposed in 1987 with the use of a double layer structure composed of materials with different HOMO an LUMO energy levels, respectively [8]. The principle is shown in Figure 1.4.
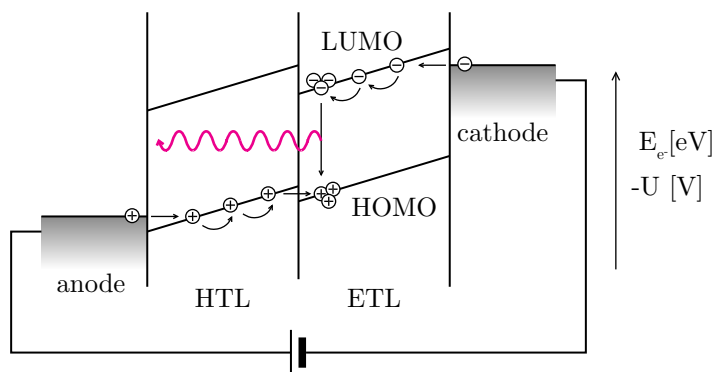
Figure 1.4 Working principle of an optimised OLED with 2 active layers, the hole transporting layer (HTL) and the electron transporting layer (ETL). In this case the ETL is luminescent.

The layer on the left-hand side transports the positive charges and blocks the electrons, therefore it is called the *hole transporting layer* (HTL). The right-hand side layer, doing the opposite, is the *electron transporting layer* (ETL). The HTL and ETL are not conductive, but can transport charges when these are injected. Charges are transported to the organic heterointerface where they are blocked by the high energy barrier for hopping. Due to this, holes and electrons accumulate at the interface of the two layers and have a enhanced probability to meet. Recombination occurs in one of the two layers, depending on the materials. In the case shown in Figure 1.4, the luminescent material is the ETL.

A further increase in effiency is achieved by adding a specific layer for charge recombination and emission between the transporting layers, as well as additional blocking layers and layers for helping charge injection. State-of-the-art devices are made of up to 7 layers.

1.1.2.2 Materials

Materials suitable for OLED should combine several properties. They must show a decent charge carrier mobility and have a high quantum yield for light emission. Moreover, the layers have to be thin, because the low charge carrier mobility must be compensated by high electric fields, reached only with thin layers.

The first observation of electroluminescence in organic materials was reported for anthracene single crystals in the fifties. Since then, many materials have been investigated, especially small organic molecules. One of the most important system is the combination of tris-(8-hydroxyquinoline) aluminum (Alq$_3$, as ETL and emission layer) and triphenyl diamine (TPD, as HTL), which is still an important constituent of state-of-the-art OLED.

The first report of a conjugated polymer exhibiting electroluminsescence occured in 1990 for poly[p-phenylene-vinylene] (PPV), shown in Figure 1.5, which emits light in the green-yellow region [9].

PPV   MEH-PPV
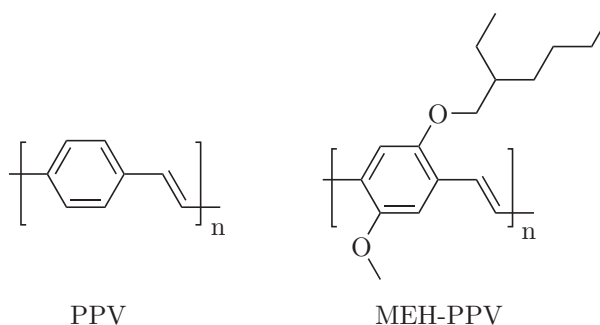
Figure 1.5 Chemical structure of two luminescent conjugated polymers.

Today, several PPV derivatives are used as luminescent layers in diodes, for example MEH-PPV (poly[2-methoxy-5-(2-ethylhexyloxy)-1,4-phenylenevinylene]), emitting orange light (see Figure 1.5). Copolymers of PPV have shown high efficiencies as well [10].

Apart form the emitting polymers, other conjugated polymers are used in OLED as injection and transporting layers. The best known example is PEDOT (poly[ethylenedioxythiophene]) doped with polystyrenesulfonic acid (PSS) (Figure 1.6).
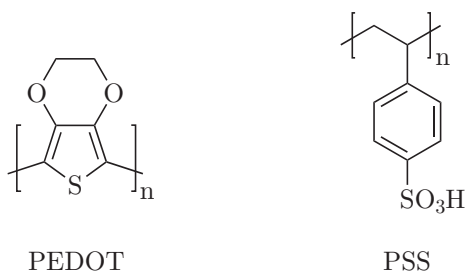
PEDOT   PSS

Figure 1.6 Chemical structure of PEDOT:PSS

This material is generally used as hole buffer layer between the anode and the luminescent polymer. Since its conductivity is remarkably high, it is sometimes used as electrode, instead of a transparent conductive oxide.

1.1.2.3   Applications

Organic light-emitting diodes find applications in two main domains. First, they can be used as efficient sources for lighting. In this case, large uniform areas are involved. But the most interesting application is as building blocks for screen pixels. Displays made of OLED offer several advantages over the dominating liquid crystal display (LCD) technology:

Power consumption The pixels are self emitting and do not need backlight. Since the diodes only use power when emission is required, the display uses less power, which is even more diminshed while displaying dark colours. Furthermore, the efficiency of the individual red, green and blue diodes reaches the one of fluorescence tubes or inorganic LED used for the backlight of LCD displays.

Brightness The brightness reached with OLED pixels is higher than with LCD. Moreover, the contrast ratio in greatly enhanced because black pixels are turned off and do not have residual backlight.

Thickness The active layers have a total thickness of the order of less than a micrometer and no backlighting is required, therefore the display can be made very thin. The actual thickness of the device is determined by the substrate and the encapsulation layers, and not by the active layers.

Flexibility The use of polymeric materials for the active layers and the substrate allows to build flexible displays, opening new possibilities of applications, e.g. foldable or rollable displays. The driving electronic (active matrix) is still in amorphous silicon, but could be replaced by organics in the future.

Cost Although this argument is not true yet, the replacement of the expensive and energy-consuming silicon purification process will lead to a considerable cost reduction. Also, cost-efficient fabrication processes may be applied.

1.1.3   Other organic devices

Besides light-emitting diodes, there are two other important applications for organic semi-conductors, which are presented below.

1.1.3.1   Solar cells

A solar cell, or photovoltaic cell, is a device that converts light into electricity. The architecture of a solar cell is similar to that of an electroluminsescent diode, except that the working principle is almost time-reversed. Also the device is operated in a low voltage range, where the built-in field produced by the anode and the cathode drives the current in the opposite direction when compared to the current flow in OLED. A photon is captured

in the absorbing layer and creates an exciton, by promoting an electron in the LUMO and leaving a hole in the HOMO. The exciton is separated at the organic heterointerface and is transported to the anode and the cathode by drift and diffusion processes. The charge is then injected in the external circuit and the cell produces current [11].

A complete field of research is devoted to the development of organic solar cells, addressing the specific issues encountered, e.g. exciton separation, formation of nanoscopic biphasic film structures, near-infrared absorption or stability under light.

1.1.3.2   Thin film transistors

A transistor (from *trans*fer res*istor*) is an electronic switch in which the resistance between two electrodes is controlled by an external voltage [12]. This voltage is applied at an additional electrode, therefore the device has three terminals. Transistors are the most common electronic devices and the key components of all integrated circuits. The working principle of an organic thin film transistor is shown in Figure 1.7 [13].
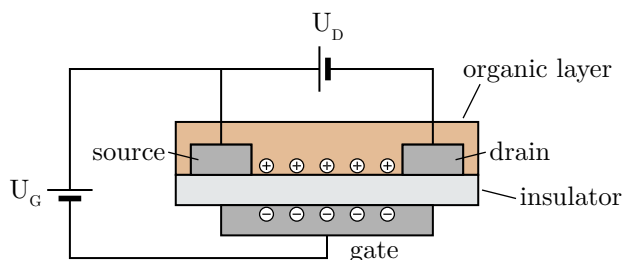
Figure 1.7 Scheme of an organic field-effect transistor. U_G ist the gate voltage and U_D the driving voltage.

When a voltage U_G is applied between the source and the gate, the interface between the insulating materials and the semiconducting polymer acts as a capacitor and gets charged. The increased charge carrier concentration in the organic layer enhances its conductivity. Upon application of a voltage U_D between the source and the drain, current can flow in the so-created conductive pathway.

The same advantages as for OLED regarding the cost and flexibility apply to organic transistors. Due to the inherent low electron and hole mobility, organic transistors will probably never be used in a computer chip. However, the mobility in organic transistor may equal or even exceed the mobility in amorphous silicon. Therefore, efforts focus on applying these devices for active matrix driving schemes. A typical application is as active matrix in an OLED display.

1.1.4   Fabrication methods

The breakthrough of the OLED display technology will depend on the ability to find efficient materials for the active layer and determine the best architecture for a high

efficiency, but also on the ability to manufacture the desired device architecture. The production of an OLED display requires at first the capability to deposit on a substrate the architecture described above in the form of small picture elements (pixels). The rest of the fabrication includes the electronic contacting and addressing circuit (active matrix) as well as the encapsulation to protect the materials from the ambient atmosphere. The issue of pixels deposition is addressed more specifically in this section.

1.1.4.1 Requirements

The deposition method for OLED pixels has to comply with the following requirements :

Lateral patterning Pixels with a limited size are required. A standard 72 dots per inch resolution implies a 350 µm pixel size, which is divided into three colours. Additionally the active matrix requires typically 60% of the surface area. Therefore, a feature size of 50–100 µm is needed.

Multi-layer ability As shown above, a multi-layer stack of materials is needed for highly efficient devices.

Versatile method The technique should be applicable to a broad range of materials to ensure that state-of-the-art compounds are processible.

Mild conditions The materials to process are mostly sensitive to heat and light. Thermal decomposition ofter occurs between 200 and 300 °C. Thermal annealing at a lower temperature induces crystallisation or aggregation which can have numerous effects, such as roughening of the film or alteration of the optical and electrical properties. Light exposure degrades the chemical structure of the materials, especially at high photon energies where bond breaking can occur. Therefore, heating and direct irradiation should be reduced to the minimum. Additionally, the materials are sensitive to oxygen and have to be handled in an inert atmosphere to avoid oxidation.

1.1.4.2 Techniques

Several techniques exists for depositing OLED materials, each with their advantages and drawbacks. An overview is given here.

Spin coating: The most simple method used for thin film deposition is spin coating. The material to deposit is dissolved in a solvent and dispensed onto a substrate, which is then spinned. Upon spinning, the solution spreads into a thin layer and the solvent evaporates, resulting in a very homogeneous film. It requires no expensive equipment and small substrate areas can easily be coated. The problem of this method is obvious: no lateral patterning can be achieved. Moreover, as a solution-based technique, spin coating

has another main drawback regarding solvent compatiblity. Two layers with a similar solvent cannot be deposited successively because the application of the second dissolves the first one and causes mixing of the layers. This is a general problem for all wet processing techniques. Nevertheless, spin coating is largely used in research laboratories and for depositing layers which do not need patterning, for example a common electrode. It is very useful as well for producing precursor films for other patterning techniques.

Mask evaporation: Small molecules can be evaporated in vaccum and deposited onto a substrate. A mask between the source and the target allows patterning by physically blocking the deposition at undesired locations. Evaporation is commonly used for metal and small organic molecules. The technique is ideal for achieving multi-layer stacks, but it requires compounds with a low evaporation temperature in order to withstand heating. Therefore, polymers and certain small molecules are excluded form the applicable range, because they decompose before boiling or sublimating.

Inkjet printing: Solutions found in the publishing industry have inspired the developement of deposition techniques for OLED pixels. Inkjet printing, used in personal desktop printers, is an example. The ink is replaced by a solution of the material to deposit and is printed onto the substrate. Due to an extensive developement for the general public, the technology is fully mature and reliable. The main disadvantage has been already mentioned for spin coating: the wet processing limits the materials and the number of layers that can be deposited. Moreover, the poorly controllable shape of the drop deposition limits the precision of the structures produced by jetting methods.

Screen printing: Screen printing is also coming from the printing industry, where it is called serigraphy. The solution to coat is applied trough a mesh pressed onto the substrate (see Figure 1.8). The mesh structure is reproduced in negative onto the substate [14, 15]. The technique allows a high throughput but, as inkjet printing and spin coating, it presents the disadvantages of a solution-based technique as mentioned above. Furthermore pixel resolution may not be sufficient for certain applications.
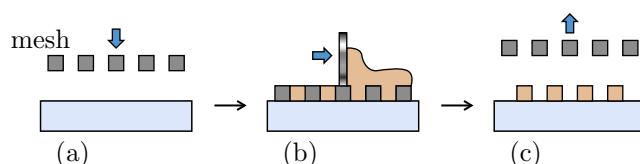
Figure 1.8 Principle of screen printing

Photolithography: The most important patterning technique in the silicon-based electronic industry is photolithography. The process is illustrated in Figure 1.9 and consists
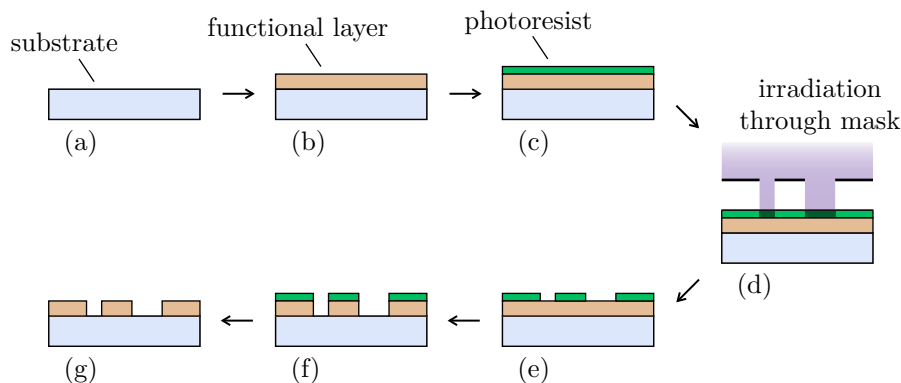
Figure 1.9 Principle of photolithography

in the following steps: the substrate (a) is coated with the functional layer (b) and then with a photoresist (c), which is a polymer designed to change its properties upon irradiation, for instance the solubility in a specific solvent. The photoresist is irradiated through a mask (d), thus defining patterns. The next step is the developing of the structure by dissolution (e). In the case of a positive resist the irradiated area becomes soluble in the developing solvent, used to reveal the pattern. The solvent is chosen so that the non-irradiated area is not dissolved. The pattern is then engraved into the functional layer by selective etching (e.g. reactive ion etching or acid etching), leaving the locations covered with resist unchanged (f). After dissolution of the resist, the final pattern is obtained (g).

While photolithography is suitable for inorganic layers, the situation is more complicated with organic materials. The process involves an irradiation and several wet steps, which may damage the organic molecules. An interesting strategy was demonstrated, involving electroactive polymers with a photodecomposible group [16]. In this case, the electroactive material plays also the role of the photoresist. The limitation comes from the availability of polymers combining two functionalities in one material, i.e. excellent light emission and photo-induced cross-linking.

Laser induced thermal imaging: Laser induced thermal imaging, or LITI, is a thermal printing technique where the OLED material is transferred from a ribbon onto the display substrate. The donor ribbon is a flexible substrate coated with a so-called *light to heat conversion* layer (carbon black), a protective interlayer and the electroactive material. The printing is realised by pressing the ribbon onto the substrate, with the OLED layer towards the substrate, and irradiating the zone to transfer through the ribbon with an infrared laser. The absorbing black carbon layer is heated by the lase pulse and triggers the delamination of the electroactive layer. After peeling off the ribbon, the luminescent material is left on the substrate at the irradiated locations.

LITI combines the dry deposition with the ability to coat a potentially broad range of materials. Moreover the method is easily up-scalable. A drawback is the necessity to have the donor ribbon in close contact with the substrate, which is critical for achieving

multi-layer patterning in successive steps. But the main disadvantage of the method is the thermal load on the transferred materials, in which a peak temperature of 350 °C is reached [17]. This is not acceptable for a lot of materials because this temperature induces irreversible alterations in the chemical structure, and therefore, in the optical and electrical properties. Finally LITI requires an absorbing layer as well as a protective interlayer. Part of these layers are also deposited together with the luminescent material, which hinders the fabrication of multi-layer structures with clearly defined interfaces.

1.1.4.3 Limitations

The techniques described above present advantages for the patterned deposition of OLED layers and are readily applied in the industry. However, none of them comply with all criteria suggested in Section 1.1.4.1. A new method combining the four basic requirements would be an important step forward for the OLED technology, since it would allow to build any arbitrary pixel architecture and to achieve high efficiencies.

In the next section, a new patterning technique fulfilling all points is described. The technique relies on laser ablation of a polymer. At first, an introduction to laser ablation is given, followed by a review of the pattern deposition techniques based on laser ablation. Finally, the new and original method which is subject of the present thesis is presented.

1.2   Laser ablation

Lasers are widely used in research and industry for their ability to deposit a high amount of energy in a short time to a precise zone of a sample. When enough energy is deposited into the material, morphological changes appear and a certain amount of material is removed from the surface. This process is called *laser ablation* and is applied in a variety of applications, among them the deposition of patterned layers, as shown below.

1.2.1   Overview

Since the invention of the first ruby laser in 1960 [18], lasers evolved from a "solution looking for a problem" to a valuable tool in research, industry and everyday life. Laser is the acronym for *Light Amplification by Stimulated Emission of Radiation*. It allows to produce a coherent light beam with a narrow bandwidth and a high brilliance by the concerted radiative relaxation of an excited medium. These properties give the laser a unique advantage for specific applications, largely compensating the increase in complexity and cost. The high coherence is used for sensing and ranging applications, e.g. from speed radars on the road to laser lunar ranging [19] or spaceborne interferometer satellites [20]. The spectral purity is used for high-resolution spectroscopy, e.g. atmospheric gas monitoring [21]. Lasers are also widely used in consumer electronic devices (optical storage) and communications networks.

Lasers can be continuous wave, as in the above-cited examples, or pulsed. In the latter, very short pulses enable time-resolved probing and spectroscopy at extreme time scales (hundreds of attoseconds are reached [22]), and due to this, correspondingly high peak power is achieved as well. If the power is sufficiently high, a laser pulse impinging onto a material sample can induce an explosive photon-matter interaction, commonly called laser ablation [23]. It was early used for materials processing, at first for heating and burning, then drilling and cutting. Progressively, the tool refined to achieve selective ablation, as demonstrated with the "laser eraser", where printed ink letters were removed from a paper sheet without damaging it [24].

Laser ablation relies on the interaction between the laser pulse and the material. The basic requirement for laser ablation is to concentrate enough power in a volume of material. This is best achieved when the material absorbs strongly at the laser wavelength. Weakly absorbing materials are also susceptible to undergo ablation but at a much higher laser power. Even transparent materials can be ablated by creating absorbing defects under a high power pulse, or by non-linear absorption. In the latter cases, a femtosecond pulse length is generally needed.

1.2.2   Laser ablation of polymers

Laser ablation for precision applications requires materials which can be processed with minimal impact on the surroundings. While virtually all materials are eligible for laser ablation, they differ by the minimum fluence (energy density) needed to achieve material removal. This minimum fluence is called threshold fluence (Φ_{th}). Materials with a low threshold fluence are preferred for applications requiring gentle processing because less energy is transmitted to the system and less overheating and irradiation take place. Low fluence processing bears as well economic advantages due to the cost of laser photons. The most suitable materials in this view are polymers. They also have a low thermal conductivity, which limits heat transfer to the surrounding zone.

The first study of laser ablation on polymers was reported in 1982 by Srinivasan [25] on polyethylene terephtalate and Kawamura [26] on polymethyl methacrylate. Since then, ablation of polymers developed into a variety of applications, ranging from dry photolithography to ophtalmology.

1.2.2.1   Specifically designed polymers

The next step of improvement was reached with the design of materials specifically for laser ablation. The UV region of the spectrum is interesting for laser ablation, because it allows to involve photochemical degradation in the process, which is intrisically more precise than purely thermal decomposition. The short wavelength is also an advantage for precision processing operating at the diffraction limit. In the UV range, the XeCl excimer laser is the most common laser in industry, mainly for gas handling and efficiency

reasons. This laser emits at 308 nm and suitable ablation materials should have a high absorption around this wavelength.

The triazene (–N=N–N(R)–) and pentazadiene (–N=N–N(R)–N=N–) chromophores were chosen for their high absorption around 300 nm and were incorporated into the polymer main chain, yielding several related compounds [27]. The best candidate up to now is an aryltriazene polymer, shown in Figure 1.10.
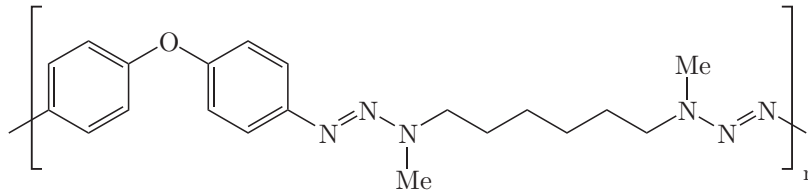
Figure 1.10 Chemical structure of the triazene polymer

It showed very high ablation rates per pulse and the lowest threshold fluence among other triazene-containing poymers, but also compared to comercial polymers used for laser ablation, such as polyimides, polyesters [28, 29] or polyurethanes [30, 31].

1.2.2.2   Ablation mechanism

While the use of laser ablation is well established, several aspects of the fundamental understanding of the process are still subject to controversy. The difficulty of modelling laser ablation of polymers is related to the complex nature of the materials (large molecules, possible reactive pathways, etc.), in comparison with metals for instance. Several models have been proposed for ablation of polymers, which are reviewed in [32, 33], but up to now, none of the models is able to describe completely the experimental observations. The different types of models may be summarised as follows.

Photochemical models   The photochemical approach supposes that the absorbed photons induce a direct bond-breaking of the polymer chain [34–38]. The basic equation is obtained from the Lambert–Bouguer's law of absorption which is expressed in terms of fluence by

$$
\begin{aligned}
\frac{\Phi}{\Phi_0} &= 10^{-ax}, \\
&= e^{-\alpha x},
\end{aligned}
\tag{1.2}
$$

where Φ is he laser fluence, a and α are the decadic and natural linear absorption coefficients, respectively, and x is the distance from the film surface. The index 0 refers to the incident value ($x = 0$). The absorbed energy density per volume element ρ_E is given by

the derivative of the absorbed fluence with respect to the distance

$$\rho_E = \frac{d(\Phi_0 - \Phi)}{dx} = \alpha \Phi_0 e^{-\alpha x}. \tag{1.3}$$

The model postulates that a minimum energy density is required for ablation to occur. The energy density decreases across the film until it reaches the threshold energy density

$$\rho_{E,th} = \alpha \Phi_0 e^{-\alpha d}. \tag{1.4}$$

The distance d is the thickness where $\rho_{E,th}$ is reached, therefore it corresponds to the ablation depth. After rearranging, the equation becomes

$$d = \frac{1}{\alpha_{\text{eff}}} \ln \frac{\Phi_0}{\Phi_{\text{th}}}, \tag{1.5}$$

where Φ_{th} is the threshold fluence given by $\rho_{E,th}/\alpha$. In practice, the absorption coeffcient calculated from Equation 1.5 differs from the linear coefficient, mainly due to transient bleaching [39, 40], incubation (permanent modification) [41, 42] and shielding of the laser beam from the ablation products. This change is reflected by an *effective* absorption coefficient α_{eff}. This model is very appropriate to describe the occurence of a sharp ablation threshold, as observed with polymers.

The model presented above supposes that the ablation occurs in one step after complete absorption of the laser pulse and can therefore be classified as a *volume* model. While Equation 1.5 is useful to describe and quantify the ablation behaviour of materials, the physical assumption behind it is not fully correct, because ablation occurs during the laser pulse already [43]. *Surface* models have been developed to take into account this effect with the introduction of a moving film-air interface [44].

Photothermal models The thermal approach postulates a rapid thermalisation of the laser energy with subsequent bond breaking [45–48]. The developed theories can be divided in volume and surface models as well. Surface models are interesting because they predict the occurence of an Arrhenius tail, i.e. an exponential increase of the ablation depth close to the threshold which is observed with gravimetric methods. This effect is not predictable with pure photochemical models. However, thermal models lack to describe the occurence of a sharp ablation threshold.

Photophysical models Models acounting for the mechanical stress have been developed as well, for instance in [49]. The effect of internal stress due to formation of small species in the bulk, as well as transient acoustic waves is taken into account. These models are generally more relevant for short pulses (ps or shorter).

Combined models   The models shown above can predict one or another aspect of the ablation of polymers, but none can describe completely the experimental observations. Some attempts have been done to describe the ablation process in a more reliable way by combining the features of both photochemical and photophysical models and creating mixed models [50]. However, until now, no fully predictive model exists for the laser ablation of polymers.

1.2.3   Applications

Although the problem of modelling is still open, a variety of applications based on laser ablation have been developed, covering now a broad field. The applications can be classified in four main domains, as shown in the diagram below:
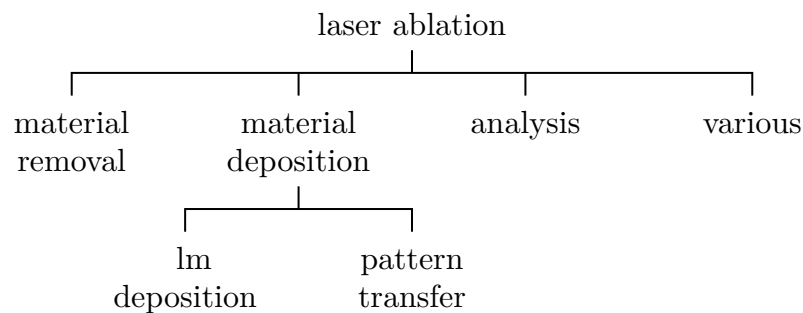
First, laser ablation achieves modification of the target, which is used for creating structures. Material modifications can be at the surface (roughening, creation of waves), or in the volume (channels, holes, micro-lenses), and are done with a high lateral and depth resolution. It offers an alternative to classical photolithography, because the pattern-drawing (exposition) and material removal (wet etching) steps are replaced by a single ablation step, where the pattern is defined and removed simultaneously.

Secondly, the ablated material can be collected onto a substrate. Depending on the conditions, films are grown on the substrate, or precise patterns are transferred. This topic is called laser deposition or laser transfer and is discussed in detail below.

Laser ablation causes removal of material from a sample, which is used for analytical purposes. The ablated *plume* (ejected cloud of material) is imaged optically, by emission spectroscopy or sent to a detector (mass spectrometry, inductively coupled plasma mass spectrometry [51–53], matrix-assisted laser desorption/ionisation - time of flight), which allows to investigate the composition of the initial target.

Finally, a fourth class of applications include plasma thruster for microsatellites, shock wave generation and others niche applications.

Materials deposition by laser ablation is now discussed in more details, starting with film deposition.

1.2.3.1 Film deposition

The material ejected from the target by laser ablation can be collected onto a receiver substrate placed in front of the target. Several techniques allow to grow films from the material ejected in the laser ablation plume. The first developed is pulsed laser deposi-
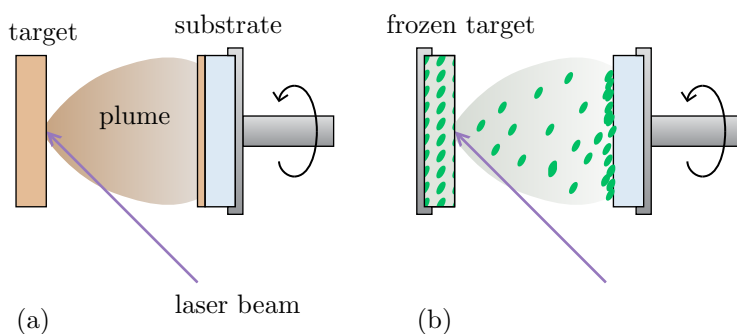
Figure 1.11 Film deposition by laser ablation: (a) PLD, (b) MAPLE.

tion (PLD), whose working principle is illustrated in Figure 1.11 (a). A material target is irradiated with a pulsed laser under reduced pressure. The material is ejected and redeposits onto a receiver substrate, placed in front of the target, at a typical distance of several centimeters. This technique allows to grow epitaxial thin films, whose composition can be tuned by using the interactions between the plume and the background gas. These interactions can be enhanced by several improvements, e.g. pulsed reactive cross-beam laser ablation [54]. PLD was initially used for inorganic materials [55–57], but recent works showed that organic thin films can be obtained as well [58–61].

However, the use of PLD is critical with sensitive compounds, because the material is directly irradiated and absorbs the laser energy. To prevent this, a derived technique was developed, called matrix-assisted pulsed laser evaporation (MAPLE). The method, shown in Figure 1.11 (b), uses a target made of a frozen solvent (the matrix) containing the material to be deposited. Upon irradiation, the solvent is evaporated and forms a plume together with the molecules of interest. The solvent molecules are evacuated by the vacuum line and, in principle, do not reach the substrate. The film grown on the substrate only contains the dry molecules previously solvated in the matrix [61,62], although recent data show that solvent molecules can be trapped in the films. The method is mainly applied to biological molecules (e.g. proteins) or sensitive organic molecules. Films of conductive polymers such as MEH-PPV [63,64] and PEDOT:PSS [65] were prepared using a free-electron laser (FEL) in the mid-infrared domain, at the resonant frequency of the solvent.

Although very useful for preparing thin films, the PLD and MAPLE technique do not conserve the spatial information from the laser impact spot and do not allow to deposit

patterns of materials, except when using a mask. However, laser-based methods allowing to do it exist as well and are presented in the following section.

1.2.3.2   Pattern deposition

Laser ablation allows to transfer precise patterns of materials, i.e. transfer of a layer from a donor to a receiver substrate while conserving the shape defined by the laser spot. The technique is called laser-induced forward transfer (LIFT) [66] and is shown in Figure 1.12. The donor substrate is prepared by coating a film onto a transparent plate. The receiver
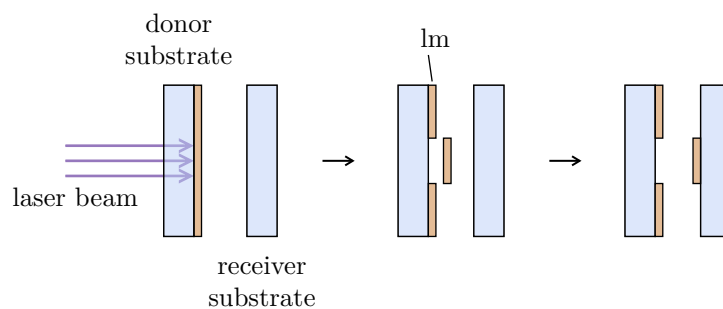
Figure 1.12 Working principle of LIFT

substrate, where the material will be deposited, is placed in front of the donor film. A shaped laser pulse hits the donor film through the substrate (from the back side) and ablates it. The material is ejected and redeposited onto the receiver substrate. The beam hits the material from the back side, in such a way that a part of the film can be ejected in a compact cloud, and be collected as well in one block. The distance is also much smaller, preventing the ablated material to spread laterally. In this way, the shape of the deposited pattern corresponds to the ablated spot, and the technique allows to write structures without masking the plume. This ability is referred to as *direct write* technology [67].

The first use of LIFT was reported in 1986 by Bohandy et al. for the deposition of copper [68]. Since, it has been applied to metals [69–72], materials for battery electrodes [73], but also to liquids containing biomolecules [74].

The main drawback of the technique is the direct laser irradiation of the material to transfer. It is often destructive for sensitive materials such as organic compounds or biological molecules. A more gentle process for achieving pattern deposition was developped from the MAPLE technique, yielding matrix-assisted pulsed laser evaporation-direct write (MAPLE-DW). The frozen target used for MAPLE is ablated from the back side and transferred in the same way as in LIFT. The technique offers the same advantages as MAPLE, namely the ability to transfer sensitive materials without direct irradiation.

MAPLE-DW has been used for transferring metal and ceramics [62, 75] as well as biological materials [76].

While adapted to sensitive materials, MAPLE-DW proceeds from molecules spread in a matrix and does not allow to conserve the morphology of the initial film, which is critical for certain applications. Though, the principle of avoiding direct irradiation can be realised with LIFT. A modification of the technique involves a two layer system comprising a *sacrificial layer* acting as an absorber and the transfer material coated on top. Upon irradiation, the sacrificial layer absorbs the laser energy and transforms it into kinetic energy for propelling the top layer. This type of approach has been reported first for the transfer of ink pixels using an aluminum absorbing layer [77]. The method was used as well to transfer biomolecules with a titanium or silver absorbing layer [78, 79]. Metal debris are then found in the transferred layer. It is not a problem in the case of biological samples, since bio-compatible metals do not interfere with the functionality.

The situation is different in the case of materials for electronic devices, because the presence of metal is a critical contamination. For this reason, this technique is unsuitable for such applications. Moreover, sacrificial layers of metal conduct heat very fast to the overlaying material, which may damage it. The problem was overcome with sacrificial layers made of polymers. The first application of an energetic polymer for LIFT was reported with the application of an additional nitrocellulose layer between the substrate and the metal absorbing layer [80]. The plastic deformation of a thick polyimide layer has been reported for the transfer of living cells as well [81].

The use of polymer specially designed for laser ablation provide a further improvement in the technique. Upon ablation, the polymer is decomposed into gaseous fragments and provides the thrust for propelling the top layer onto the receiver [82]. Furthermore, the absorbing material protects the top layer from the laser pulse and is specially designed to decompose at low fluences. Among various polymers, triazene-based polymers (TP) show the lowest ablation threshold at 308 nm and are therefore the most promising materials for this application [28, 29, 83]. Several laser ablation studies have been performed on the triazene polymer, such as mass spectroscopy of the ejected fragments [84–86] and shock wave analysis by time-resolved imaging [87]. The triazene polymer was used for molecular implantation [83], and in 2001, the first use of triazene polymer as a LIFT sacrificial layer was reported for the transfer of a PMMA film [82].

1.3 Goal of the work

1.3.1 Starting idea

As shown in Section 1.1.4, the fabrication of pixels of electroluminescent polymers for organic light-emitting diodes need a method able to overcome all the issues mentioned. On the other hand, laser-based depositon methods offer possibilities to achieve gentle transfer

of sensitive materials. The idea of the present work is is to apply the triazene-based LIFT technique to deposit functional OLED pixels. The goal is to prove the feasability of the triazene-based LIFT method for sensitive materials, to understand it and to build an OLED pixel with this technique.

1.3.2   Developement of the work

The work starts with fundamental investigations of the ablation behaviour of the triazene polymer, establishing a bridge to the data already available. The ablation of ultra thin films in the thickness range required for LIFT film are investigated. The attention is then focused to the LIFT configuration: the back side ablation of the sacrificial layer was investigated, at first alone, then coated with a top layer. The mechanism of the transfer was studied with a time resolved imaging technique, giving access to the in-flight behaviour of the tranferred material. Transfer was applied to different model materials, including metal and polymers and eventually, applied to transfer an OLED building block which was subsequently characterised.

Chapter 2

Experimentals

The experimental work can be summarised in three main parts: sample preparation, laser processing including imaging, and post-processing characterisation. The experimental methods are presented here in this order.

2.1 Samples preparation

The first step is to prepare the donor films for ablation and transfer experiments. In certain cases, the receiver substrates needed preparation as well. The preparation of the samples consists in coating one or more layers onto transparent carrier substrates.

2.1.1 Substrates

The substrate material used for laser processing must be transparent to the laser light, because the beam interacts with the triazene film through the substrate. For this reason, fused silica was used, in the form of plates of Suprasil 2 (Heraeus, Germany) cut into $25 \times 25 \times 1$ mm^3.

Other materials were used in order to investigate the influence of the substrate on the ablation threshold. The goal was to have different thermal conductivites but the same absorption coefficient. Sapphire (Stecher ceramicparts GmbH, Uetendorf, Switzerland, 1 mm thick) and polymethyl metacrylate (PMMA, Maagtechnic, Dübendorf, Switzerland, 1.2 mm thick) were used.

The substrates were cleaned prior to any deposition with a special procedure under a laminar flow hood to avoid dust as much as possible. The substrates were ultra-sonicated in successive baths of acetone, ethanol and a solution of a surfacant specially designed for cleaning optical parts (Hellmanex). The substrates were then brushed in all directions and rinced three times in the ultrasonic bath with ultrapure water (0.2 μm filtered). They were finally dried in a nitrogen flow.

2.1.2 Triazene polymer

The triazene polymer (poly[oxy-1,4-phenylene(3-methyl-1-triazene-1,3-diyl)-1,6-hexane-diyl(1-methyl-2-triazene-1,3-diyl)-1,4-phenylene], Figure 1.10) was synthesised[1] following the procedure published previously [88].

The triazene polymer was deposited by spin-coating. The polymer was dissolved overnight in a mixture of chlorobenzene and cyclohexanone (1:1 w/w) to get a 5% primary solution, which was centrifugated at 4000 rpm for 20 minutes to remove undissolved particles. Solutions with concentrations between 5% and 0.25% were obtained by dilution. The solutions were dispensed onto the substrate through a 0.45 µm filter. Spinning was done for 60 s at speeds between 1000 and 3000 rpm with a ramp of 1000 rpm/s . The films were dried after deposition either 2 hours at 50 °C or overnight at room temperature. Films with a thickness between 7 and 500 nm were obtained with this procedure.

2.1.3 OLED materials

An organic light-emitting diode (OLED) is made of at least three layers. The most important is the electroactive layer, in which charge recombination and light emission occurs. This layer has to be contacted to a current source. For this, it is sandwiched between two electrodes, whose work function have to match the HOMO and LUMO of the luminescent layer. This is the most simple architecture for building an OLED.

The goal was not to test a new device configuration and get a record-efficiency diode, but to start from a well-known system and to test the transfer method on it. Among the possible materials, MEH-PPV (poly[2-methoxy-5-(2-ethylhexyloxy)-1,4-phenylenevinylene]) was chosen because it is well-known, a lot of reference data exist on diodes based on it, and it was readily available in the laboratory. Matching cathode materials are alkali metals or alkaline earths such as cadmium or calcium. Instead aluminium was selected because calcium is highly reactive in air and would therefore complicate the process. At least one electrode must be transparent for light to be emitted. The cathode material being opaque, a transparent anode was required. A suitable anode material is tin-doped indium oxide (ITO), which is the most common material for this application.

The transfer method inverts the order of the layers between the donor and the receiver substrate. The topmost donor layer is the closest to the receiver substrate and vice-versa. For this reason, the OLED architecture has to be build in reversed order on the donor substrate. The Al cathode is deposited directly onto the triazene film, followed by the MEH-PPV layer.

Aluminium was deposited by thermal evaporation in vacuum. A Leybold Univex chamber was used for the deposition. Al was evaporated from tungsten boats at a typical rate of 0.5 nm/s under a pressure of less than 10^{-5} mbar. Practical issues with the boats limited the deposition thickness to 40 nm per source. Two sources were used

---

[1]The polymer synthesis was done by Matthias Nagel at Empa.

successively to reach 80 nm. Due to the ease of fabrication of TP/Al bilayer samples, this combination was used frequently as a simple model system for studying ablation and transfer by shadowgraphy.

MEH-PPV was deposited by spin-coating. The commercially available MEH-PPV (Aldrich, $M_n = 40$'000–70'000 g/mol) needed to be purified to obtain a good light emission and to prevent the solution from gelifying. Purification[2] was done by flash chromatography in tetrahydrofuran on a silica gel column. It was then dissolved in chlorobenzene to a 1 wt% solution and spin-coated for 120 s with a ramp of 500 rpm/s. As the solvent of the MEH-PPV dissolves the triazene layer, it was not possible to get a bilayer TP/MEH-PPV for transferring it alone. MEH-PPV had to be coated on the Al layer. The thickness obtained by spin-coating was also determined by the viscosity of the solution, which was very dependent on the purification process. It was very difficult to obtain constant film thickness between different samples and, depending on the purified batch used, layers 20 to 90 nm thick were obtained.

ITO coated glass substrates (thickness = 140 nm, resistance = 20 Ω per square), used for the transfer of functional pixels, were purchased from Thin Film Devices Inc. (USA), where the patterning was done by photolithography.

2.1.4 Water-soluble polymers

Although bilayers of triazene and MEH-PPV were not available, the transfer of single polymer layers was a topic of interest. Water-soluble polymers were used to prepare a bilayer with triazene to overcome the solvent compatiblity limitation. Gelatine and methylcellulose were chosen due to their availability and ease of spin-coating. Gelatine is a polypeptide whose repetition unit consists in the pattern glycine/other peptide/proline [89] (see Figure 2.1). It was obtained as food gelatine from DGF Stoess, Germany and spin-coated on triazene from an aqueous solution which had been stained with some drops of eosine dye.

Methylcellulose (Methocel MC, Fluka, low viscosity) is a alkylated polysaccharide whose structure is also shown in Figure 2.1. It was spin-coated on triazene from an aqueous solution as well.

---

[2]Purification was done by Simon Huber and Roland Hany at Empa.
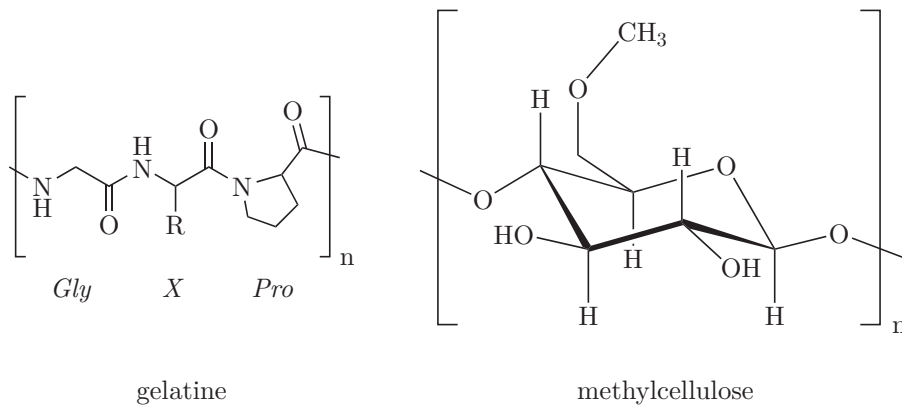
Figure 2.1 Chemical formula of gelatine and methylcellulose.

2.2   Laser processing

2.2.1   Choice of the laser

The triazene polymer was specially designed to absorb photons in the UV range. The lasers used for processing were chosen to match the emission wavelength with the absorption maximum.
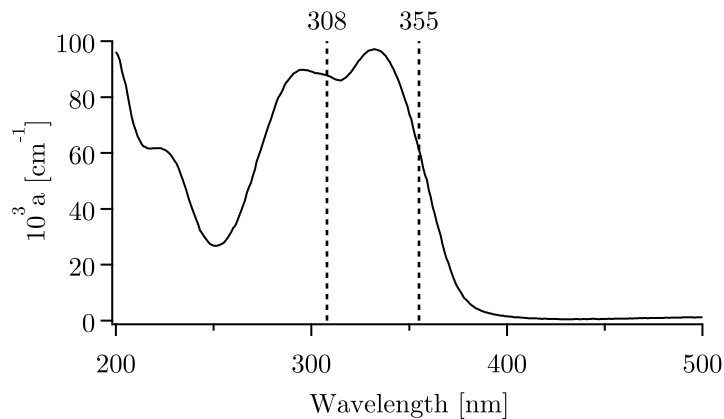
Figure 2.2 Absorption spectrum of the triazene polymer and the laser wavelengths chosen.

Among the commonly available emission wavelength, 308, 351 and 355 nm are the best suitable for the polymer, as it appears from Figure 2.2. Lasers emitting at 308 and 355 nm were used in this work. Emission at 308 nm is provided by an XeCl excimer laser, delivering a large, rectangular, top hat beam. Due to this fact and its high absorption by the polymer, it was believed to be most suitable for microstructuring and therefore, the standard laser used in this work.

The 355 nm wavelength is as well absorbed by the triazene, though less than at 308 nm. This wavelength is delivered by the third harmonic generation of a solid-state Nd:YAG laser, and offers the advantage of being Q-switched, giving access to shorter pulse lengths and much higher repetition rates. Therefore, selected experiments were carried out with a picosecond Nd:YAG[3] to investigate the influence of the pulse length. The corresponding experiments were performed also with a nanosecond Nd:YAG laser at 355 nm for comparing the effect of the pulse length at the same wavelength. The temporal pulse shape of the three laser is shown in Figure 2.3, as well as the corresponding full widths at half maximum (FWHM).
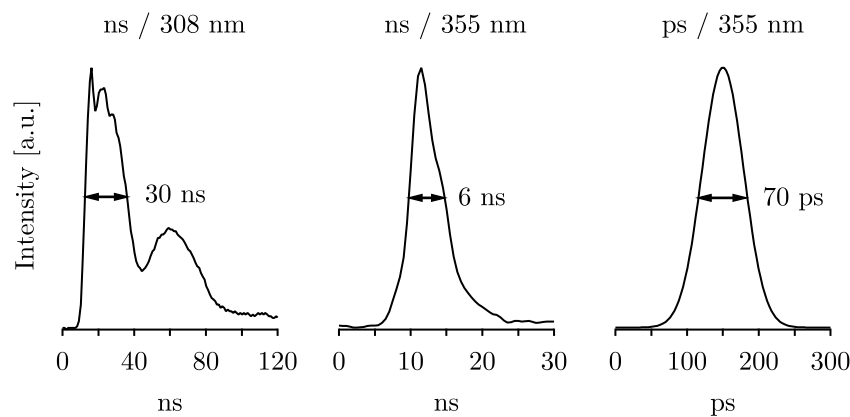
Figure 2.3 Relative intensity of the laser pulse versus time for the three lasers used. The full width at half maximum (FWHM) is given next to each pulse.

The pulse shape of the 308 nm emission exhibits two maxima, which is typical for this excimer laser. The various experimental setups used are described below.

2.2.2   Laser ablation

The experimental setup used for ablation is presented in Figure 2.4. The pulsed laser (ns / 308 nm, ns / 355 nm, ps / 355 nm) was operated at a repetition rate of 1 or 2 Hz (10 Hz for the picosecond) and controlled by a shutter. The beam intensity was controlled with a motorised attenuator plate (for the picosecond setup: rotating polariser operated manually). A homogeneous part of the beam was selected with a square mask of 2×2 mm^2 and imaged by a lens onto the sample with a magnification of 0.25, yielding a spot size of 500 µm.

The sample was mounted in the sample holder shown in Figure 2.4 (d), which was specifically designed for this work. It allows to position the sample precisely and to fix a receiver substrate in front of the donor film, either in contact or separated by a distance of

---

[3]These experiments were realised within the Laboratory of Lasers, Plasma and Photonic Processes (LP3), at the Université de la Méditerranée/CNRS, Marseille, France.
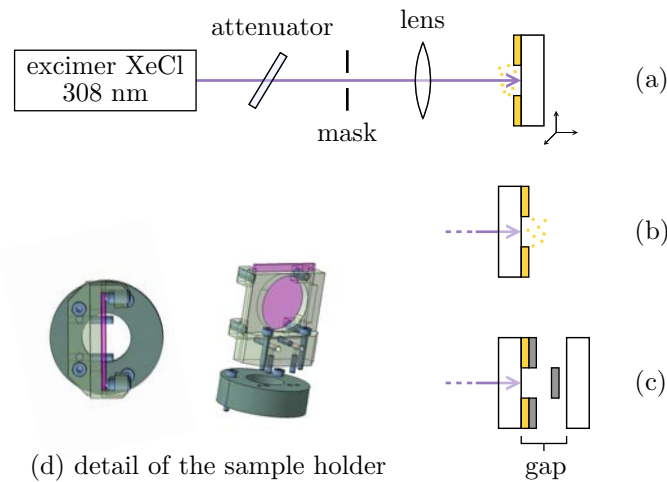
Figure 2.4 Experimental setup for (a) front side, (b) back side ablation and (c) forward transfer. (d) Detail view of the sample holder (the substrate is shown in pink).

up to 1 mm. The sample was placed perpendicular to the beam. In the case of front side ablation the film was facing the beam whereas for back side ablation, the beam impinged on the film through the fused silica substrate. The pulse energy at each fluence was measured by a pyroelectric energy meter (Molectron J4-09 or Gentec QE 50) placed at the end of the beam line and an average on 100 pulses was used. For measuring some energy ranges, a beam splitter was used to reduce the intensity of the beam.

The sample holder was mounted on a motorized translation stage. The whole system was controlled with a computer running the LabVIEW software and allowed to create a matrix of points for each sample, where the pulse energy and the number of pulses were varied.

The setup for picosecond experiments was similar, except that it was operated manually. The energy distribution profile of the picosecond laser beam was measured on a strongly attenuated beam by a CCD sensor.

2.2.3   Laser transfer

Laser forward transfer is realised by positionning a receiver substrate in front of the donor film to recover the ejected material. Irradiation was done from the back side. The practical realisation is similar to ablation from the back side, but a receiver substrate is added to the setup (see Figure 2.4 (c)). The transfer of various layers was done on carefully cleaned glass microscope slides cut to the same dimension than the fused silica plates. The transfer of functional pixels was done on ITO-coated glass substrates.

The transfer was investigated either in contact or with a gap separating the donor and the receiver substrates. In this case, spacers with a defined thickness were placed at

the edges between the two substrates and screwed together by the sample holder. The spacers were either cut glass (1 mm), MgO substrates (0.5 mm) or metal foil (20 μm).

2.2.4   Shadowgraphy imaging

A time-resolved lateral imaging technique was used to investigated the dynamics of flyer ejection and deposition. The features of interest are the flyer but also the shock wave induced by ablation. The technique suitable for visualising flows in transparent media is shadowgraphy [90]. The working principle is shown is Figure 2.5.
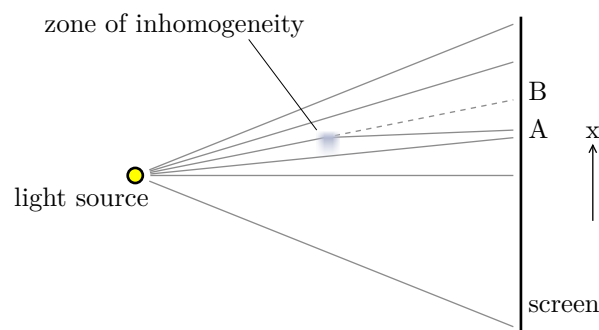
Figure 2.5 Principle of shadowgraphy: a zone with a non-zero $\partial^2 n/\partial x^2$ produces a variation of intensity on the screen. The beam deviated in the inhomogeneous zone increases the intensity arriving at A and darkens the zone B.

In the simplest setup, the phenomenon of interest is illuminated by a point light source and the resulting shadow images appear on the screen. In this work, the screen was replaced by an objective and a camera, but the principle remains the same. Obviously, opaque objects such as a flyer form a shadow on the screen. Under certain conditions, transparents media can create images as well. When the second derivative of the refractive index $\partial^2 n/\partial x^2$ is not zero in a zone, light rays crossing it are inhomogeneously refracted and will converge or diverge after the inhomogeneous zone. Therefore, the light intensity will be higher than ambient lighting at a certain point and lower at other points on the screen. Typically, shock waves produce this kind of features and are particularly well revealed by shadowgraphy.

Shadowgraphy experiments were performed with two different lasers. The principle was the same but for practical reasons, two different configurations were used. The first configuration, shown in Figure 2.6, utilises the 308 nm excimer laser.

The observation requires a pump-probe experiment with two pulsed lasers, because the processes of interest happens within the time scale of nanoseconds to microseconds, which is too fast for the applied camera. The pump laser, used to trigger ablation, was
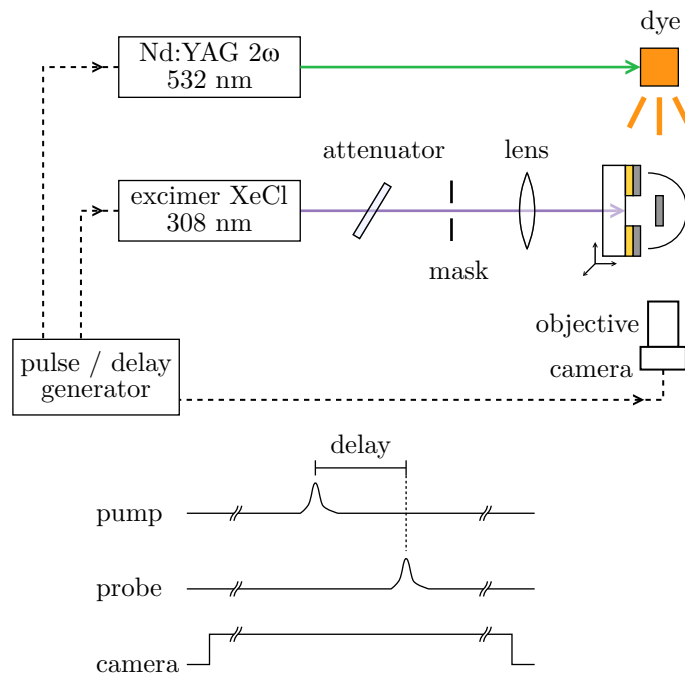
Figure 2.6 Scheme of the shadowgraphy setup used for investigations with the 308 nm excimer laser. The timeline at the bottom illustrates the synchronisation.

the excimer laser with the same configuration as presented above. The probe laser was a nanosecond Nd:YAG running at the second harmonic (532 nm), which was used to pump a fluorescent dye (Rhodamine 6G). The reason to apply a dye was to break the coherence of the probe laser, providing an illumination of better quality. The fluorescence decay time of 6–10 ns determined the temporal resolution of the experiment.

A digital pulse/delay generator (Stanford Research Systems DG535) was used to synchronise the two laser pulses. The sequence of events during data collection is illustrated on the timeline of Figure 2.6. The camera is openend before the pump pulse starts, but no picture is recorded due to low ambient light. The pulse generator delivers a signal to the pump laser, which triggers the ablation. The pulse generator sends after a tunable delay another signal to the probe laser, which illuminates the scene for the camera. Finally the camera is closed and the picture sent to a computer. As the flash illumination is much stronger than the ambient light, the camera "sees" only during the probe pulse and captures a snapshot of the process. In this way, the camera does not need to be synchronised precisely.

Each ablation spot yielded one picture at a given time delay. A sequence of picture was acquired by moving the stage to a new position and repeating the sequence with another time delay. The system was controlled by a computer, which recorded the pictures as well as the time delays.

For experiments with the picosecond laser, the setup was slighly different, because a gated ICCD (intensified charge-coupled device) camera could be used. On this type of

camera, photons arrive first into a photomultiplier with tunable gain before reaching the sensor. The photomultiplier allows to amplifiy the light and let it reach the sensor only for a given time, which can be as short as tens of nanosecond (the signal is *gated*). In this way, no pulsed illumination was required. The setup is shown in Figure 2.7.
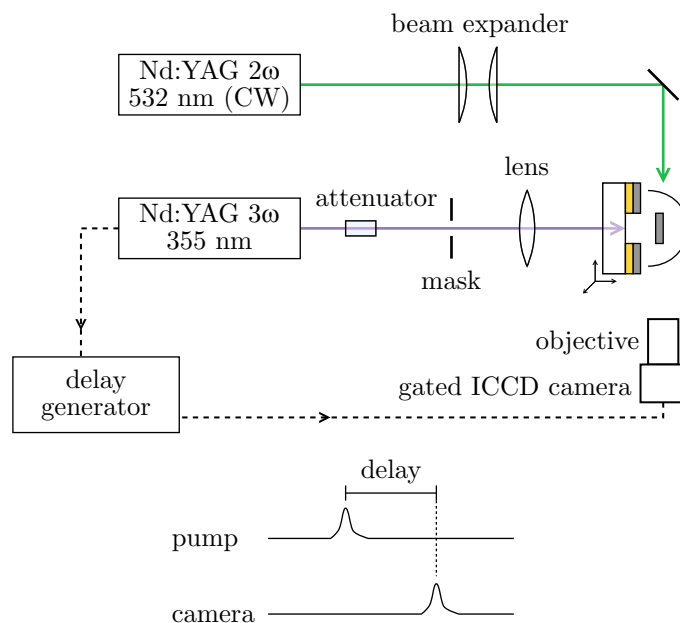
Figure 2.7 Scheme of the shadowgraphy setup used with the picosecond 355 nm Nd:YAG laser.

Continuous illumination was provided by a low-power Nd:YAG operating at 532 nm. The synchronisation was initiated by the picosecond laser, relayed after a tunable delay by the delay generator (DG535) and sent to the ICCD camera (Princeton Instruments). The gate time of the camera, giving the time resolution, was 20 ns. Pictures were aquired on a computer but the system was operated manually.

The distance scale was determined by moving the stage for a known length. After aquisition, the position of the moving features were measured with the help of a specially developed set of macros running under Igor Pro.

2.2.5   Vacuum setup

The polymers used in OLED are sensitive to oxygen and moisture. For making good devices, it is essential to protect them during the whole fabrication process. The preparation of the donor film and the characterisation after deposition occured in a glove box, and the transport of the sample between the laboratories was done in a vacuum box filled with nitrogen. The laser processing step needed as well a tight enclosure to ensure optimum protection from atmosphere. A vacuum chamber was chosen, because it would allow as

well to study the influence of the pressure on the deposition process. Moreover, most of the building parts were easily available commercially.

The vacuum chamber system was designed and setup for performing ablation and transfer experiments under controlled atmosphere or under vacuum while allowing imaging of the process. A schematic view is shown in Figure 2.8. The main requirements for the design were:

- One laser-grade viewport

- Visual access from the four sides for shadowgraphy, front and back side imaging

- Compact shape adapted to the working distance of the existing imaging equipment

- Fast pumping and inert gas purging

- Fast opening without tools

The two last requirements demanded a medium vacuum range (down to 10^{-2} mbar), which was fully sufficient for this purpose. The translation stage had to be small enough to fit into a compact design. Piezo electric actuators from attocube were chosen for this, with one vertical axis, one horizontal axis perpendicular to the laser direction and a rotation axis used for changing the irradiation side and to align the sample precisely. To gain space, no translation axis along the laser direction was build in the chamber. The translation required for fine-focusing the laser beam was instead achieved outside of the chamber by mounting the focusing lens on a linear stage. The motors were fixed onto a manual two-axis tilting stage for achieving fine alignment of the sample relative to the laser beam. Finally, the sample holder shown in Figure 2.4 (d) was fixed onto the top actuator.
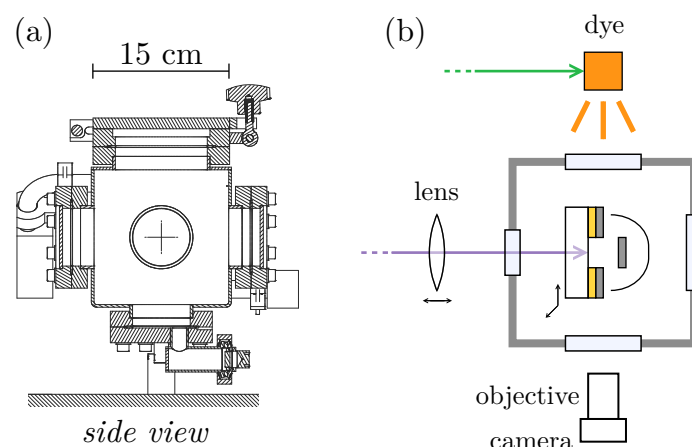
Figure 2.8 Scheme of the vacuum chamber: (a) cut view and (b) experimental setup shown for shadowgraphy.

A dry vacuum pump allowed to reach a base pressure of $5 \cdot 10^{-2}$ mbar. The vacuum chamber was inserted in the 308 nm laser setup presented above.

2.3   Samples characterisation

2.3.1   Depth profiling

Profilometry was used to measure the thickness and roughness of films and transferred pixels, as well as for measuring the depth of ablated craters. In this method, a tip scans the surface of the sample and the height profile is recorded. The vertical resolution is 3–5 nm, while the horizontal resolution and the maximum aspect ratio investigable are much coarser, because they are limited by the diameter of the tip of 5 µm . The method is similar to atomic force microscopy but much more straightforward and it allows to scan much larger distances (up to 10 mm). The depth profiling device was an Ambios XP-1. The ablation depth was measured by averaging the profile of the crater.

2.3.2   Imaging

2.3.2.1   Optical microscopy

Optical microscopy was the main imaging technique used for analysing the samples after processing. Overview pictures were taken with a Zeiss Stemi device and close-up views were done with a Zeiss Axioplan microscope, both under top illumination. The images were recorded with a Leica digital camera. The system had a length calibration for measuring the dimensions of the ablation spots, required for calculating the fluence.

2.3.2.2   Scanning electron microscopy

Scanning electron microscopy[4] (SEM) was used to analyse some samples in more detail. Pictures were taken with an environmental SEM Philips XL30 FEG device. An environmental microscope was used because of the low conductivity and rapid charge accumulation on the sample. Even then, samples had to be coated with 3 nm Pt prior to imaging for providing electrical conductivity.

2.3.3   Spectroscopic methods

Spectroscopic methods are an important tool for the investigation of the chemical structure of the materials and possible modifications upon ablation or transfer. They allow as well quantitative measurements after determination of the absorption coefficient.

2.3.3.1   UV-visible spectroscopy

It is essential to target the right chemical bond for getting clean ablation. In the case of triazene, the goal is to irradiate with photons absorbed by the triazene group, which will yield a clean and efficient ablation. The choice of the laser wavelength is given by the

---

[4]SEM imaging was performed by Philippe Gasser at Empa.

absorption spectrum, provided by UV-vis spectrophotometry. The absorption coefficient gives the theoretical penetration depth of the laser beam as well. Spectrophotometry allows to investigate quantitatively the changes in the chemical structure upon laser irradiation as well. Finally, it is a practical tool for non-destructive control of the film thickness of spin-coated samples. Samples were measured versus fused silica blank with a Varian Cary 50 device.

2.3.3.2   Raman spectroscopy

Raman spectroscopy investigates the vibrational levels of molecules (mid-infrared region of the spectrum) by measuring the light scattered by the sample. Most of the scattered intensity has the same wavelength than the incident light, but a part undergoes inelastic scattering, which shifts the frequency by an amount corresponding to a Raman transition. Due to the nature of the transitions, the selection rules are different to absorption spectroscopy. Raman is the appropriate method for sensing symmetrical groups, such as the N–N and N=N bonds in triazene. It was used to measure the amount of remaining triazene units after ablation.

Experiments were perfomed with an optical microscope connected to a laser source (HeNe, 633 nm) as excitation wavelength and to a monochromator for analysing the scattered light. This configuration allows to investigate ablated triazene films with a spatial resolution better than 50 µm, i.e., well below the ablation spot size.

2.3.3.3   Fluorescence spectroscopy

The light emission of electro-active compounds is a key point for making organic light-emitting diodes. Emission occuring from an electronic excited state created by charge injection is electroluminescence. The same radiative transition can also occur from an excited state created by light absorption, this phenomenon is called fluorescence. Due to its close relationship to electroluminescence, fluoresence was used to characterize the light-emitting function of the luminescent polymer after transfer, without the need of any electrical connection. Films of MEH-PPV were compared before and after transfer. The photoluminescence was measured in air with a Jobin Yvon Horiba FL311 Fluorolog using front face detection.

2.3.4   Physical properties

Several physical properties of the triazene polymer were measured with a view to provide parameters for modelling thermal diffusion.

The refractive index of TP was measured by spectroscopic ellipsometry[5] (Sopra ES-4G). For the density measurement, a piece of a thick film was floated in an aqueous NaCl

---

[5]Ellipsometry was measured by Rüdiger Kötz at PSI.

solution by adjusting the density of the solution, which was measured at the end. A density of 1100 kg/m^3 was obtained by this method.

The thermal diffusivity of TP was measured with the laser flash technique (Netzsch Micro Flash), where a laser pulse heats the lower surface of the sample and an infrared detector measures the transient temperature profile of the upper surface. A fitting model including the sample thickness allows to calculate the thermal diffusivity. In this case, the two-layer method was used: the thermal diffusivity of an aluminum plate (2 mm thick) was measured first as reference and a second time after being coated with a thick layer of TP (110 µm). The thermal diffusivity of the polymer was calculated by substracting the contribution of the aluminum plate, yielding a value of $1.0 \cdot 10^{-7}$ m^2/s. The heat capacity of TP was measured by differential scanning calorimetry (DSC) and a value of 1100 J/kg K at 25 °C was obtained. The thermal conductivity was calculated from the thermal diffusivity, density and heat capacity.

2.3.5 Light-emitting device characterisation

The characterisation of OLED consists in measuring the electrical and light emission properties of the device while protecting it from ambient air. The diodes were kept in inert atmosphere throughout the characterisation. For this, a portable sealed chamber with a viewport and electrical feedthroughs was used (see Figure 2.9).
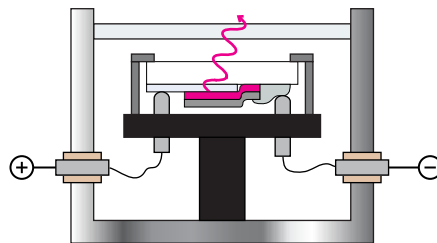
Figure 2.9 Sealed chamber used for diode characterisation. The device is protected from air while remaing fully accessible for electrical and optical measurements.

The diodes are tested by establishing electrical contact to the anode and the cathode. The ITO anode was larger than the pixel and contact was achieved with a metallic pin in the sealed box. The Al cathode had to be connected to a location outside the pixels, because if a metallic pin would touch the pixel directly, it would damage it and produce a short circuit. A connection line from the cathode to the pin was painted with silver paste.

Current-voltage curves were measured with a Keithley 2400 source-measure unit operated under Labview. When the electrical behaviour was good, the electroluminescence spectrum and luminance were recorded at a given voltage. The characterisation of a radiative source is expressed by the radiant intensity in watt per steradian (W/sr). However,

the human eye has a sensitivity depending on the wavelength, with a maximum in the green part of the spectrum. For this reason, the radiometric intensity does not correspond to the intensity perceived by the eye. When vision is concerned, the intensity of a light source is expressed as luminous intensity, which is the radiometric value corrected with the standard response curve of the eye, established on vision statistics (see Figure 2.10). The unit of the luminous intensity is the candela (cd), defined as $1/683$ W/sr at 540 nm.
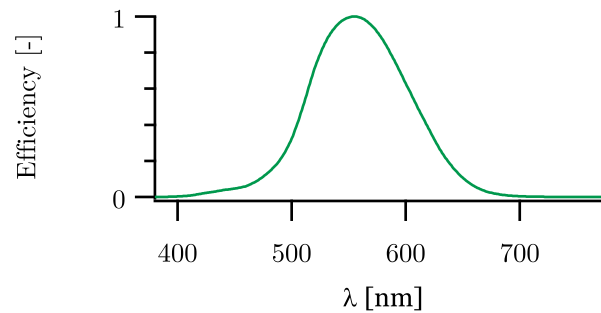
Figure 2.10 Standardised response curve of the human eye in photopic (day) vision. A efficiency of 1 corresponds to 683 cd·sr/W.

The correspondance at the other wavelengths, which is always smaller, is given by multiplicating with the the response curve. The luminous intensity is not sufficient to characterise a light source, because the eye is also sensitive to the area of the emitter. The luminous charateristics of a light source is therefore given by the luminance (in cd/m^2), defined as the luminous intensity divided by the area of the source.

Both luminance and emission spectrum were measured in a single step with a Minolta CS1000 spectroradiometer. The measurement area of the spectroradiometer was larger than the emitting area of the OLED and the measured signal was corrected by the ratio of the two surface areas.

Chapter 3

Theoretical modelling

In an experimental work, theoretical calculation are one method of testing and confirming hypotheses about the dynamics of the system. The first observation to explain with a model was the origin of the increase in the threshold fluence for front ablation of thin films of the triazene. The modelling of light absorption and thermal diffusion into the polymer layer allowed us to understand the observations. The thermal modelling was perfomed in collaboration with Boris S. Luk'yanchuk, Data Storage Institute, Singapore and is presented in Section 3.1.

The second problem requiring theroretical calculation was the energies involved in the creation of the shock wave and the flyer. The calculations of these data are presented in Section 3.2.

3.1   Heat transfer[1]

The situation to model is the front side ablation of thin triazene films. The system is shown in Figure 3.1. A mathematical model based on the linear heat transfer equations
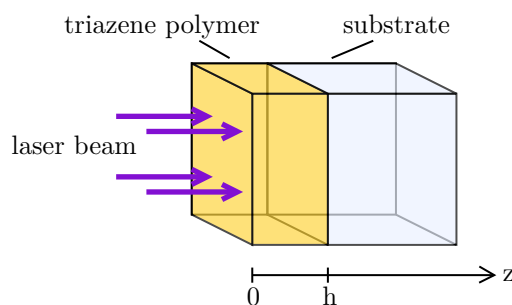
Figure 3.1 Scheme of the system considered for thermal modelling.

was used to compute the temperature of the film-substrate system directly after the laser pulse. The spot size is sufficiently large compared to the characteristic thermal diffusion

---

[1]The content of this section was published in [91].

length, allowing to model the system with one-dimensional differential equations for the heat transfer. The indices f and s refer to film and substrate respectively and h is the film thickness. The substrate thickness is H which is much larger than h allowing the simplification $H = \infty$. The heat balance equations are

$$\frac{1}{\chi_f}\frac{\partial T_f}{\partial t} = \frac{\partial^2 T_f}{\partial z^2} + Q_f(z,t) \tag{3.1}$$

for the film $0 \leq z \leq h$,

$$\frac{1}{\chi_s}\frac{\partial T_s}{\partial t} = \frac{\partial^2 T_s}{\partial z^2} + Q_s(z,t) \tag{3.2}$$

for the substrate $h < z < \infty$.

T is the temperature, χ the thermal diffusivity and $Q(z,t)$ describes the distribution of the absorbed laser intensity within the film and substrate. These terms can be written in the following form

$$Q_f(z,t) = \frac{\Phi}{t_l}g(t)F_f(z), \tag{3.3}$$

$$Q_s(z,t) = \frac{\Phi}{t_l}g(t)F_s(z). \tag{3.4}$$

Here Φ is an average laser fluence, the $g(t)$ function describes the pulse shape by

$$g(t) = \frac{t}{t_l}\exp\left(-\frac{t}{t_l}\right), \tag{3.5}$$

and $t_l = 0.409\, t_{\text{FWHM}}$ (the duration of the pulse at the full width at half maximum). Although it does not correspond exactly to the excimer double peak pulse shape for 308 nm pulses, we noticed that this simplification affected only marginaly the results. The function $F(z)$ in (3.3) and (3.4) represents the distribution of the laser intensity along the z-coordinate by

$$F_f(z) = \frac{\alpha_f}{\kappa_f}(1 - R_f)q_f(z), \tag{3.6}$$

$$F_s(z) = \frac{\alpha_s}{\kappa_s}\mathrm{T}_s q_s(z), \tag{3.7}$$

where α is the absorption coefficient for the film and the substrate, κ the thermal conductivity, $q(z)$ the normalized distribution of the laser intensity and R_f and T_s are the film reflectivity and substrate transmittivity respectively. R_f depends on the film thickness according to the following relation, valid for normal incidence [92]

$$R_f = |r|^2 = \left|\frac{r_{mf}e^{-2i\psi} + r_{fs}}{e^{-2i\psi} + r_{mf}r_{fs}}\right|^2. \tag{3.8}$$

The index m refers to the medium (air). r_{mf} and r_{fs} are the amplitude of the reflection coefficients on the boundaries media/film and film/substrate, respectively, given by

$$r_{mf} = \frac{\sqrt{\epsilon_m} - \sqrt{\epsilon_f}}{\sqrt{\epsilon_m} + \sqrt{\epsilon_f}} \ , \ r_{fs} = \frac{\sqrt{\epsilon_f} - \sqrt{\epsilon_s}}{\sqrt{\epsilon_f} + \sqrt{\epsilon_s}}. \tag{3.9}$$

The function ψ is proportional to the film thickness h

$$\psi = \frac{2\pi}{\lambda} h \sqrt{\epsilon_f}, \tag{3.10}$$

where λ is the laser wavelength. Thus R_f is determined by h and the three relative dielectric permittivities ϵ_f, ϵ_m and ϵ_s, of the film, medium and substrate, respectively. ϵ is given by the refractive index n and the extinction coefficient k, according to

$$\sqrt{\epsilon} = n + ik \quad , \quad k = \frac{\alpha\lambda}{4\pi}. \tag{3.11}$$

As the optical properties of the medium (air) are close to vacuum, we take $\epsilon_m = 1$.

Determining q_f and q_s in (3.6) and (3.7) would require to solve the Maxwell equations. However for simplicity we make the following assumptions:

1. The absorption coefficient of the substrate is by several orders of magnitude smaller than that of the film. Therefore we assume that $F_s(z) = 0$.

2. The distribution of the intensity in the film is derived from the Lambert–Bouguer's law of absorption $(1 - R_f)e^{-\alpha_f z}$.

After these simplifications the initial equations (3.1) and (3.2) become

$$\frac{1}{\chi_f} \frac{\partial T_f}{\partial t} = \frac{\partial^2 T_f}{\partial z^2} +$$
$$(1 - R_f) \frac{\alpha_f}{\kappa_f} \frac{\Phi}{t_l} \frac{t}{t_l} \exp\left(-\frac{t}{t_l}\right) e^{-\alpha_f z}, \tag{3.12}$$

$$\frac{1}{\chi_s} \frac{\partial T_s}{\partial t} = \frac{\partial^2 T_s}{\partial z^2}. \tag{3.13}$$

Equations (3.12) and (3.13) should be solved with boundary conditions. For the outer region we consider thermal insulation

$$\kappa_f \left.\frac{\partial T_f}{\partial z}\right|_{z=0} = 0 \ , \ T_s(z)|_{z\to\infty} = 0, \tag{3.14}$$

and a continuity of temperature and thermal flux between film and substrate

$$T_f|_{z=h} = T_s|_{z=h} \ , \ \kappa_f \left.\frac{\partial T_f}{\partial z}\right|_{z=h} = \kappa_s \left.\frac{\partial T_s}{\partial z}\right|_{z=h}. \tag{3.15}$$

The intitial temperatures are equal to zero

$$T_f(z)|_{t=0} = T_s(z)|_{t=0} = 0. \tag{3.16}$$

This problem can be solved easily by applying the Laplace transform

$$\tilde{T}_f(z,p) = \int_0^\infty e^{-pt} T_f(z,t) \, dt, \tag{3.17}$$

$$\tilde{T}_s(z,p) = \int_0^\infty e^{-pt} T_s(z,t) \, dt. \tag{3.18}$$

The inverse transforms are given by

$$T_f(z,t) = \frac{1}{2\pi i} \int_{\gamma-i\infty}^{\gamma+i\infty} e^{pt} \tilde{T}_f(z,p) \, dp, \tag{3.19}$$

$$T_s(z,t) = \frac{1}{2\pi i} \int_{\gamma-i\infty}^{\gamma+i\infty} e^{pt} \tilde{T}_s(z,p) \, dp. \tag{3.20}$$

The Laplace transform converts equations (3.12) and (3.13) into a set of ordinary differential equations

$$\frac{d^2\tilde{T}_f}{dz^2} - \frac{p}{\chi_f}\tilde{T}_f \quad + \frac{(1-R_f)\Phi}{(1+pt_l)^2}e^{-\alpha_f z} \quad = 0, \tag{3.21}$$

$$\frac{d^2\tilde{T}_s}{dz^2} - \frac{p}{\chi_s}\tilde{T}_s \qquad\qquad = 0. \tag{3.22}$$

These equations should be solved with the boundary conditions

$$\left.\frac{\partial \tilde{T}_f}{\partial z}\right|_{z=0} = 0 \quad , \quad \tilde{T}_s(z)\Big|_{z\to\infty} = 0,$$

$$\tilde{T}_f\Big|_{z=h} = \tilde{T}_s\Big|_{z=h} \quad , \quad \kappa_f \left.\frac{\partial \tilde{T}_f}{\partial z}\right|_{z=h} = \kappa_s \left.\frac{\partial \tilde{T}_s}{\partial z}\right|_{z=h}. \tag{3.23}$$

The solutions of equations (3.21) and (3.22) are given by

$$\tilde{T}_f = a\exp\left(-\sqrt{\frac{p}{\chi_f}}z\right) + b\exp\left(\sqrt{\frac{p}{\chi_f}}z\right)$$
$$\qquad - \frac{\alpha_f\chi_f}{\kappa_f(\alpha_f^2\chi_f - p)}\frac{(1-R_f)\Phi}{(1+pt_l)^2}e^{-\alpha_f z}, \tag{3.24}$$

$$\tilde{T}_s = a\exp\left(-\sqrt{\frac{p}{\chi_s}}z\right). \tag{3.25}$$

The unknown constants a, b and c can be obtained from the boundary conditions (3.23). The inverse Laplace transform is complicated to solve analytically but it can be solved numerically. The result gives the temperature of the TP film for each time and position.

3.2   Energy balance

The calculation of an energy balance of the LIFT system allows to analyse the possible energy consumption pathways and evaluate their relative importance.

The energies involved in the process were evaluated from an energy balance between the input and the output terms. The input contributions are the incident laser energy E_{laser} and the decompostion energy of the ablated volume of triazene, E_{dec}.

The output terms comprise the energy released into the shock wave (E_{SW}) and the kinetic energy of the flyer (E_{flyer}), which can be both evaluated from the shadowgraphy experiments. They also include terms much more difficult to quantify, such as the thermal and mechanical (shock propagation through the substrate) losses, as well as mechanical work to detach the flyer. All these unknown contributions are grouped into the energy losses E_{loss}. The energy balance is then

$$E_{\text{laser}} + E_{\text{dec}} = E_{\text{SW}} + E_{\text{flyer}} + E_{\text{loss}}. \tag{3.26}$$

To compare the energies under different conditions, it is more practical to normalize Equation 3.26 on its left hand side

$$1 = \eta_{\text{SW}} + \eta_{\text{flyer}} + \eta_{\text{loss}}, \tag{3.27}$$

where η_i is the normalized energy of term i, defined by

$$\eta_i = \frac{E_i}{E_{\text{laser}} + E_{\text{dec}}}. \tag{3.28}$$

The incident energy is given by

$$E_{\text{laser}} = A \cdot \Phi_{\text{laser}} \cdot \text{T}_s, \tag{3.29}$$

where A is the ablated area and Φ_{laser} is the laser fluence. T_s is the the transmittance of the substrate, relevant for back side ablation where the laser impinges through the fused silica plate. For front side irradiation, $\text{T}_s = 1$. The decomposition energy is calculated from the decomposition enthalpy of the polymer $\Delta_{\text{dec}}H$. The value is only strictly valid for an isobaric transformation, but this approximation was also used by other authors [87,93]. The decomposition energy is

$$\begin{aligned} E_{\text{dec}} &= \Delta_{\text{dec}}H \cdot m \\ &= \Delta_{\text{dec}}H \cdot \rho_f A d, \end{aligned} \tag{3.30}$$

with m being the mass of the ablated polymer film, ρ_f its density and d the ablated depth. The ablation depth was measured by profilometry after front side ablation.

The energy of the shock wave was evalutated by the planar model developed by Frei-

wald [94]. It was also applied for analysing the ablation of a similar triazene polymer [87] and found to be more appropriate than a model accounting for the hemispherical geometry [95]. The model includes the energy of the released gaseous debris, E_{debris}, and the energy transferred to the surrounding gas, E_{gas}. The energy of the shock wave is given by

$$
\begin{aligned}
E_{\text{SW}} \quad = \quad & E_{\text{debris}} + E_{\text{gas}} && (3.31) \\
= \quad & \left[\frac{Ad}{8} \left(\frac{2}{\gamma+1} \right)^2 \rho_f \right] v^2 \\
& + \left[\frac{\rho_g A}{\gamma+1} \left(\frac{1}{\gamma-1} + \frac{4}{\gamma+1} \right) \right] v^2 x, \\
&&& (3.32)
\end{aligned}
$$

where ρ_g is the density of the surrounding atmosphere and γ its adiabatic ratio. In this work, we added a parameter t_0 to allow for a delayed observation of the origin of the shock wave. The position as function of time is given by

$$
x = \frac{\left(\frac{2}{3} C_5 E_{\text{SW}}^{\frac{1}{2}} (t - t_0) + C_4^{\frac{3}{2}} \right)^{\frac{2}{3}} - C_4}{C_5}, \tag{3.33}
$$

with

$$
\begin{aligned}
C_4 \quad &= \quad \frac{Ad}{8} \left(\frac{2}{\gamma+1} \right)^2 \rho_f && (3.34) \\
C_5 \quad &= \quad \frac{\rho_g A}{\gamma+1} \left(\frac{1}{\gamma-1} + \frac{4}{\gamma+1} \right). && (3.35)
\end{aligned}
$$

C_4 and C_5 are known and the fit of x versus t yields E_{SW} and t_0. We noticed that the value for the ablated thickness had only a very minor influence on the calculated energy of the shock wave. This is due to the predominance of the C_5 term in the shock wave equation and the low contribution of the exothermal decomposition to the total energy.

The kinetic energy of the flyer, E_{flyer}, is calculated from the initial velocity and the mass with

$$
E_{\text{flyer}} \quad = \quad \frac{1}{2} \rho_f Ah \cdot v_{\text{flyer}}^2, \tag{3.36}
$$

where the flyer thickness h was calculated from the film thickness minus the ablated depth d. One assumption that was used in this calculation is that the ablated thickness of triazene corresponds to the ablation depth measured for front ablation at the corresponding fluence.

Chapter 4

Results and Discussions

The results are presented in a growing complexity order, starting from ablation of a single layer of triazene, followed by material ejection and material transfer. Finally, the goal of the work is demonstrated in the last part.

4.1 Ablation of the triazene polymer

Laser ablation of the triazene polymer is the basis of LIFT with a sacrificial layer, therefore it is natural to start the work with an investigation of the triazene ablation behaviour. Ablation studies were mainly realised with the excimer laser at 308 nm, because this laser is best adapted for the laser processing of triazene. The energy beam profile is flat and the emission wavelength corresponds to the absorption maximum of the triazene group. Other lasers were used as well, for both scientific and technological reasons. The scientific interest was to vary the wavelength and the pulse duration. For this, the frequency-tripled Nd:YAG emission wavelength (355 nm) was choosen, at which the absorption coefficient of the triazene is still high. Two lasers with different pulse length were used, i.e. nanosecond and picosecond. Therefore, laser pulses with nanosecond duration at 308 and 355 nm plus picosecond pulses at 355 nm were available, allowing to vary two parameters independently.

The technological motivation was to test solid-state lasers, which are more compact and easier to maintain than gas lasers, and most importantly, which can be operated at higher repetition rates. For these reasons solid-state laser would be the most cost-effective for an upscaling to an industrial process and therefore it is important to know whether they are suitable for the LIFT process.

The ablation is characterised qualitatively, with the crater shape and morphology, and quantitatively by the ablation rate and threshold fluence.

4.1.1   Ablation morphology

4.1.1.1   Excimer laser[1]

The ablation by the excimer laser is discussed first. A typical ablation spot is shown in Figure 4.1, where a 420 nm thick triazene film was ablated with a single pulse at a fluence of 180 mJ/cm^2.
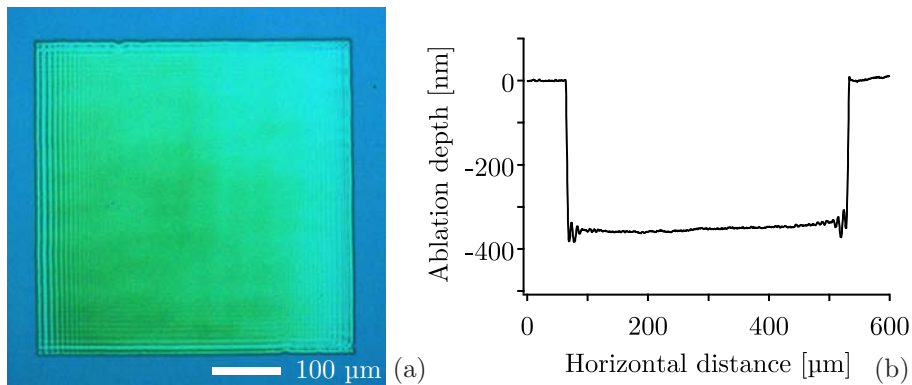
Figure 4.1 (a) Optical microscopy picture of an ablation spot done in a 420 nm thick TP film by one pulse of 180 mJ/cm^2. (b) Corresponding depth profile scanned vertically.

The corresponding depth profile reveals that the ablation depth is about 350 nm, which means that a part of the initial film has not been ablated. The ablation crater is very flat and homogeneous, which corresponds to the good beam profile of the excimer laser. However, both the picture and the profile reveal the presence of ripples at the side of the crater and parallel to them. These ripples intersect at the edges to form a grid.

Close-up views of the ablation craters were obtained by scanning electron microscopy (SEM). Figure 4.2 shows the surface of a 360 nm thick TP film after irradiation.

The figure shows the corner of ablation spots after 6 pulses, one close to (20 mJ/cm^2, a) and one well above (90 mJ/cm^2, b) the threshold fluence. For the latter fluence, a clean ablation behaviour is observed for the triazene polymer. The edges of the crater are sharp and no debris or redeposited material are visible in the crater or around it. This is in agreement with previous studies on the triazene polymer [97]. The spot at the low fluence is free of debris as well but exhibits the periodic ripples observed in the optical picture. The wavy shape of the crater edge at 90 mJ/cm^2 is due to the same rippling effect.

Some samples were irradiated at 30 mJ/cm^2 with 6 pulses, i.e. a condition under which the ripples are amplified, to investigate this effect in more detail and to measure the pattern period. An example is shown in Figure 4.3.

In this case, the wavy pattern spreads across the whole ablation spot. The periodicity is between 7 and 10 μm and increases slightly when the mask size is reduced. A tilted

---

[1]A part of this section was published in [96].
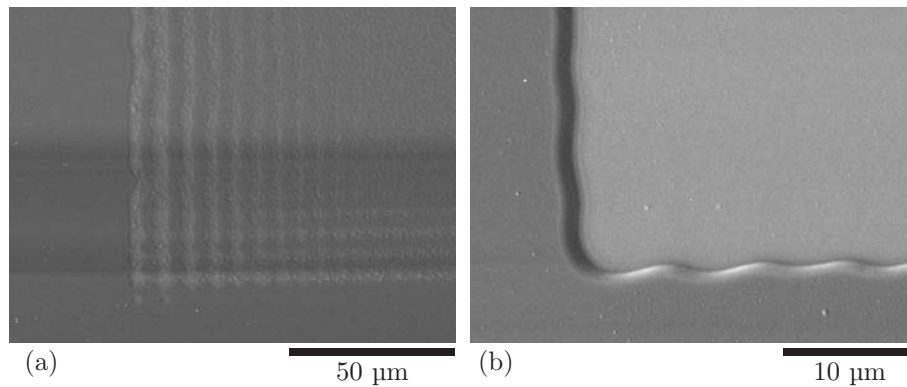
Figure 4.2 Scanning electron microscopy of ablation craters after 6 pulses at (a) 20 and (b) 90 mJ/cm^2. The film thickness is 360 nm. The sample was coated for the SEM analysis with a 3 nm layer Pt for electrical conduction.
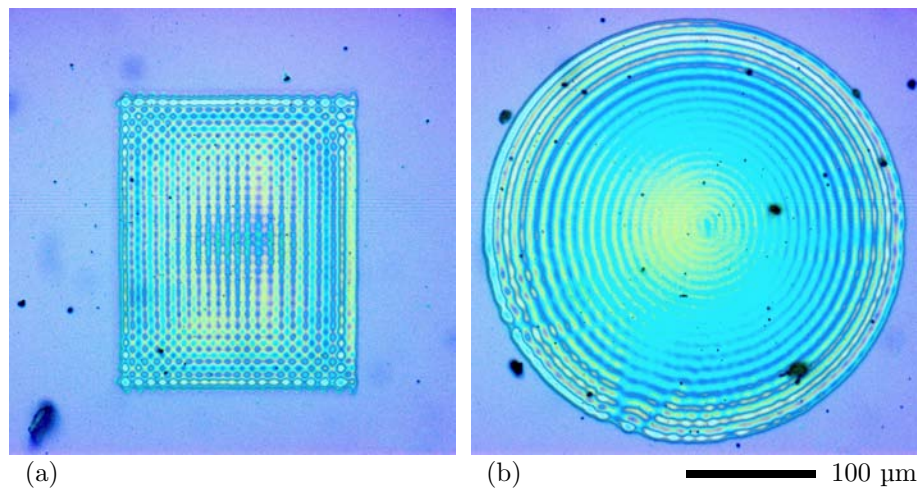
Figure 4.3 Optical microscopy of ablation spots realised with (a) a square and (b) a round mask. The pattern were obtained after 6 pulses at 30 mJ/cm^2.

mask (i.e. the right and left edge not in the focus) produces the most visible changes in the period, with a difference of up to 100% between the ripple separation at the left and at the right side of the spot. The wavy pattern follows the shape of the mask as well, as seen from the round spot (see Figure 4.3 b).

The origin of the ripples is not yet clear, but there is a range of different mechanisms which can produce variations in the ablation depths. These can be divided in optical and mechanical processes.

Laser beam inhomogeneities The observed structures are too regular, as beam inhomogeneities are normally random or constant if they are due to damages of defects of the optical system of the laser and setup.

Far field (Fraunhofer) diffraction Diffraction manifests itself in the apparent bending of waves around small obstacles. In the far field, periodic patterns are observed

behind obstacles, e.g. a mask. These periodic patterns expand to the outside of the mask and the intensities of the amplitudes decay fast ($I_1 = 0.045 I_0$, $I_2 = 0.016 I_0$, etc.). The observation that the ripples are not really expanding to the outside and that they spread with a slowly decaying amplitude inside the mask area (including the complete area) suggests that diffraction is also not very probable.

Interferences The wave properties of light lead to interference, but certain conditions of coherence must be met where the superposition of two or more waves results in a new wave pattern, which is periodic with a spacing depending on the wavelength and interference angle. In this case periodic patterns (including circular pattern for circular waves) are obtained which expand over the complete area of irradiation. This description would be so far the best to our observation, although the origin of the "two" beams is not clear.

Acoustic or surface acoustic wave which is frozen in the resolidifying polymer after ablation. This type of wave should expand over the complete area with constant amplitude, although it may be formed from the interference of a reflected wave e.g. at the ablation crater wall. However, Figure 4.2 (a) shows that the parts of the film (dark) between the ablated ripples (bright) did not undergo material removal. An acoustic wave would affect the whole surface and no intact bands would remain. This fact does not really support the acoustical hypothesis.

It is difficult to explain why this effect is more pronounced at low fluences and, depending on the fluence, why it is observed with a decaying amplitude only at the edge or over the complete area. It may be that the observed effect is due to a combination of several of the above described effects.

In summary, a definitive conclusion on these ripples cannot be drawn. However, they mainly appear at low fluence and after several pulses. The LIFT process requires a single pulse with a large ablation depth, which indicates that the ripple creation is not critical for the forward transfer.

The determination of the ablation depth as function of the fluence is a key parameter for the optimisation of the film thickness of the sacrificial layer. The ablation rate was measured for single pulses and multi-pulse experiments, which would reveal possible incubation effects.

A typical plot of the ablation depth versus number of pulses at several fluences is shown in Figure 4.4. The film thickness was 420 nm and is indicated in the plot. The crater obtained after one pulse at the highest fluence corresponds to Figure 4.1.

At 20 mJ/cm^2, very close to the threshold fluence, practically no ablation occurs. Above the threshold fluence and up to 28 mJ/cm^2, ablation is measured after one pulse, but the ablation depth does not increase or only very little with successive pulses, i.e. there is a stagnation of the ablation with multi-pulse irradiation. The situation changes above 32 mJ/cm^2, where a linear increase of the ablated depth versus the number of
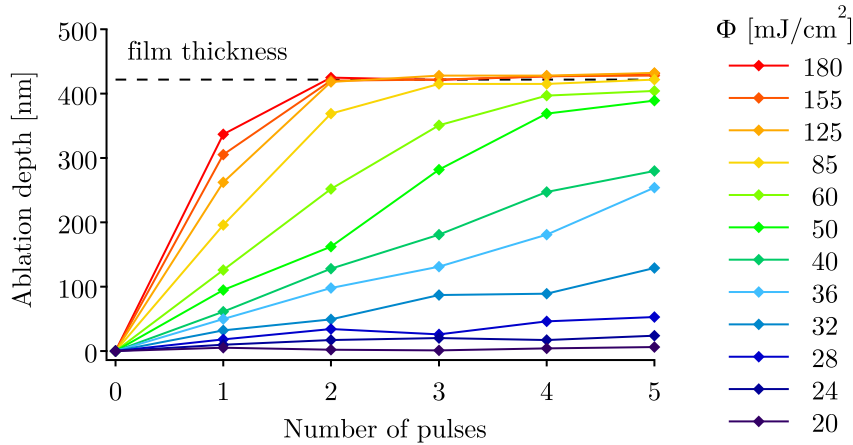
Figure 4.4 Ablation depth versus pulse number for a 420 nm thick triazene film.

pulses is observed. In this case, each pulse ablates the same amount of material with a given rate (depth per pulse). This rate increases with increasing fluence until it is limited by the available film thickness. Starting from 50 mJ/cm^2, a saturation appears after 5 pulses and at the highest fluence (180 mJ/cm^2) the second pulse is already in the saturation regime. It is interesting to notice that ablation at 50 and 60 mJ/cm^2 does not remove the complete polymer layer, although the linear progression of the ablation depth would suggest it. This effect is related to the proximity of the substrate and is discussed extensively in the next section.

The corresponding depth profiles at selected fluences are presented in Figure 4.5. The profiles at 60 and 125 mJ/cm^2 reveal as expected a regular ablation depth across the crater. The profiles at the low fluences are more surprising. At 28 mJ/cm^2, the first pulse yields a shallow yet flat crater. After the second pulse, the crater gets deeper at the edges but rough in the center. Successive pulses increase this fact even more. This effect is visible as well at a fluence of 36 mJ/cm^2, although much less pronounced.

It was shown that irradiation of the triazene polymer with a UV lamp causes photodegradation of the triazene group and crosslinking of the remaning material [88]. Moreover, the degradation of the triazene chromophore releases nitrogen. The same effects are induced with laser irradiation below the threshold fluence, but in a much shorter time due to the higher light intensity. In this case, no material removal takes place and the polymer is merely degraded. The released nitrogen can slowly diffuse out of the film and escape.

Well above the threshold, all the material that could have been degraded is removed from the sample and a new, fresh layer is exposed to the upcoming laser pulse. In this way, successive pulses have the same effect until the substrate is reached. Nitrogen is released as well and helps ablation in providing additional pressure for ejecting the material. But for the fluence range just above the threshold, there is a mixture of photodegradation and ablation. The laser pulse causes photodegradation in a certain thickness, but only
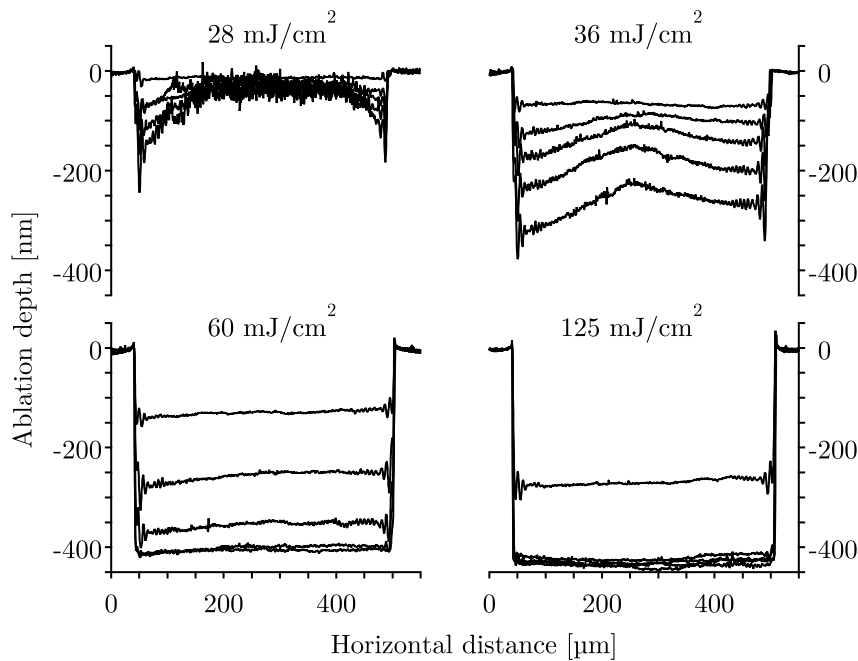
Figure 4.5 Depth profiles of the ablation spots after 1 to 5 pulses (shallowest to deepest crater, respectively) for four different fluences.

ablates a thinner layer. The following laser pulse impinges on a modified material: the chromophore density of is reduced due to photodegradation and the polymer is partially cross-linked [88]. The sum of these two effects produces a material more difficult to ablate, and the threshold fluence is increased. In this way, successive pulses do not achieve further ablation but only photodegradation and the crater depth is constant. This phenomenon is the inverse of incubation, where the material become more prone to ablation after several pulses, and was also observed for polyimide, where ablation stops after a certain number of pulses at a given fluence [98].

The formation of the rough structure is due to the released nitrogen, which is not able to escape easily from to the surounding film. Gravimetric measurements showed that a release of nitrogen can be detected before ablation is observed [86], indicating that a gas release happens at a lower fluence than the actual ablation. The gas creates bubbles, which are trapped within the film and, under the action of the pressure, deform the film and create the observed roughening. These gas bubles can be seen as well on the SEM picture (Figure 4.2 a). It appears clearly at this point that single pulse ablation at a high fluence is preferable to multi-pulse ablation at a lower fluence if one wants to get a precise and flat ablation crater.

4.1.1.2 Nd:YAG lasers

Two frequency-tripled Nd:YAG lasers at 355 nm with different pulse length were used in this work as well. A typical ablation spot obtained with the nanosecond 355 nm laser in

a 400 nm thick triazene film is shown in Figure 4.6.

Figure 4.6 (a) Optical microscopy picture of an ablation spot done in a 400 nm thick TP film by one pulse of 150 mJ/cm^2 with the ns / 355 nm laser. (b) Corresponding depth profile scanned vertically. (c) Magnified profile from the rectangle-surrounded zone of (b). The red line is the result of a low-pass filtering. The original profile is shown is black.

The edges or the crater are sharp as well but the ablation profile is different from the excimer laser. The bottom of the crater is rough and irregular. The roughness seen on the profile can be separated in two components by applying a low-pass filter on the profile. The result is shown in Figure 4.6 (c) as red line.

A regular short period wave is superimposed with an irregular waviness. It is clear from the picture that the wave with the short period corresponds to the ripple pattern described in the previous section. The periodic distance is the same, however the ripples extend over the whole surface after only one pulse at a relatively high fluence, which is different to the observations for the excimer laser irradiation, where these ripples are only observed at low fluences and several pulses. This may indicate that the coherence of the beam plays a important role, because the Nd:YAG beam has a higher spatial coherence than the excimer laser.

The irregular waviness revealed by the filtering is a characteristic of the energy beam profile of the laser. The applied solid-state laser has a poor spatial homogeneity of the beam intensity, which is reflected in the ablation depth of the polymer. Moreover, concentric rings can be distinguished on the top right and bottom left corner of the ablation spot (Figure 4.6 a). They contribute as well to the long-distance waviness of the crater and may orignate from interference effects, arising when a highly coherent beam is used, which

is the case for the Nd:YAG. These rings do not appear with the less coherent excimer laser.

Figure 4.7 shows an ablation spot at similar conditions for the picosecond 355 nm laser.
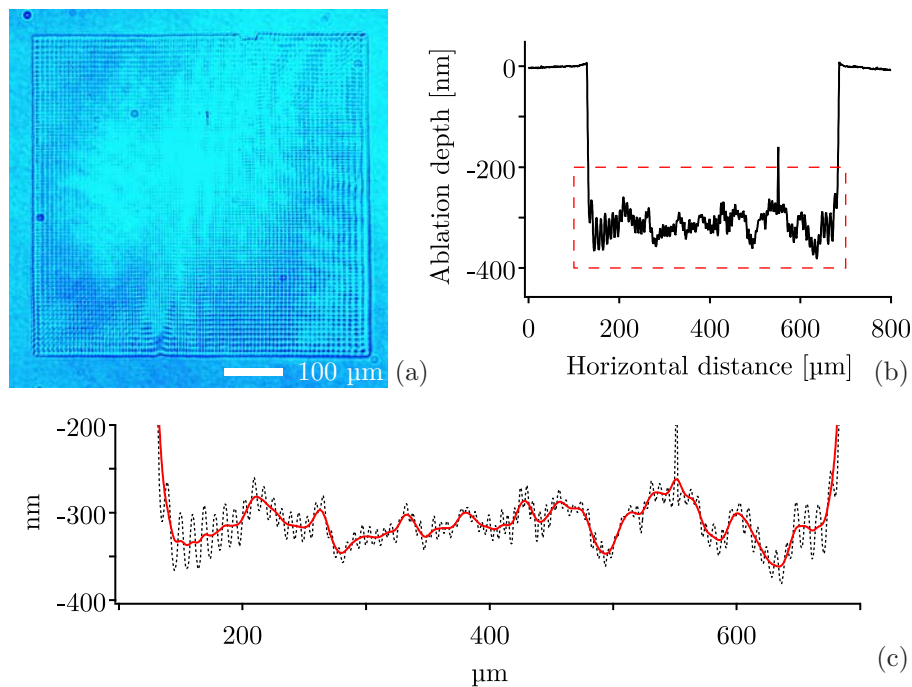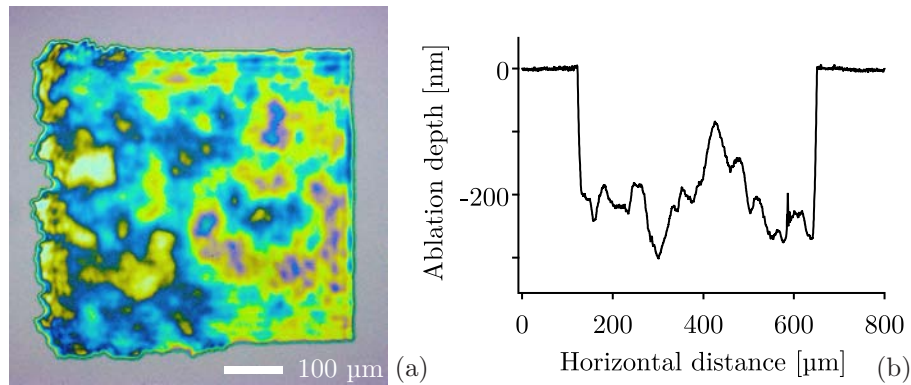

Figure 4.7 (a) Optical microscopy picture of an ablation spot done in a 400 nm thick TP film by one pulse of 160 mJ/cm^2 with the ps / 355 nm laser. The irregular shape at the left side comes from a partially ablated mask. (b) Corresponding depth profile scanned vertically.

The left edge of the crater is not straight, due to a technical problem, i.e. the mask was partially ablated at this side during the experiment. The other edges are as sharp as for the two other lasers. The crater depth is again very irregular, as shown by the profile and the interference colours on the picture. The variation between the deepest and the shallowest points is even larger than for the nanosecond laser.

The quality of the ablation profile is directly related to the beam profile of the laser, which was measured for the picosecond laser (shown in Figure 4.8).
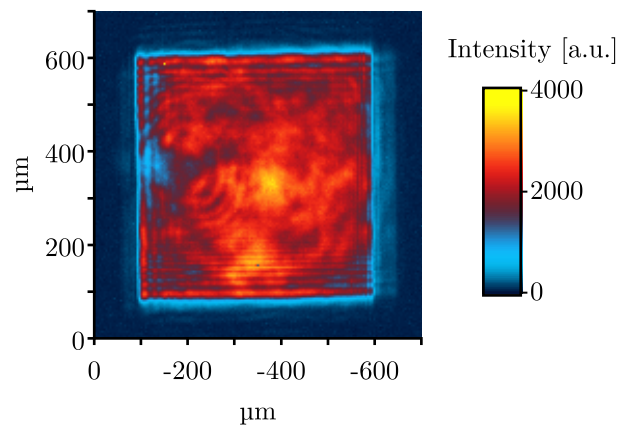
Figure 4.8 Spatial distribution of the beam intensity for the 355 nm picosecond laser setup.

It is noteworthy that the beam profile cannot be directly compared with Figure 4.7 because it was recorded after correcting the problem with the mask and realigning the beam. It corresponds to the best profile that has been obtained, which still presents large inhomogeneities within the spot. A variation of more than 400% is observed, which has of course a very pronounced influence on the ablation depth profile.

A first conclusion at this point is that the Nd:YAG "as is" does not seem to be adapted for LIFT, due to the required homogeneous distribution of the "thrust" onto the top layer which should be transferred. The actual effect of the beam profile on the material ejection is discussed later.

4.1.2 Ablation threshold fluence[2]

The threshold fluence of ablation, together with the ablation rate, determines the fluence required to achieve the desired ablation depth. The knowledge of this value allows to tune the fluence to the film thickness, but also to predict the ablated thickness when it is not measurable, such as in multi-layer forward transfer experiments.

For each fluence, the ablation depth was plotted versus the pulse number (e.g. Figure 4.4) and the slope over the linear domain yielded the ablation rate. The latter was plotted versus the fluence, giving the characteristic ablation curve, which was fitted by Equation 1.5. Figure 4.9 shows typical ablation curves for two different film thicknesses and their corresponding fit obtained with the excimer laser.
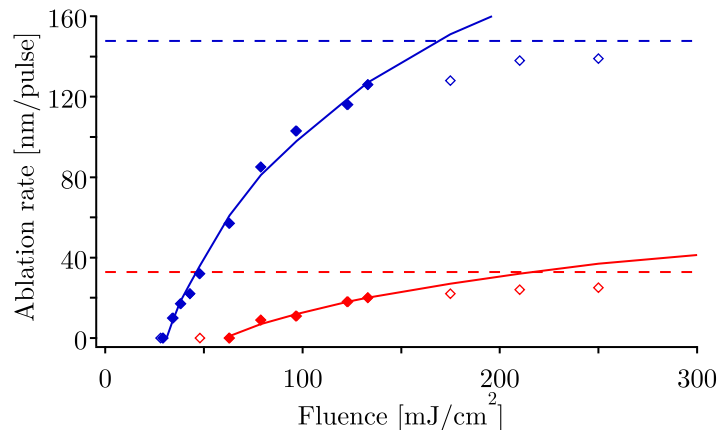
Figure 4.9 Ablation curves of TP on a fused silica substrate for a 148 nm (blue) and a 33 nm (red) thick films. The interrupted lines indicate the film thickness.

Three domains are visible: no ablation is observed below the threshold fluence; the ablation rate just above the threshold shows a logarithmic dependence on the fluence, according to Equation 1.5; finally at high enough fluences the ablation rate is limited by the film thickness. It is interesting to note that the ablation rate deviates from the fit in

---

[2]A part of this section was published in [91].

the range where ablation rates similar to the film thickness are predicted. In this fluence range a smooth transition to the theoretical limit (i.e. film thickness) is observed. As revealed in Figure 4.9, films with different thicknesses exhibit different threshold fluences. This effect is discussed in detail below.

4.1.2.1   Influence of the film thickness

The influence of the film thickness on the ablation threshold is an important parameter for the application of the triazene polymer as sacrificial layer in the LIFT process. TP films with a thickness between 10 and 400 nm were therefore investigated in detail. Figure 4.10 shows the measured threshold fluences ($\bullet$) versus film thickness for ablation experiments using fused silica substrates. It will be shown below that the substrate material plays a role for the value of the threshold fluence. For this reason, it is indicated in all figure captions of this section.
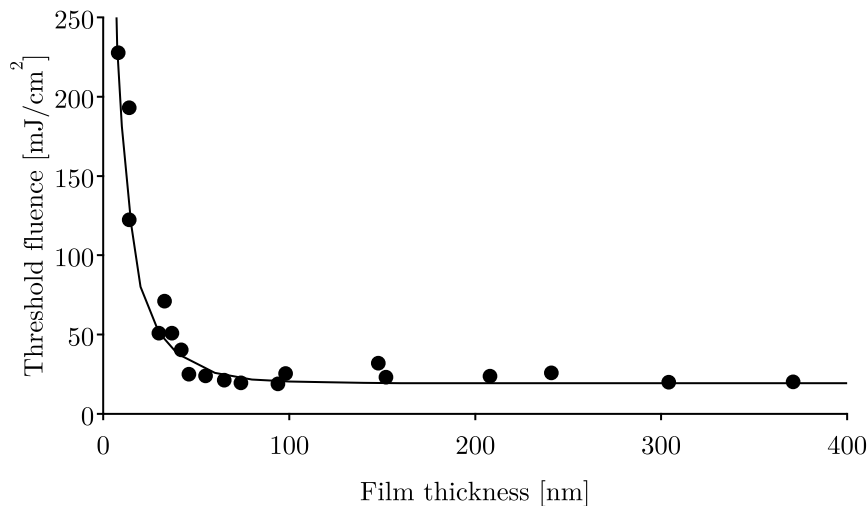
Figure 4.10 Measured ($\bullet$) and calculated (solid line) threshold fluence of the triazene as function of the film thickness. Substrate is fused silica.

The threshold fluence is constant at 20 to 25 mJ/cm^2 for films thicker than 50 nm. The absence of oscillations in the threshold fluence suggests a negligible interference between the beam reflected at the film/substrate interface with the incident beam. Below 50 nm, a steep increase of the threshold fluence with decreasing thickness is observed. The clear influence of the film thickness on the ablation threshold of TP was *a priori* not expected.

To understand this phenomenon a thermal model of the surface temperature evolution versus film thickness was developed as described in Section 3.1. The temperature profiles for film thicknesses between 10 and 400 nm were computed. The applied parameters are summarized in Table 4.1.

The absorption coefficients at 308 nm, α_{308}, are expressed relative to the base e, consistently with (3.12), and a pulse duration $t_{\mathrm{FWHM}} = 30$ ns was applied.

Table 4.1 Physical properties of the TP and the substrates

	α_{308} $[cm^{-1}]$	n_{308} $[-]$	κ $[W/cm\ K]$	χ $[cm^2/s]$
TP	$2.3 \cdot 10^5$	1.64	$1.3 \cdot 10^{-3}$	$1.0 \cdot 10^{-3}$
fused silica	$8.8 \cdot 10^{-1}$	1.49	$1.4 \cdot 10^{-2}$	$8.1 \cdot 10^{-3}$
sapphire	$1.7 \cdot 10^0$	1.81	$3.3 \cdot 10^{-1}$	$1.1 \cdot 10^{-1}$
PMMA	$6.4 \cdot 10^1$	1.55	$1.9 \cdot 10^{-3}$	$1.1 \cdot 10^{-3}$
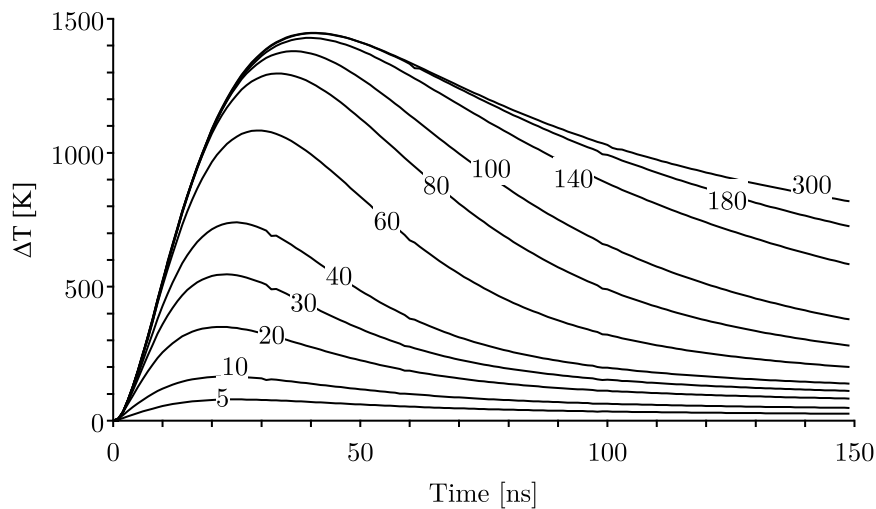
Figure 4.11 Evolution of the film surface temperature for different thicknesses of film (h [nm] written on each curve) at a constant fluence of 25 mJ/cm². Temperature is given relative to room temperature. Substrate is fused silica.

Figure 4.11 shows the result of the calculation as a temperature evolution of the film surface ($z = 0$) for a constant fluence, $\Phi_0 = 25$ mJ/cm², corresponding to the threshold fluence for thick films. Each curve corresponds to a different film thickness. It should be noticed that all temperatures are expressed relatively to the initial temperature (i.e. room temperature) and are not absolute temperatures. The model allows notably to calculate the peak temperature $T_{\max}$ reached by the film. It clearly appears that this maximum temperature of the film surface depends on the thickness. The thinner the film, the lower the peak temperature. Above 180 nm all temperature profiles tend to merge into each other and $T_{\max}$ approaches a constant value of $T_0 \approx 1450$ K.

Now for films thinner than 60-80 nm, no ablation occurs at 25 mJ/cm², contrary to thicker films. An obvious relationship between the peak temperature and the ablation onset must therefore exist. To quantify it, we consider that a certain temperature is needed for ablation to start. This temperature is defined as T_{th} and depends on both fluence and film thickness. For films thicker than 180 nm, this threshold temperature is T_0, which corresponds to the observed constant threshold fluence, while for thinner films

a higher fluence is needed to reach T_0.

Using the model, we recalculate the temperature profiles for each film thickness h by varying the fluence Φ. The fluence needed to reach T_0 is then the threshold fluence Φ_{th}, which satisfies the relation:

$$T_{\mathrm{max}}(h, \Phi_{\mathrm{th}}) = T_0 \tag{4.1}$$

The results of this calculation are shown in Figure 4.10 (line) together with the experimental data points. The model agrees very well with the experiment. A significant change in the calculated threshold appears below 100 nm. This originates from two effects. Firstly, the diminution of the absorbed photons starts to affect the ablation below the optical distance $h_{\mathrm{opt}} \approx \alpha_{\mathrm{eff}}^{-1}$. In this case, h_{opt} is 45 nm. The second effect is due to the large difference of the thermal conductivities between the substrate and the film. Below the thermal diffusion length, defined by

$$h_{\mathrm{th}} \approx \sqrt{2\chi_f t_l}, \tag{4.2}$$

the films start to be thermally influenced by the substrate (in this case $h_{\mathrm{th}} \approx 50$ nm). In the case of a better conducting substrate, it acts as a heat sink and a higher fluence is needed for the film to reach the threshold temperature.

The smooth transition from the fit curve to the theoretical limit in Figure 4.9 can now be explained. Heat diffuses faster from the polymer when the substrate is closer. The layer close to the substrate needs to receive more heat to reach the threshold temperature and to undergo ablation compared to the bulk polymer. As shown in Figure 4.10, the threshold fluence rises abruptly with decreasing thicknesses, thus explaining the asymptotic transition in Figure 4.9.

It has to be pointed out that our thermal model does not account for all possible terms in the heat balance. In particular, the exothemic decomposition of the triazene leads to a temperature increase in the order of several hundreds of K and heat removal may occur by fragments carrying away kinetic energy. These effects become important for a significant ablation depth. Considering the threshold fluence, we are at the point where the ablation depth is virtually zero, meaning that the decomposed amount of material is very low. If we compare the decomposition energy of a very thin layer with the energy provided by the laser pulse, the ratio converges to zero when getting closer to the threshold. The decomposition energy can therefore be neglected for predicting the threshold fluence. This explains why despite these simplifications, the model describes the experimental behaviour very well.

4.1.2.2   Influence of the substrate material

A detailed knowledge of the ablation behaviour with other substrates can give very useful information for two aspects. The validity of the model can be checked, which predicts

an influence of the thermal conductivities of the substrate on the threshold fluence. The other aspect is related to the envisioned application, i.e. LIFT. It will be advantageous for certain processes to use a polymeric material as substrate instead of fused silica. The influence of the substrate on the threshold fluence was therefore investigated with two others materials. Sapphire was chosen as a highly conductive material and PMMA as a low conductor. For the latter, the ablation threshold at 308 nm is high enough (900–1100 mJ/cm^2 [99, 100]) to ensure that the substrate does not undergo ablation in the investigated fluence range.

The influence of the substrate material on the threshold fluence is presented in Figure 4.12. The dots are the measured points while the lines represent the values calculated with the model, using the parameters in Table 4.1.
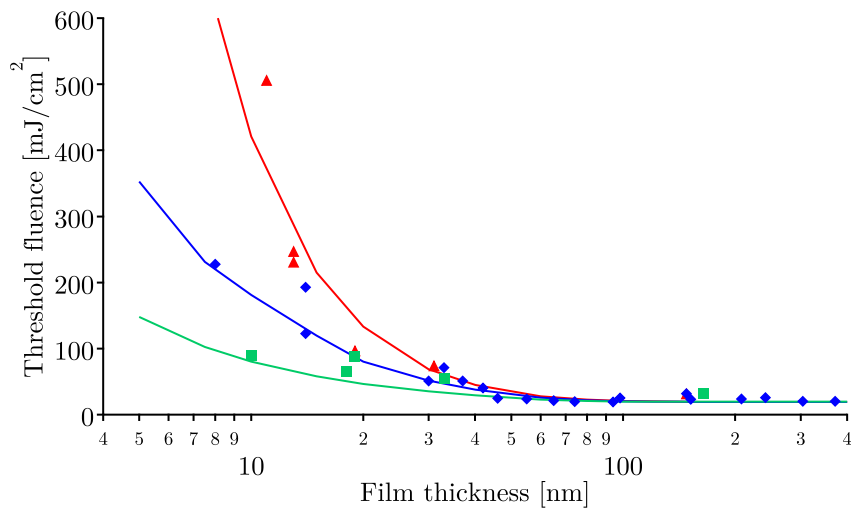
Figure 4.12 Influence of the substrate material on the ablation threshold. The points are experimental data: (△) sapphire, (◇) fused silica, (□) PMMA. The solid lines are computed from the model: (up) sapphire, (middle) fused silica, (down) PMMA.

The same effect of the thickness is observed for the two other substrates but, as predicted, with a different magnitude which depends on the material. Ablation on sapphire exhibits the strongest thickness-related effect, followed by fused silica, while the polymeric substrate (PMMA) has the lowest influence on the threshold fluence. The error on the fluence and thickness measurements is estimated to be ∼ 10%. Almost all experimental points fit the corresponding curve within the uncertainty. Although some points still deviate, the trend is a clear difference between the substrates.

The experiments confirm the validity of the model. The substrate with the higher thermal conductivity will absorb heat faster and thus reduce the maximum temperature reached at the film surface. On the opposite, PMMA has a thermal conductivity similar to TP and thus acts thermally as an extension of the TP layer. In this case the increase of the threshold fluence is mainly due to the reduced amount of photons absorbed within

the small thickness, as reported for the ablation of hydrogenated carbon films coated on an insulating substrate [101]. The data in Table 4.1 show that the absorption coefficient of PMMA is higher than for sapphire and fused silica. One could argue that it is not clear whether the lower thermal conductivity or the higher absorption is responsible for the observed effect. Considering that the absorption coefficient of PMMA is still more than one thousand times lower than of TP, the fluence absorbed by the substrate remains negligible.

4.1.2.3 Influence of the pulse length

According to Equation 4.2, h_{th} is affected by the pulse duration. To investigate this effect, the dependence of the threhold fluence on film thickness was investigated with the nanosecond (6 ns) and picosecond (70 ps) 355 nm lasers. Figure 4.13 shows the ablation curves obtained for the same film thickness (420 nm) with the three different lasers. The
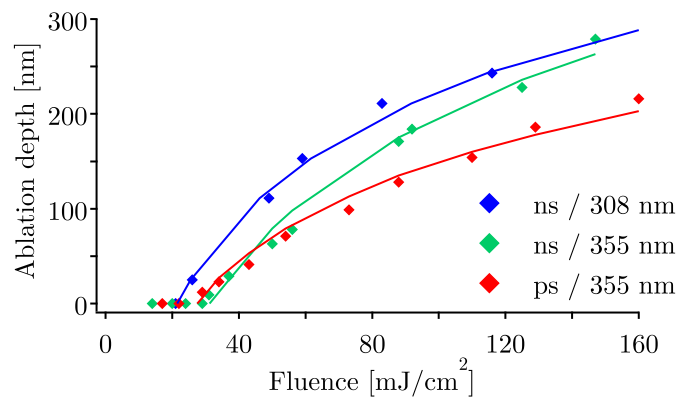
Figure 4.13 Comparison of the ablation curves for the 3 lasers with a 420 nm thick film. The points are data measured and the lines are the corresponding fit from Equation 1.5.

3 lasers are compared at first at the same film thickness well above the critical length for thermal diffusion to ensure that no thickness-related effects are present. A summary of the measured values with the three lasers is shown in Table 4.2.

Table 4.2 Threshold fluence and absorption coefficient of TP for the three lasers, together with the pulse duration.

Laser	Φ_{th} [mJ/cm^2]	α [cm^{-1}]	τ
ns / 308 nm	20–25	$2.3 \cdot 10^5$	30 ns
ns / 355 nm	24–32	$1.4 \cdot 10^5$	6 ns
ps / 355 nm	22–27	$1.4 \cdot 10^5$	70 ps

The ablation thresholds are very similar although the absorption coefficient at 355 nm is much lower (see Table 4.2). It corresponds to previous work where a threshold fluence of 25 mJ/cm^2 was reported for the ablation of TP at 351 nm with a 30 ns pulse duration.

The ablation rates are slightly lower at an irradiation wavelength of 355 nm compared to 308 nm, but interestingly, the nanosecond pulse removes more material at the same fluence than the picosecond pulse for fluences above 40 mJ/cm^2.

Figure 4.14 shows the threshold fluence versus film thickness for the three different pulse lengths.
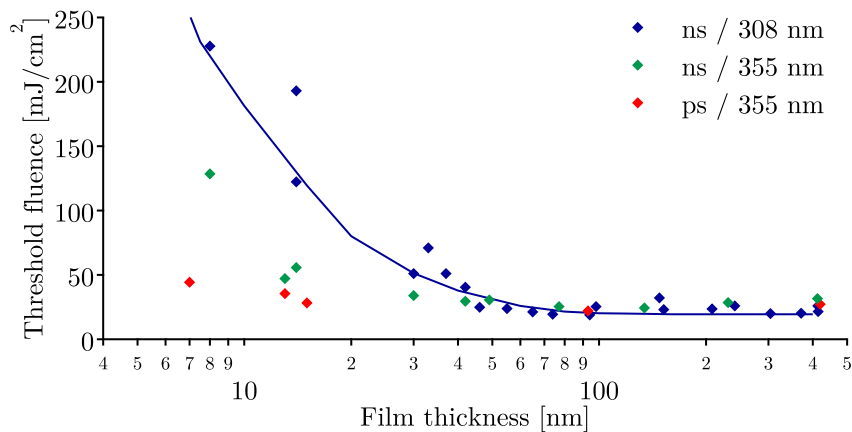
Figure 4.14 Influence of the laser pulse length on the ablation threshold. The points are measured data and the line for the ns / 308 nm pulse is calculated from the model. The substrate is fused silica.

The calculations with the model are not yet available as the code for the model has to be modified, nevertheless the data can be compared qualitatively. The threshold fluence increases with decreasing film thickness for the three lasers, but with a different magnitude. The longest pulse duration (30 ns, from the excimer 308 nm) corresponds to the steepest increase. Ablation with the ns / 355 nm laser (6 ns) exhibits a less pronounced increases, while the picosecond pulse (70 ps) produces the lowest increase of the threshold fluence with decreasing film thickness.

These results correspond to the expectations, i.e. ablation with shorter pulse duration is less sensitive to heat diffusion and therefore, the temperature required for ablation to occur is reached at a lower fluence for a film thickness below 50 nm. This suggests that the thermal model should also be able to predict the influence of the pulse duration on the threshold fluence, or at least qualitatively.

4.1.2.4   Considerations on the mechanism

This work shows that the thermal contribution plays an important role in the ablation of very thin triazene films, as discussed previously for thick samples [28, 40, 85]. However, it is difficult to conclude on the ablation mechanism from these experiments. As a

matter of fact, we focused specifically on very thin films and showed that their threshold fluence is higher than for bulk polymer, originating from thermal diffusion and a laser penetration depth larger than the film thickness. For thin films, it is possible to prove the thermal contribution in the ablation process, which is more difficult in bulk material. It may therefore not be feasible to extrapolate a general ablation mechanism from the observations on very thin films. Moreover, the mechanism consists of a mixture of thermal degradation, photochemical and thermally-activated photochemical bond-breaking, which cannot be quantified with the analysis of the threshold fluence and ablation rate. The threshold temperature is also "assigned" without relation to the thermal decomposition temperature. The nature of the mechanism cannot be assessed without a detailed analysis of the composition of the ablation products [34]. Additionally, it has been shown that a switch from photochemical to photothermal mechanism can happen with increasing laser fluence [32, 102, 103]. For these reasons, we believe that a definitive conclusion on the mechanism cannot be drawn from this work.

4.1.3   Back side ablation

Laser induced forward transfer proceeds from a film on a transparent carrier substrate irradiated from the back side of the substrate. The next step towards LIFT is therefore to investigate the ablation of the triazene from the back side. This is realised by turning the sample 180° relative to front side ablation. The results obtained with the excimer laser are presented first.

4.1.3.1   Excimer laser[3]

An overview of ablation spots created with the 308 nm laser at various fluences and number of pulses is shown in Figure 4.15. The films had a thickness of 540 nm, which is thick compared to the optical penetration depth of $a^{-1} \approx 100$ nm.

The spot at the lowest fluence was not ablated with 1 pulse. The edges of the ablation spot are visible, probably due to a slightly higher beam intensity at this location, corresponding to the observation for front side ablation. At the intermediate fluences, a skin of undetached yet delaminated material is present on the ablation spot. The spot at the highest fluence was completely ablated.

It is useful to compare the ablation depth obtained with front side and back side ablation to understand what happened. Figure 4.16 presents the crater depth measured on the film of Figure 4.15 and on a comparable film ablated from the front side.   The onset of ablation is shifted towards higher values for back side irradiation, but a full removal of the film is obtained at at fluence where only about half of the film is ablated under front side irradiation.

---

[3]A part of this section was published in [104].
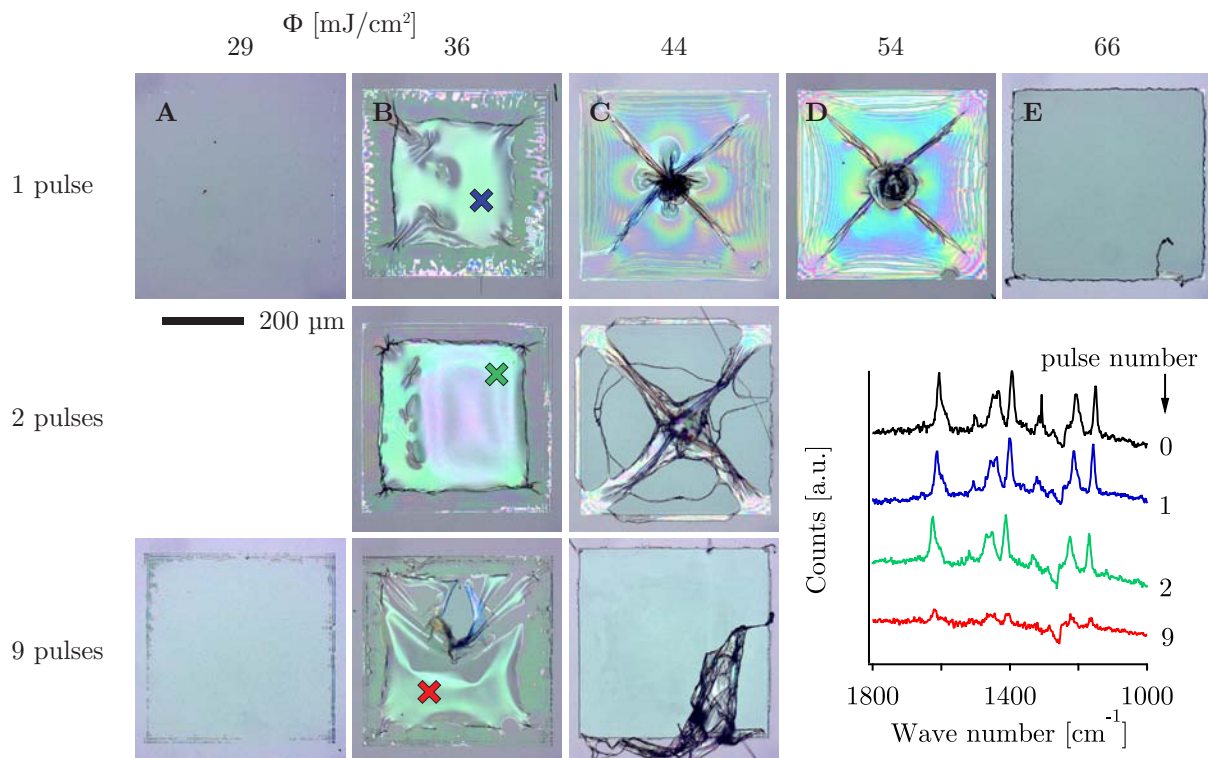
Figure 4.15 Optical microsopy pictures of back side ablation spots from a 540 nm thick TP film. The fluence increases from left to right and the number of pulses from top to bottom. The depth of the spots labeled with letters is reported in Figure 4.16. Inset: Raman spectra of the locations indicated by crosses at 36 mJ/cm^2. The zero pulse spectrum was measured on an non-irradiated location. The hole seen on the skin at 9 pulses of 36 mJ/cm^2 was done afterwards with the profilometer tip.

Above 36 mJ/cm^2, it appears from the plot that the fluence was not sufficient to ablate the whole film, however, a part of the film was ablated. As the laser impinged from the substrate side, ablation started at the boundary between the film and the substrate instead of the outer surface (polymer/air). In this way, only the part of the film close to the substrate was decomposed into gas and the top part remained solid. This is shown by the presence of the skin between 36 and 54 mJ/cm^2, whose appearance changes with the fluence and therefore with the thickness of the remaining layer. At 66 mJ/cm^2, the fluence was still too low to result in a complete ablation of the film. However, no skin is present on the ablation spot. In this case, the thrust caused by the decomposed layer was sufficient to eject the top layer. This skin ejection is discussed in more details in Section 4.1.4.2

Ablation from the back side was perfomed with multi-pulses as well. Selected ablation spots after 2 and 9 pulses are shown in Figure 4.15 in the two bottom rows. The edges of the irradiated spot after 9 pulses at the lowest fluence are more visible than after 1 pulses. This indicates that the fluence is slightly above the threshold at this location and that successive pulses achieve ablation, which is not the case in the center of the spot. This

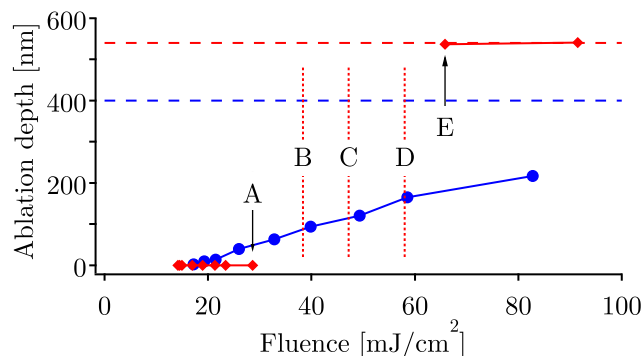**Figure 4.16** Comparison of the ablation depth between front side for a 400 nm thick film (blue) and back side for the 540 nm thick film shown in Figure 4.15 (red). The corresponding film thicknesses are indicated by the horizontal dashed lines. The letters refer to the spot in Figure 4.15 and the vertical dashed lines show the fluences where no profile measurements were possible due to the fragility of the "skin".

observation is in agreement with the ripple patterns obtained with front side irradiation at a fluence close to the threshold (see Figure 4.2 a).

At 36 mJ/cm^2, a skin layer is formed after 1 pulse already. Successive pulses do not change the aspect of the spot. It should be mentioned here that the hole seen on the skin layer after 9 pulses does not results from ablation, but was done accidentally with the profilometer tip during sample characterisation. The situation evolves at 44 mJ/cm^2, where the skin layer is progressively removed with successive pulses, although not completely. The remaining skin layer is progressively ablated until it is thin enough to detach. The points where the film remains connected are at the corners, where less strain is present due to geometrical reasons.

It is interesting that at 36 mJ/cm^2, the fluence is high enough to ablate the film, but successive pulses do not cause material removal anymore. The composition of the remaining skin was investigated by micro-Raman spectroscopy to understand this effect. The investigated locations are indicated with the coloured crosses in the picture of Figure 4.15 and the corresponding Raman signal is shown in the inset of that figure. The peaks around 1400–1500 cm^{-1} and 1200–1300 cm^{-1} are typical for the triazene group [105]. They are present with a very comparable intensity on the inact film and on the spot irradiated with 1 and 2 pulses, but they are almost not distinguishable after 9 pulses.

The similar intensity of the triazene peaks for 0, 1 and 2 pulses shows that a certain amount of triazene chromophores are present in the remaining skin layer. The absence of these triazene peaks after 9 pulses indicates that no triazene groups are present in the remaning layer, and therefore that this layer is composed of photodegradated material. It is in principle the same observation as described in Section 4.1.1 for multi-pulse front side ablation at a fluence close to the threshold. This explains why the skin layer is not completely ablated after 9 pulses at 36 mJ/cm^2, although the ablation depth for front

side ablation at this fluence ($\sim$ 100 nm, see Figure 4.16) would allow a complete layer decomposition after less than 9 pulses.

The formation of a top layer of undecomposed material is dependent on the fluence, but also on the initial film thickness. Two thinner film of 350 nm and 100 nm were investigated under the same conditions, with the 100 nm film having a thickness comparable to the laser penetration depth. An overview of single pulse ablation craters is shown in Figure 4.17.
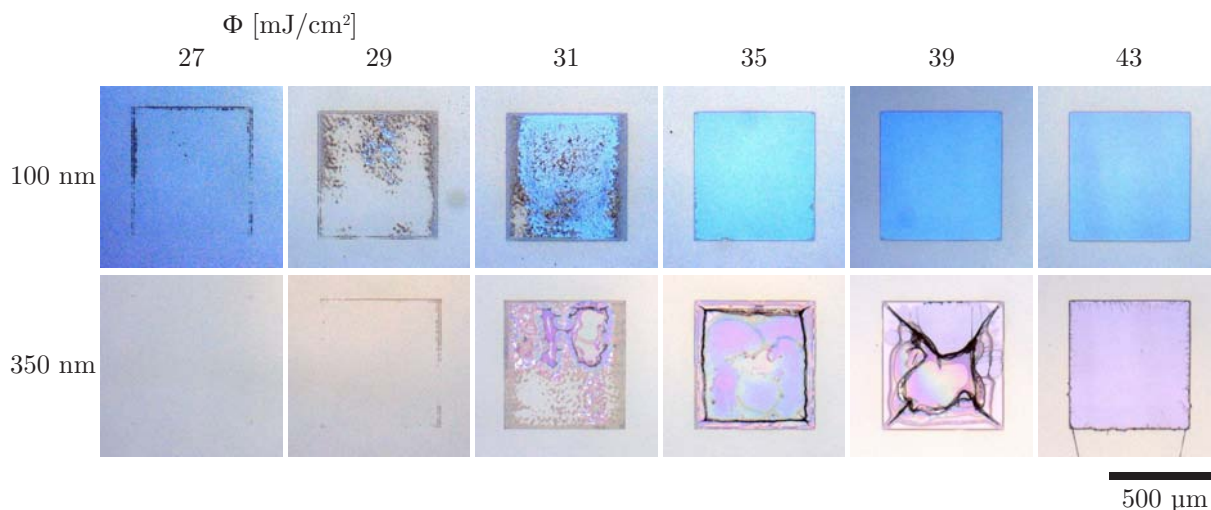
Figure 4.17 Optical microsopy pictures of back side ablation spots from 100 (top) and 350 nm (bottom) thick TP films. The fluence increases from left to right.

Back side ablation on a 350 nm thick film yields a similar behaviour as the 540 nm sample shown in Figure 4.15, with the formation of a skin layer, completely removed when the fluence is high enough. The situation is different with a 100 nm film. The spot is abruptly ablated when the fluence increases, without passing through the step of forming an undetached layer of polymer. In this case the film was too thin to form such as skin layer.

It is interesting to compare the fluence required to ablate films of different thicknesses. The fluence required to achieve a complete removal of the film depends strongly on the film thickness. While the film of 100 nm is fully ablated at 35 mJ/cm^2, more than 40 mJ/cm^2 are needed for the 350 nm thick film and even above 60 mJ/cm^2 for the thickest film of 540 nm. For complete ejection of the polymer film enough thrust is required to overcome the resistance of the remaining layer. There should be an equilibrium between the resistance to shear of the edge, depending on the remaining thickness, and the pressure created, related to the ablated depth. At a certain fluence, the ratio is favorable to top layer ejection. Thicker films need a higher fluence in order to reach this point.

The ablation threshold, about 28 mJ/cm^2, seems to be much less dependent on the film thickness, although a slight increase is observed. The onset observed corresponds to the creation of gas cavities, whose creation is counteracted by the resistance of the film,

which increases with its thickness. Therefore, a thicker film requires more fluence for the gas bubbles to appears. However, this effect is much less important than for the top layer ejection.

4.1.3.2   Nd:YAG laser

Back side ablation was investigated with the picosecond laser setup as well. A series of ablated spots from a 300 nm thick TP film is shown in Figure 4.18.
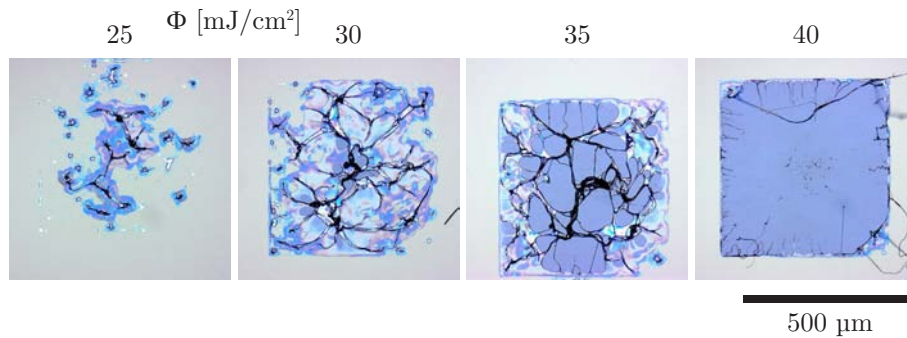
Figure 4.18 Optical microsopy pictures of back side ablation spots done with the ps / 355 nm laser on a 300 nm thick TP film. The fluence increases from left to right.

The film is ablated in an inhomogeneous way, as seen from the spot at 25 mJ/cm^2, where ablation happened only at certains locations within the irradiated area. When the fluence was increased, the ablated area expands until it covers the whole spot. Eventually, the complete layer is removed. There is no formation of a skin layer covering the whole spot. In this case, the beam profile was too irregular to provide the same fluence to the whole surface. The different stages from skin formation to complete delamination, described above for irradiation at 308 nm, are present on the same ablation spot according to the actual fluence impinging at that location. In this way, very localised skin formation is seen next to unablated areas. These observations corresponds to the depth profile obtained by front side ablation and to the beam profile shown in Figure 4.8. While the inhomogeneity of the beam results in differences in ablated depth within the profile, the consequence of these inhomogeneity for back side ablation are dramatic differences between fully ablated and intact zones.

As a consequence of this differential ablation, the onset is less well-defined. It appears however that the 300 nm thick film is already partially ablated at 25 mJ/cm^2 and fully delaminated above 40 mJ/cm^2. The latter value corresponds to the 350 nm film processed with the excimer laser, but the onset seems to occur at at lower value. A similar comparison between front and back side irradiation with a femtosecond pulses has even shown that the threshold fluence of ablation is much lower for back side irradiation (only 20% of the threshold fluence for front side) [106, 107].

The ablation threshold of front side ablation is very similar for both lasers, suggesting that the difference does not originate from it. The picosecond pulse may create a more abrupt pressure jump at the ablation spot and achieve the gas cavitiy formation cited above at a lower fluence, thus explaining this difference. However the fluence is only an average over the whole spot and the actual energy distribution may yield much higher fluences locally. A definitive conclusion about the effect of the pulse duration on the back side ablation threshold is therefore not possible.

In a general way, back side ablation reveals the same dependence of the ablation depth on the fluence which is well known for front side ablation, but with a much sudden jump in the ablated depth versus fluence, corresponding to the complete film removal. This is specially visible in Figure 4.16. It is expected that this fact has a considerable influence on the material ejection and transfer. In this view, we believe that the use of a flat energy profile is required to achieve LIFT.

It appeared as well that a part of the triazene film is not decomposed but ejected upon back side ablation. This effect may be very important for the application of a sacrificial layer for LIFT, because the sacrifical layer is intended to be decomposed completely and not be deposited with the donor material. The next section deals with the material ejection from a donor substrate, starting with a single triazene film.

4.1.4   Time resolved imaging[4]

After the investigation of the ablation of triazene films, the ablation process was followed in real time by a time-resolved lateral imaging technique. The goal of the experiment is to study the ablation dynamics and measure the velocity of the features created by ablation (shock wave, products and flyer). The knowledge of the propagation velocity gives access as well to the energetics of the process, which is discussed in detail below. First, the ablation process is evaluated qualitatively.

4.1.4.1   Front side ablation

Ablation from the front side has been studied first, because most reference data exist for this configuration and therefore allow a comparison with literature data. It is also the most simple configuration, since the volume of ablated material is directly accessible from the crater depth measurement. A sequence of pictures taken at $110 \, \mathrm{mJ/cm^2}$ for a 500 nm thick triazene polymer film is shown in Figure 4.19. The film surface is on the right, while the laser pulse comes from the left.

Two propagating features can clearly be distinguished in the images. The first moving front (feature A in Figure 4.19) is attributed to the shock wave caused by the pressure jump at the ablation spot. This pressure jump originates from the large volume increase by the decomposition of the triazene polymer and from the fast thermal expansion of the

---

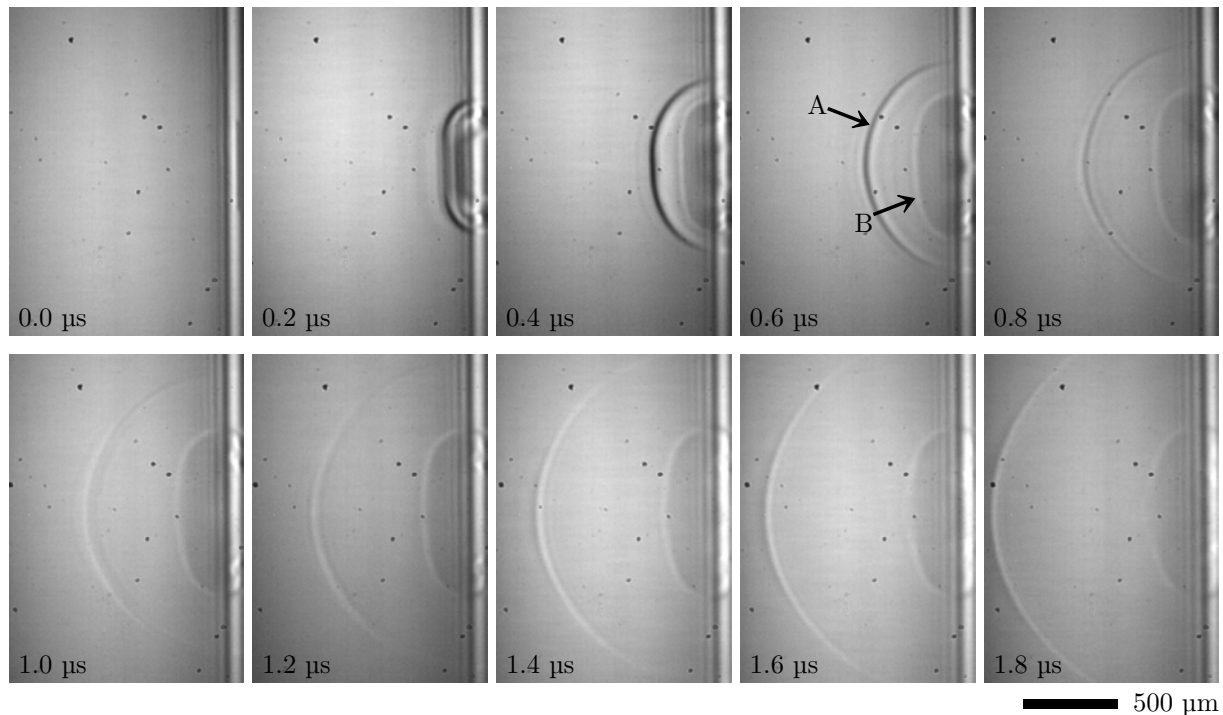[4]The content of this section was published in [108].

Figure 4.19 Sequence of pictures taken for front side ablation of a 500 nm triazene polymer film at 110 mJ/cm^2. The laser comes in from the left, while the substrate is on the right. The time delays are indicated in the frames. The arrows show the features A and B described in section 4.1.4.1.

materials (gas and solid) upon heating by the laser pulse. The shock wave propagates first in a piston-like motion (at 0.2 µs), when the propagation distance is shorter than the width of the ablation spot. The shock front tends to become hemispherical when the distance increases, as expected for a point-like ablation spot [109].

The second observable feature (indicated as B in Figure 4.19) is most probably formed by gaseous decomposition products from the polymer. The shape evolution of this product front is slightly different from the shock wave. The expansion is slowing down very quickly, maintaining a flat shape. The presence of the shock wave and the gas front corresponds to observations from previous work on thick films of a slightly different triazene polymer [87]. It is remarkable that no particles are visible in the ablation plume, which confirms a clean and debris-free ablation of the triazene, which was also observed previously.

The above described observations are also valid for a 190 nm thick sample (not shown). The ablation threshold fluence strongly increases for thinner films with thicknesses below 50 nm (as shown in Section 4.1.2.1), due to heat diffusion and reduced absorption. Therefore, a change in the behaviour can be expected for films thinner than 50 nm.

4.1.4.2   Back side ablation

The corresponding configuration to analyse the LIFT process is back side ablation. A sequence of pictures taken for a 460 nm thick triazene polymer film at a fluence of

110 mJ/cm^2 is presented in Figure 4.20. The samples are rotated by 180° with re-
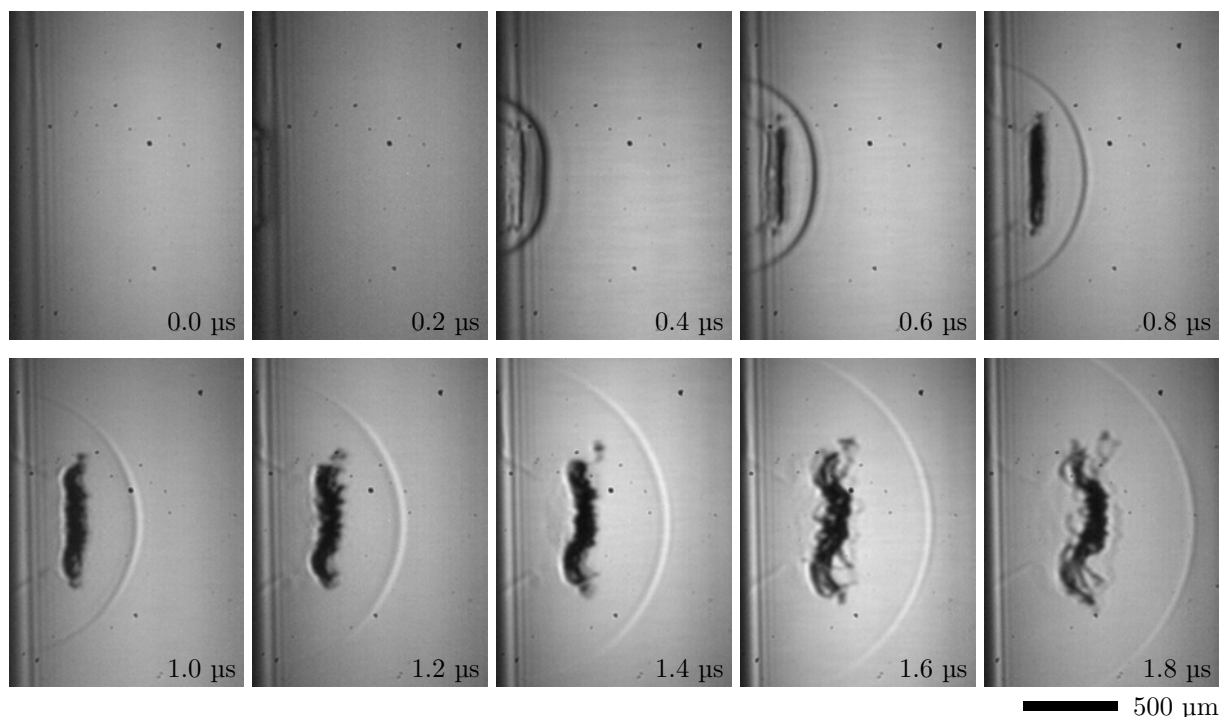
Figure 4.20 Sequence of pictures taken for back side ablation of a 460 nm triazene polymer film at 110 mJ/cm^2. The time delays are indicated on the frames.

spect to front side ablation (in Figure 4.19). The shock wave is also visible with a similar shape and expansion properties as observed for front side ablation. The main difference is the replacement of the product front seen in Figure 4.19 with an opaque object ejected from the substrate, i.e. a *flyer*, which becomes visible 0.4 µs after the irradiation. The flyer has initially a well-defined flat shape, corresponding to the ablated spot of the polymer film. Then it expands, becomes distorted and looses its initial shape.

The presence of the flyer shows that the entire triazene layer is not ablated by a single laser pulse at this fluence. The flyer consists of undecomposed polymer, which is ejected by the pressure thrust created during ablation and decomposition of the underlying part. This partial ablation upon back side exposure corresponds to the observations described in Section 4.1.3 for back side irradiation. The presence of an undecomposed layer of triazene on the receiver substrate after transfer of a single TP layer will be discussed in a following section.

4.1.4.3 Effect of film thickness and fluence

The formation of a flyer requires that a certain amount of material stays intact, or at least, in the form of a compact product layer. The appearance, shape and properties of the flyer should depend on the irradiation fluence because the latter will determine the ablation depth, and therefore the thickness of the remaining polymer. The film thickness should

also play a similar role, because for a given fluence, a thin film will be fully decomposed with no flyer present. To verify this assumption, samples with two film thicknesses (190 nm and 460 nm) were investigated for various fluences. A summary of these experiments is given in Figure 4.21 (a) and (b), where the time delay was kept constant at 1.2 µs. Corresponding optical microscopy pictures of the 460 nm thick sample after ablation are shown in Figure 4.21 (c).
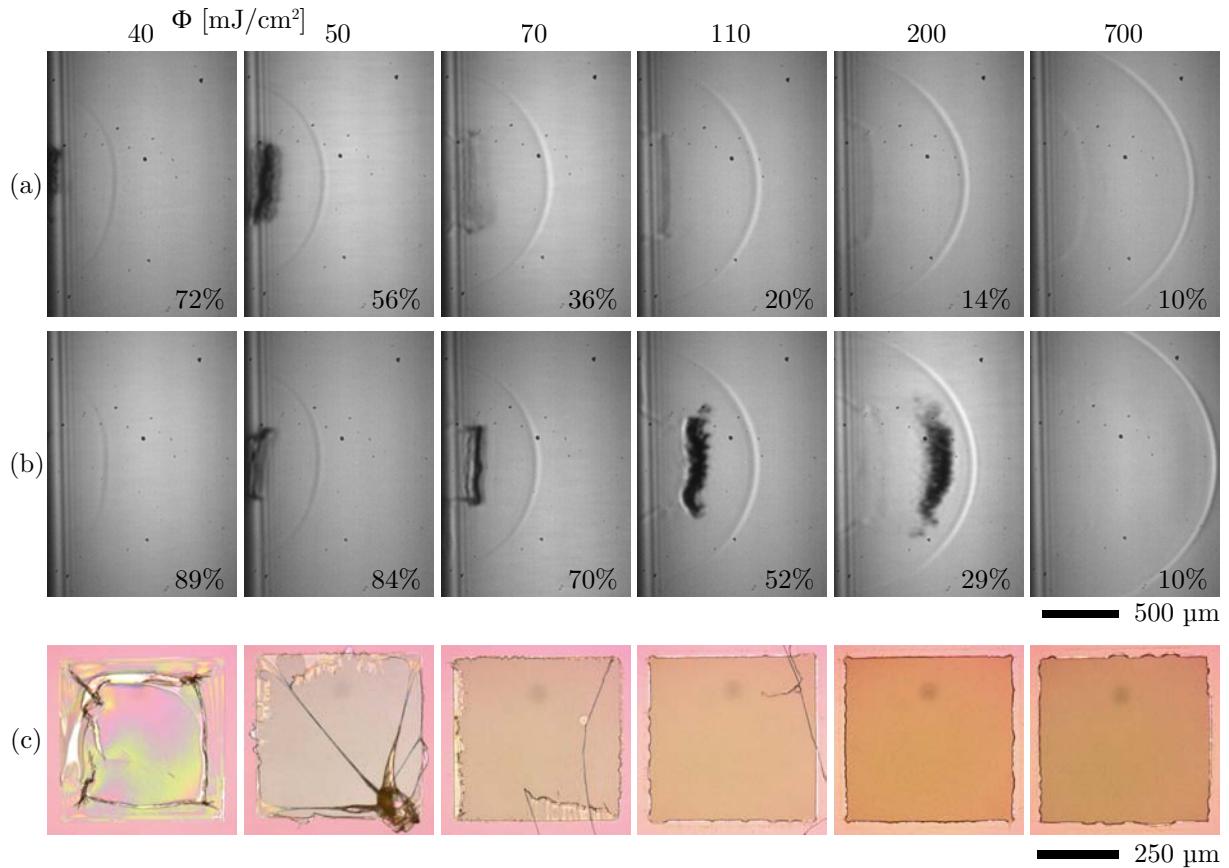
Figure 4.21 Pictures of back side ablation taken after 1.2 µs with 190 nm (a) and 460 nm (b) triazene polymer films at increasing fluences (from left to right) and the corresponding ablation spot microscopy images of the 460 nm triazene sample (c, at a different scale). The percent value on the pictures is the calculated undecomposed ratio (see section 4.1.4.3 for details).

In the case of the thicker film (Figure 4.21 b) at a fluence of 40 mJ/cm^2, which is close to the threshold fluence of 25 mJ/cm^2, no flyer is observed and only the shock wave is visible. The corresponding microscopy picture shows the presence of a remaining skin layer at the ablated spot, which has probably been expanded and deflated after the pulse, in accordance to previous observations in Figure 4.15. In this case, no ejection of the top layer occurred, because the generated pressure was not sufficient to expel the top layer. A flyer can be observed when the fluence is increased. At 50 mJ/cm^2, the flyer remains very close to the substrate and seems not to be completely detached from the remaining polymer. The residues on the ablated spot confirm that a part of the flyer remains linked

to the donor film, i.e. mainly at the corners [104], where polymer threads are visible. The flyer exhibits a good flat shape for an irradiation fluence of 70 mJ/cm^2, but the upper and lower parts seem to be still connected to the initial film. Above 110 mJ/cm^2, the flyer is clearly detached and no residues are present in the ablation spot. However, the shape of the flyer starts to be less well-defined and its size increases, together with its ejection speed. This can be assigned to the decreased thickness and therefore lower mechanical stability of the flyer. This fact is even more pronounced at 200 mJ/cm^2, where the flyer contours become more cloudy. Eventually, no flyer is visible and the whole layer of donor film is decomposed into gaseous products at a fluence $\geq$ 700 mJ/cm^2.

With increasing fluence, the penetration depth of the laser increases and a thicker layer of material is decomposed, generating more gaseous species, i.e. pressure to cause the ejection of the flyer. At the same time, the remaining film thickness decreases. With increasing fluence more energy is available to eject a flyer with a decreasing thickness which results in faster destabilisation of the flyer. The final scenario is reached when the whole triazene layer is ablated.

The effect of fluence on the thinner film (190 nm) is similar except that the flyer gets decomposed at lower fluences. Figure 4.21 (a) shows shadowgraphy pictures for the 190 nm thick triazene sample. At 40 mJ/cm^2, a partially detached cloudy piece is already visible, although no flyer is ejected. The best flyer, i.e. the flyer which has the best chance to yield a good deposition, is visible for a fluence of 50 mJ/cm^2. The flyer becomes less visible when the fluence is further increased and for 70 mJ/cm^2, it is not clear whether a solid flyer or only a cloud of gaseous species and fragments are ejected. Above this fluence, only gaseous ablation products are observed which have a similar appearance for a fluence of 200 mJ/cm^2 as the features observed for front side ablation.

For a given film thickness, the quality of the flyer changes constantly with an increase of the fluence. The best quality, i.e. flat shape and compact aspect, is reached for an intermediate fluence for both polymer thicknesses. However, this optimum fluence is higher for the thicker sample (between 70 and 110 mJ/cm^2) than for the 190 nm film (around 50 mJ/cm^2). The thickness of the flyer was estimated in order to quantify this difference in optimum laser fluence. The ablation depth of the corresponding films was measured for front side ablation and is assumed to be the same for back side ablation. The values are shown in Figure 4.22 (a), together with the depth normalised by the initial film thickness (b).

The flyer thickness should then be equal to the film thickness minus the ablated depth. This assumption is easy to calculate and should give a good approximation of the flyer thickness. The result is best expressed in terms of percentage of the initial thickness for a better comparison and indicated in the corresponding pictures in Figure 4.21.

The optimum value to get a good yet well separated flyer is between 60 and 80% of undecomposed layer. The sharpness of the flyer shape decreases strongly when this ratio is smaller than 50%. Eventually, the flyer is completely decomposed into fragments and
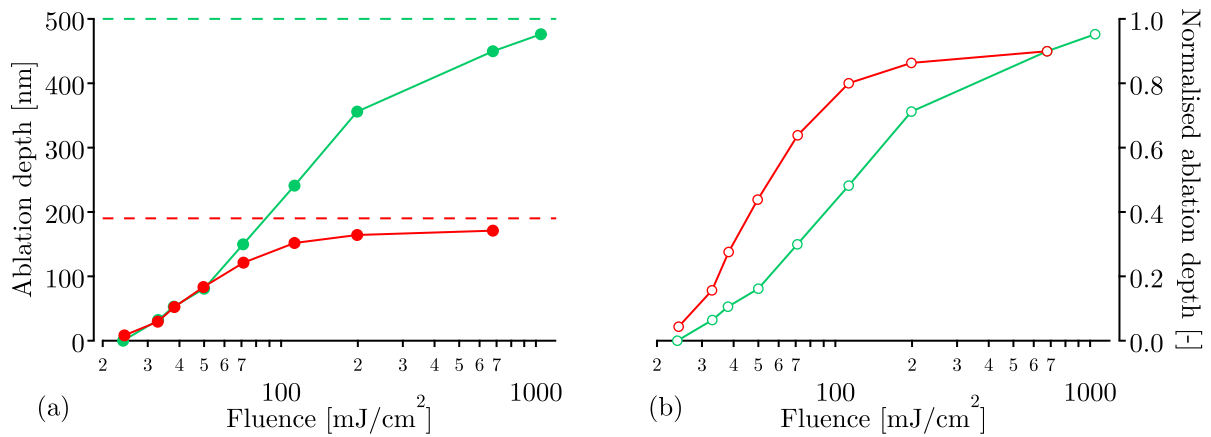
Figure 4.22 (a) Ablation depth versus fluence for front side ablation of the 500 nm (green) and 190 nm (red) triazene films corresponding to the samples in Figure 4.21. The respective film thickness is shown by the dashed lines. (b) Ablation depth normalised by the film thickness for the 500 nm (green) and 190 nm (red) triazene films.

gaseous species when the theoretical part of unaffected triazene thickness lies between 20 to 30%.

The percentage of undecomposed polymer seems to be a useful value for characterizing the process. A direct comparison of the images generated from the 460 nm and 190 nm thick films at the same fluence reveals that the flyer from the thinner film is faster and thicker. Indeed, the ratio of undecomposed polymer is quite different for both samples. A direct comparison of the flyer properties should only be valid for fluences where a similar percentage of undecomposed thickness is obtained, i.e 50 mJ/cm^2 for 190 nm and 110 mJ/cm^2 for 460 nm. In this case, both flyers have a comparable shape, but the flyer from the thicker sample is faster. This suggests that the calculated ratio is a good estimation of the flyer state and behaviour, but additional effects are also important. The laser energy and the absolute amount of decomposed material play an important role in the process. A comprehensive estimation of the energy balance is presented below to understand the system in more detail.

4.1.5   Energy balance[5]

4.1.5.1   Shock wave propagation

The analysis of the shadowgraphy pictures provides quantitative information as well. The propagation velocity of the shock wave and flyer were measured and the model shown in Section 3.2 allows then to estimate the energy of these objects and to compare it with the input energy of the laser.

---

[5]The content of this section will be submitted for publication.

The position of the shock wave was measured from the images and plotted versus the time elapsed after the beginning of the ablation pulse (Figure 4.23, various symbols). The lines are fit curves as explained below. The data for front and back side irradiation are shown at a high (700 mJ/cm^2) and low fluence (50 mJ/cm^2). The latter fluence was chosen because it is just above the ablation threshold for a complete film delamination upon back side irradiation, as shown in Section 4.1.4.3.
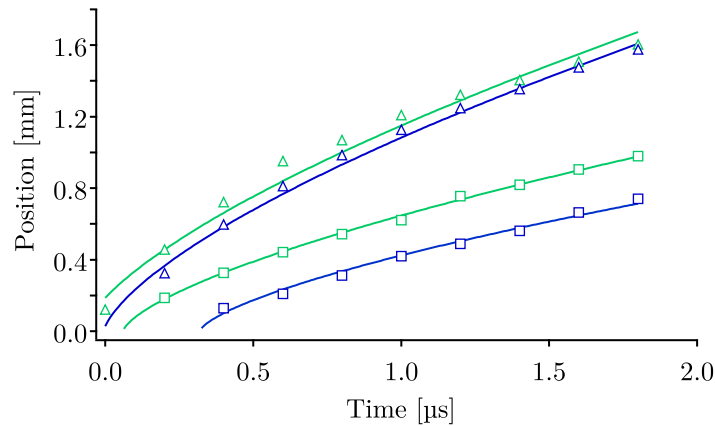

Figure 4.23 Points: position of the shock wave front versus time measured perpendicular to the sample for front side (green) and back side ablation (blue), each at two fluences: ($\triangle$) 700 mJ/cm^2, ($\square$) 50 mJ/cm^2. Lines: corresponding fit curves.

The shock waves exhibits a typical deceleration, due to the distribution of the initial energy into a increasing volume of air. The velocity of the shock wave is, as expected, faster at the high fluence. However, two features are remarkable. The trajectories for front side and back side ablation overlap well at the high fluence, but are clearly different at 50 mJ/cm^2. The second interesting fact is that the shock waves seem not to start at the same time, if we consider the apparent interception of the trajectories with the time axis ($x = 0$) as the starting time of the shock wave propagation. At 50 mJ/cm^2, the shock generated by back side ablation seems to start hundreds of nanoseconds after the shock wave generated by front side irradiation. We can exclude an artifact of the measurement, because the uncertainty on the reference point for the position (i.e. the surface of the sample) is much less than the observed 200 µm. Moreover, a systematic error between front and back side measurements would not explain the difference between the curves, because a shift of all curves for back side with respect to front side curves would shift the difference to other fluences but not cancel it.

The main difference between front side and back side ablation at low fluences is the presence of a flyer in the latter case. This layer of undecomposed polymer is ejected when the fluence is not high enough to ablate the whole triazene film, yet sufficient to delaminate and propel the remaining part. Thicker flyers are obtained at fluences just above the delamination threshold, i.e. the minimum fluence required for complete material

removal from the ablated spot. For a given layer thickness of 460 nm, it is between 40 and 50 mJ/cm^2, as shown in Section 4.1.4.3. Interestingly, the fluence range at which the major differences in the shock wave evolution appear is where a thick material flyer is ejected. When the fluence is increased, the flyer becomes thinner until it is not visible anymore (at 700 mJ/cm^2), and correspondingly, the trajectories of the shock wave tend to overlap. It is clear that the flyer thickness is directly related to the shock wave evolution. To understand the phenomenon the energies involved in the processes are analyzed.

4.1.5.2   Energy balance

The energy released in a shock wave can be computed from its trajectory. The position is fitted versus time with Equation 3.33 and the result is shown as solid lines in Figure 4.23. The applied parameters are summarised in Table 4.3.

Table 4.3 Fit parameters

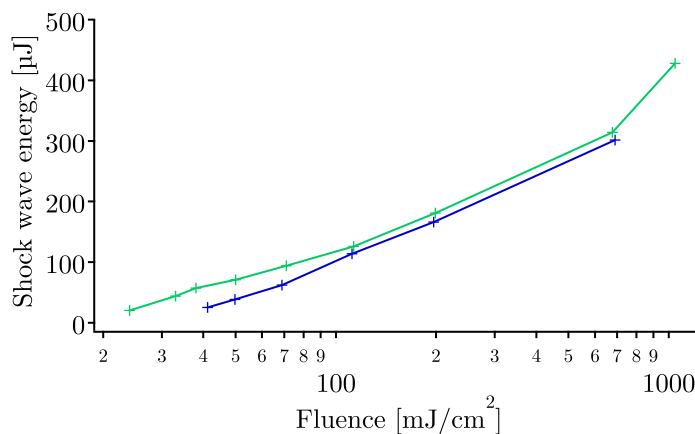| Name	Symbol	Value	Unit
Area	A	$2.5 \cdot 10^{-7}$	m^2
Substrate transmittance	T_s	0.92	-
Decomposition enthalpy	$\Delta_{\text{dec}}H$	$6.97 \cdot 10^5$	J/kg
Adiabatic ratio	γ	1.4	-
Density of triazene	ρ_f	$1.12 \cdot 10^3$	kg/m^3
Density of air	ρ_g	1.184	kg/m^3

Figure 4.24 Shock wave energy versus laser fluence for front side (green) and back side ablation (blue).

The best fit is obtained at intermediate fluences (not shown), while at the highest fluence, the fit line is less curved than the actual data points, suggesting that a hemisherical model would be slightly more suitable in this case [87]. The data points at 50 mJ/cm^2 are

correspondingly more linear than the fit line, probably because the shock wave weakens when the fluence gets closer to the ablation threshold. Eventually, it converges to a plain sound wave, that propagates linearly [109]. However, the same model was applied for all fluences to obtain consistent data.

The fit provides two parameters, the time delay t_0, discussed further in Section 4.1.5.3, and the initial energy E_{SW}. This energy is plotted versus the incident laser fluence in Figure 4.24 for both front side and back side ablation. The shock wave energy increases as expected with the fluence with both curves following the same trend. However the shock wave energy for front side irradiation is consistently higher and pronounced differences are observed at low fluences. A representation of the normalised energies, according to Equation 3.28, is better suited to enhance the difference.
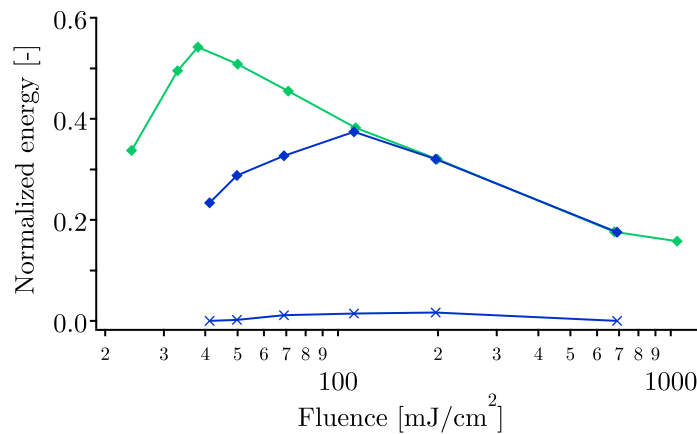
Figure 4.25 Normalized energy versus laser fluence for the shock wave at front side (green) and back side ablation (blue), as well as for the flyer in the case of back side ablation (×).

Figure 4.25 (⋄) shows the normalized shock wave energies versus incident fluence. A value of 1 corresponds to a complete transfer of the input energy into the shock wave. It is noteworthy that the points between 110 and 700 mJ/cm^2 overlap better than in Figure 4.24 due to the fact that the transmission of the fused silica substrate (92%) is now included for back side ablation. The data point at the lowest fluence correspond to no ablation (front) or no flyer ejection (back) for each curve.

The energy of the shock wave lies between 20% and 55% of the total energy. This order of magnitude is realistic and the values reveal that a significant part of the energy is used for the loss processes described in Section 3.2. Both curves reveal a maximum value, though at a higher fluence for back side irradiation. It is not yet clear why a maximum is reached, but this may be related to the procedure of calculating the laser energy. For this calculation we assume that the laser light is completely absorbed, which may be incorrect at low and high fluences, for the reasons discussed below.

When the fluence decreases and gets close to the threshold fluence, a dramatic decrease

of the ablation depth occurs, being eventually zero at the threshold. The volume of gas released decreases accordingly. As mentioned above, the shock wave is created by a pressure jump at the ablation spot, which is provided by the volume increase and by thermal expansion of the materials. When the gas volume diminishes, the shock wave is weaker. At high fluences, the ablation depth is similar to the film thickness and a part of the laser light is transmitted through the sample, thus decreasing the energy available in the balance. However, it was noticed that applying the linear absorption coefficient for the energy calculation results in unrealistic values ($> 100\%$) at low fluences, where the affected thickness tends to zero. Indeed, a shock wave was even visible at 24 mJ/cm^2 where no ablation was detected. For this reason, we believe that the total pulse energy is a good yet simple value for the input energy.

More interesting is the comparison between both curves. The trend seen in Figure 4.24 appears even more clearly in Figure 4.25, i.e. a difference of a factor of 2 for the shock wave energy at low fluences between front side and back side irradiation. The largest difference is observed at 40 mJ/cm^2, where for back side irradiation a part of the film is decomposed but no flyer is ejected. When the fluence is increased, the difference decreases until vanishing at 110 mJ/cm^2, corresponding to a estimated flyer thickness of 50% of the original film.

One possible approach to explain these data is to take the kinetic energy of the flyer into account. The flyer position was therefore measured and fitted versus time with a linear relation (not shown). The slope of this line gives the velocity, v_{flyer}, used in Equation 3.36 to calculate the kinetic energy of the flyer. The obtained normalized energy is included in Figure 4.25 ($\times$). The calculated maximum value was just above 2%, which is much too low to explain the difference in the shock wave energies. Moreover, the maximum of the curve is found at 200 mJ/cm^2, where both shock waves have the same energy. The energy used to accelerate the flyer does therefore not explain the observed difference.

Another possible explanation may originate from the different geometries of both systems. They are very different at low fluences, which has implications for the heat transfer and the mechanical energy. We have shown previously that highly thermally conductive substrates, such as fused silica, are major heat sinks during ablation of films thinner than 50 nm [91]. When ablation is performed from the front, energy losses occur by the heat transfer through the remaining polymer layer and further into the fused silica. However, the influence of the substrate is low because the triazene insulates thermally the ablated area. The case is different during back side ablation. The decomposed zone is located between the fused silica and the remaining triazene layer. The latter is heated in a way comparable to front side ablation, with the substrate as an additional heat sink. It can be expected that an important part of the thermal energy is lost into the fused silica because the ablated zone is not insulated from the substrate. At high fluences, the undecomposed triazene layer is thinner or zero and the two irradiation geometries are similar. This effect can explain the observed difference quite well.

The influence of mechanical processes is different as well. During front side ablation, the ablation products are freely ejected into the atmosphere and mechanical losses only happen by the shock wave recoil into the substrate. When a flyer is ejected, the edges of the flyer have to be detached from the surrounding film, which requires additional energy. Further investigations are being carried out to quantify this amout. Moreover, the shock wave is created in the ablated zone, i.e. between the flyer and the substrate, but is observed in front of the flyer. The shock wave must therefore travel through the polymer film, which will be the flyer, before propagating into the ambient air and may loose energy by polymer heating during this crossing. This possibility is discussed further to explain differences of the observation time in the shock wave appearance.

Finally, another reason for the weaker shock wave in the presence of a flyer may be a partial reflection of the shock wave at the polymer/air interface when the shock wave reaches the external film surface after travelling through the undecomposed layer, which may cause an additional energy loss.

4.1.5.3 Delay

As seen in Figure 4.23, the shock waves are best approximated when a time delay is introduced into the fit equation. These t_0 values are shown in Figure 4.26 for front side and back side ablation. A positive delay means that the shock wave is observed after the laser pulse (reference point at the top of the main intensity peak).
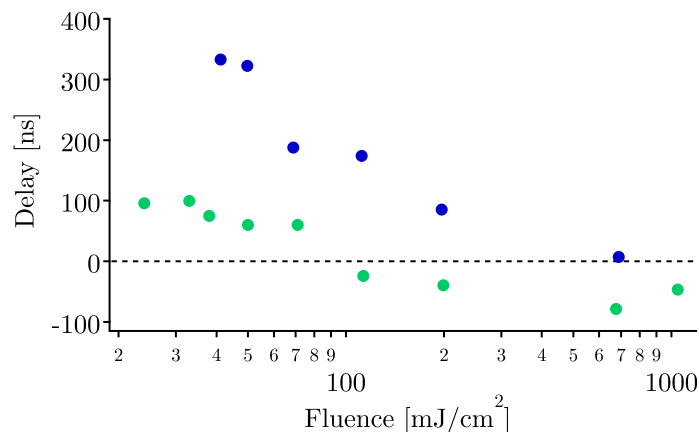
Figure 4.26 Delay of the apparent time origin of the shock wave with respect to the ablation pulse (parameter t_0 from fit), plotted versus laser fluence for front side (green) and back side ablation (blue). A positive delay represent an origin after the laser pulse.

An increasing delay time is observed for decreasing fluences, and the delay is larger for back side irradiation. The delay is negative at high fluence for front side ablation, which is of course unreasonable. It indicates that the equation curve does not describe the early points correctly. At the low fluences, however, the trend is in accordance with

the observed shock wave trajectories, i.e. shock waves generated by front side irradiation start earlier than those from back side ablation.

The reason for this difference in the delay is not clear. Even the sound propagation in the flyer, which may be slower than in air, cannot explain it. Assuming a speed of sound for rubber-like material ($\sim$ 40 m/s), which is the extreme case for a slow propagation medium, the time for crossing an entire flyer would be only around 10 ns, which is at least one order of magnitude shorter than the observed time delay. There may be other reasons responsible for this delay, related to the geometry of the cavity where the flyer is formed.

The explanation may also be related to the domain of validity of the equation describing the shock wave. The delay may correspond to the time the shock front needs to reach a hemispherical shape, where the equation can describe the data points very well. Below this time, the geometry of the shock wave is still transient and the fit equation is not able to describe the points correctly. This possibility was suggested by other authors as well [110, 111].

4.2 Material ejection

4.2.1 Ejection of a metal layer

The next step towards the deposition of pixels is to investigate how a layer of donor material coated on the triazene polymer is delaminated and ejected upon back side ablation. For these experiments, a model system made of triazene/aluminum was chosen. The transfer of metal patterns has both theoretical and practical interests. As explained in Section 2.1, this configuration was a simplified model of an OLED pixel but easier to prepare and not requiring the expensive MEH-PPV. There is also a technological interest to direct-write metal patterns, for instance as electrical contact on microelectronic devices.

For all the experiments, a constant layer thickness of 80 nm of aluminum was chosen. The samples were investigated using shadowgraphy imaging, thus allowing to reveal the shape and flight of the ejected pixel. An overview of an ejected flyer is shown first.

4.2.1.1 Aspect of the flyer

A sequence of pictures obtained with a 350 nm TP / 80 nm Al film upon back side irradiation at a fluence of 360 mJ/cm^2 is shown in Figure 4.27.

The pictures reveal the creation of a shock wave followed by the ejection of a material flyer. The propagation of the shock wave is similar to the observations for back side ablation of a single TP layer, i.e. the shock front evolves from a flat shape to a hemispherical propagation. The flyer is ejected with a very flat shape and travels intact across a distance of about 500 µm. After 1 µs, the flyer starts to loose its original flat shape and becomes wavy. In the same time, some fragments detach from the flyer in the forward direction and
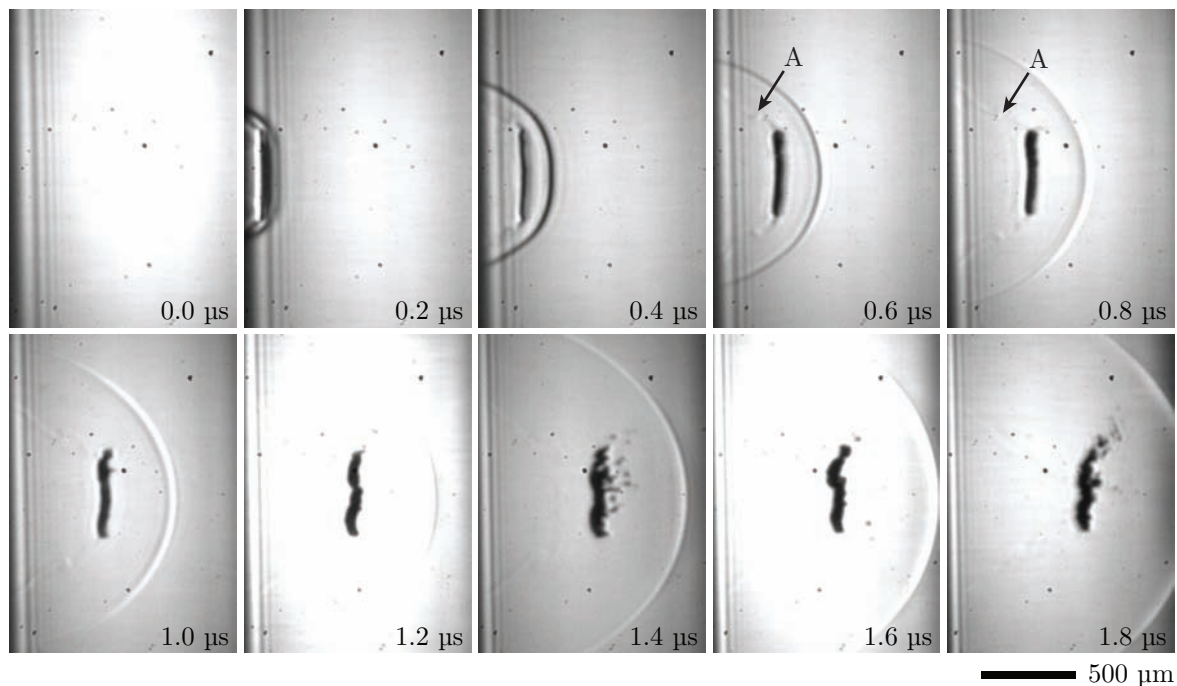
Figure 4.27 Sequence of pictures taken for a 350 nm TP / 80 nm Al sample at 360 mJ/cm^2. The time delays are indicated on the frames. The arrow A shows a gas flow behind the flyer.

towards the periphery. This is surprising because one would expect detached fragments to be slower than the flyer. It is not possible from the shadowgraphy pictures to determine if the fragments come from the center or from the edge of the flyer. The fact that they go forward tends to indicate that they are ejected from the edge, where an eventual gas flow around the flyer would have the most influence. Fragments detaching from the center of the flyer after a certain time delay are hard to conceive because they should be protected from turbulences at this location. Despite of the fragments, the flyer is still in an apparent compact state after about 2 µs.

Although smooth perturbations in the medium density are difficult to visualise with shadowgraphy [90], some air flows can be seen. At 0.8 µs, gas flows are visible between the flyer edges and the substrate (see feature A in Figure 4.27). They can be attributed to a gas front expanding behind the flyer, probably the decomposed TP released at the ablation spot. However, a more sensitive technique such as Schlieren imaging would certainely be useful to understand the origin of that feature [90].

Interestingly, the flyer of aluminum and the flyer of triazene shown in Figure 4.20 follow the same timing of decomposition, i.e. start to fall apart after 1 µs, but exhibit a different aspect. The Al flyer seems much more rigid and brittle while the floppy-like structure of the pure TP flyer leads to the formation of threads. The mechanical properties of the material certainely play an important role in this view.

4.2.1.2   Effect of the laser fluence

The applied fluence affects the energy released into the process and its influence on the flyer ejection was investigated as well. Figure 4.28 presents snapshots taken after 0.8 µs with the same sample as shown above but irradiated at different fluences. The corresponding views of the donor film after ablation are shown below each frame. The intact Al layer appears white on the micrographs due to intense light reflection.
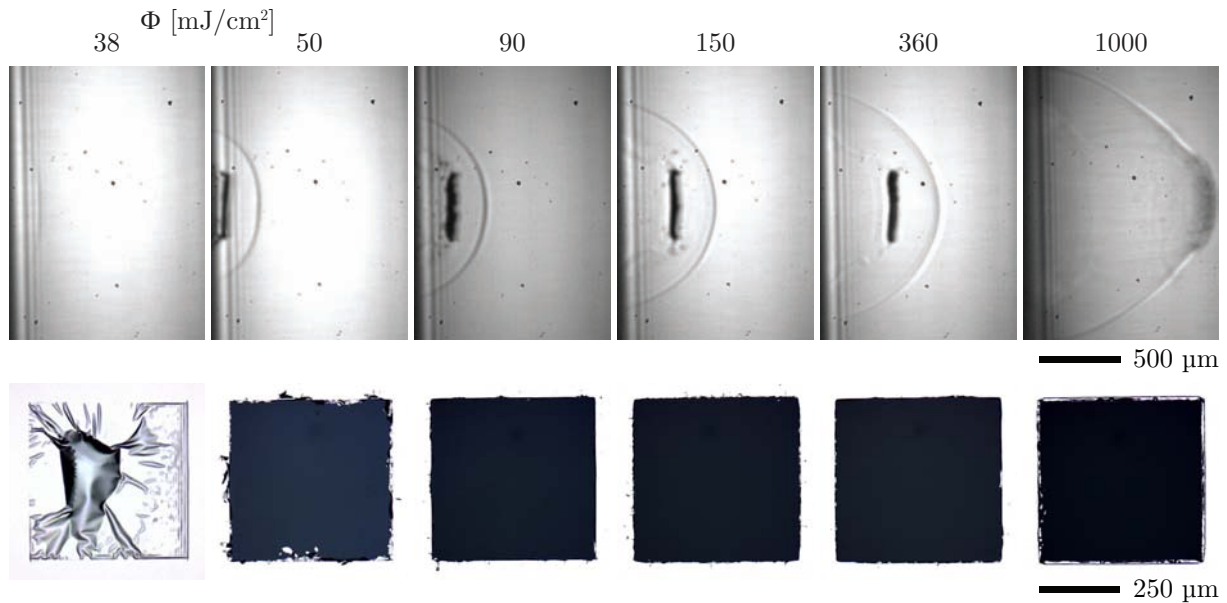

Figure 4.28 Pictures of a 350 nm TP / 80 nm Al sample irradiated at various fluences (top row, increasing from left to right) and the corresponding ablated spots on the donor film (bottom row, different scale). The intact Al layer around the spots appears white.

The shape of the flyer can be correlated with the quality of the ablation spot, as explained below. No material flyer was ejected from the spot at the lowest fluence (38 mJ/cm^2), because the fluence is not sufficient to eject the top layer. The same phenomenon of skin formation described previously accounts for this feature. The "metallic airbag" observed indicates that the presence of an Al layer on the triazene does not influence the shape of the skin formation seen for pure TP layers (see Figure 4.15). Correspondingly, no flyer is present in the shadowgraphy picture, only the shock wave can be distinguished. This feature is interesting, because it proves that the shock wave is also transmitted through a film, i.e. without gas transfer between the location where the pressure jump was created (TP layer) and the propagation medium (air).

When the fluence is increased, delamination occurs. At 50 mJ/cm^2, a flyer is visible and the spot is fully delaminated. The edge of the ablated spots are not very sharp, as if tearing has happened instead of sharp cutting. At the same time, the edges of the flyer seem to be still connected to the donor film on the shadowgraphy picture. This way of detaching is very similiar to what was observed for a single TP layer (see Figure 4.21).

Between 90 and 360 mJ/cm^2, the flyer increases its velocity and its shape becomes also smoother. The aspect of the ablated spots, however, is not really affected, all three have well-defined and sharp edges.

The picture at 1000 mJ/cm^2 is very different, because no flyer is visible, but the shock wave presents a deformation at the front part. The whole sequence is shown in Figure 4.29.
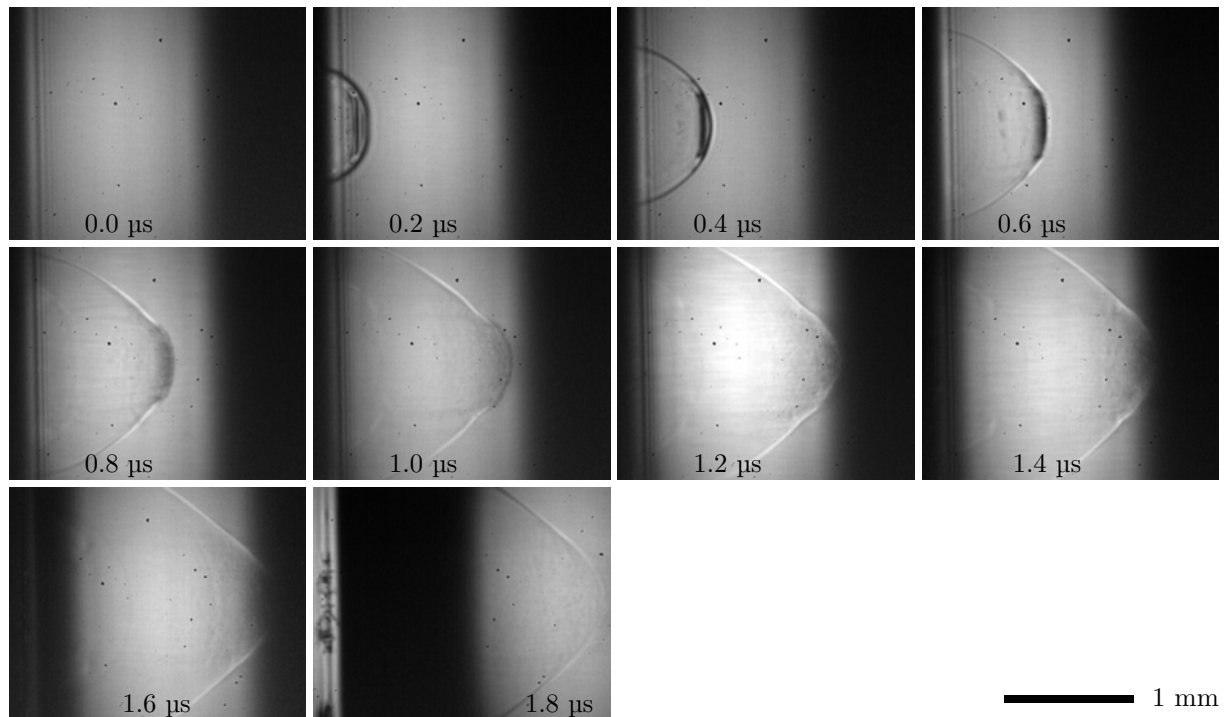

Figure 4.29 Sequence of pictures taken for a 350 nm TP / 80 nm Al sample at 1000 mJ/cm^2. The time delays are indicated on the frames. The illumination has been adjusted on the last frames to follow the shock front.

After 0.2 µs, the shock wave and the flyer are visible, and the flyer has already flown over a large distance, if one compares this with the pictures after 0.8 µs for lower fluences. It is actually difficult to say if the observed flyer is still a solid layer of material or if it is a compact cloud of vaporised material. At 0.4 µs, the flyer reaches the shock wave and is decomposed upon contact. Eventually, a mixed front of debris and compressed air is formed where the flyer meets the shock wave. This mixed front is propagating faster than the shock wave itself and deforms it in the forward direction.

A similar phenomenon of particles overtaking the shock wave was observed before for front side ablation of particle-doped energetic polymers [112]. The shock front was deformed under the effect of particles as well. Obviously, this regime is not appropriate for LIFT because it destroys the flyer. The ablated crater shows correspondingly evidence of unclean edge cutting probably due to the violent ejection. This fluence is therefore the upper limit of the operating window.

The flyers shown in Figure 4.28 are mostly in a good shape. But this situation may change with time and flying distance. The next step is to follow the trajectory of the flyer

and to analyse the distance it can cover while staying intact. A comparison of the flyer after different delay times at various fluences is presented in Figure 4.30. The time delay increases from left to right and the fluence from bottom to top.
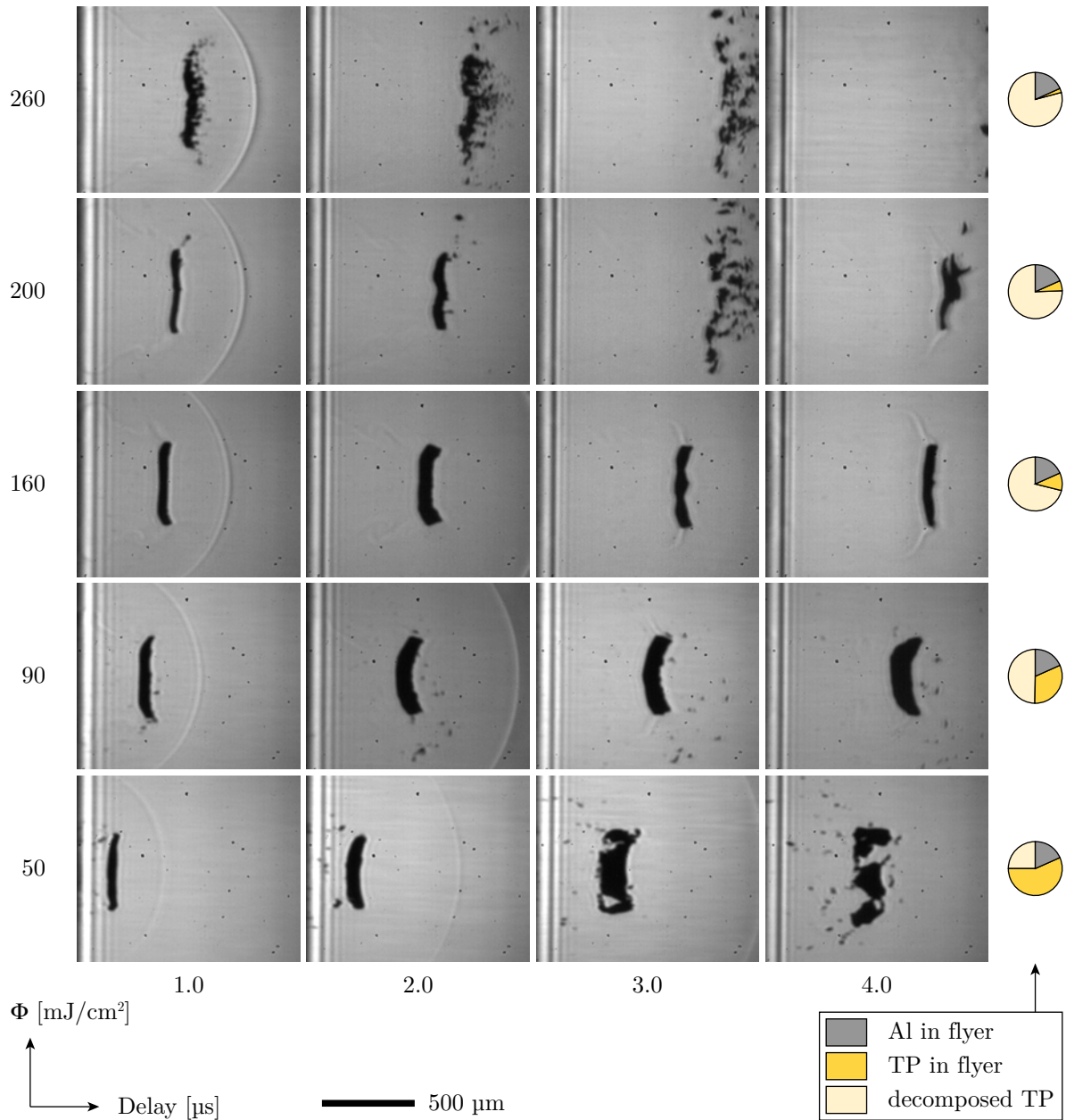
Figure 4.30 Sequences of pictures taken for a 350 nm TP / 80 nm Al sample at different fluences (increase from bottom to top). The pie charts on the right represent the flyer composition (in thickness) estimated from the ablation curves shown in Figure 4.32.

The very early frames (before 1 µs) are not shown but they reveal very similar details at all fluences, i.e. a flat and thin flyer. The "longest-living" flyers are obtained at fluences between 90 and 160 mJ/cm². The flyer at 160 mJ/cm² stays rather flat for the first 4 µs, during which it travelled across almost 1 mm. However, the flyer appears thicker with time, which is due to bending or tilting: as soon as the flyer is not parallel to the viewing

axis anymore, its shadow image appears broader. Indeed, the flyer tends to bend forward during the flight, as can bee seen very well for 90 mJ/cm² (2–4 µs) .

The bending of the edge to the front is counter-intuitive for an object propagating in a medium, because one would expect that the edges are folded backward due to the air drag. In the present case, it is the opposite, which may indicate that there is a gas flow around the flyer to the forward direction. This may originate from an overpressure behind the flyer created by the gas released during the ablation of the triazene layer (see Feature A in Figure 4.27). This overpressure can also explain the detachement of fragments in the forward direction observed at the high fluences.

If an overpressure is build from ablation products, it should equilibrate after a while. This case is actually observed after a longer time, as shows Figure 4.31. The figure shows the end of the sequence at 160 mJ/cm², between 6 and 9 µs.
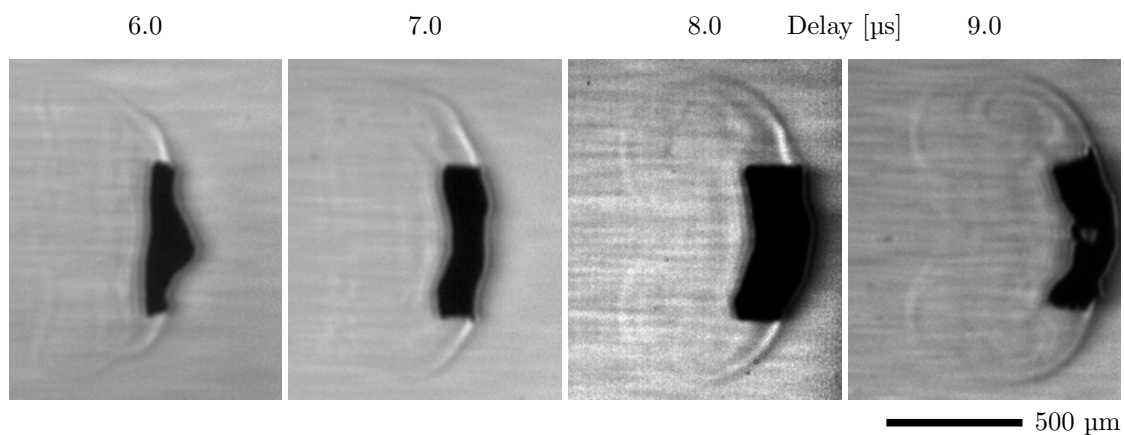
Figure 4.31 Sequence of pictures after long delays for a a 350 nm TP / 80 nm Al sample at 160 mJ/cm². The substrate plane (on the left) was cropped and the pictures were digitally enhanced by background substraction and contrast tuning to reveal the air flows.

The edges of the flyer are bended to the back and are followed by a vortex, increasingly visible with time. The frame at 9 µs shows very clearly the air flows. The pictures then correspond to the classical case of a solid object moving in a medium, with the air drag pulling the edges of the flyer towards the back and creating turbulences behind it. Therefore, it means that the overpressure created behind the flyer during ablation is equilibrated with the ambient after a certain time, and only the normal air drag is dominant.

When the fluence is increased to 200 mJ/cm² and above, the flyer no longer stays intact during the whole observation period and fragments are ejected. The highest fluence (260 mJ/cm²) reveals an early destruction of the flyer (after 1 µs).

The transition between the frames are generally smooth, but the evolution of the flyer may appear strange under certain conditions. For example, the transition between 3 and 4 µs at 200 mJ/cm² seems to be unlogical, because the flyer seems to evolve from

a decomposed to a compact state, but one should keep in mind that every picture was done with a new sample spot. The unavoidable fluence variation from pulse to pulse is most probably visible in this sequence. In this case, the repeatability is low, which is the sign for a fluence close to the threshold of destruction. A low variation in the fluence has therefore a large effect on the flyer state.

Interestingly, the flyer is also falling apart at the lowest fluence, where less stress should be exerted to the materials. In this case, the decomposition pattern is different, because the flyer forms big "clumps" of materials instead of small fragments.

When the fluence increases, two parameters change. More energy is given to the system, and a thicker layer of triazene is ablated. It was shown in the previous section that the non-decomposed part of the triazene is ejected and forms a flyer. Therefore, it is expected that the flyer created from the ablation of a bilayer of Al and TP is also composed of an aluminum/triazene bilayer, whose thickness is depending on the applied fluence. The presence of the triazene polymer in the flyer certainely modifies its mechanical properties compared to a pure metal flyer, and therefore its behaviour during the flight.

In this view, the consideration of the ablated thickness is important for understanding the process. It is not possible to measure the ablation depth in this back side irradiation configuration, but the value can be estimated based on the depth measured with front side ablation, as explained in Section 4.1.4.3. The system is more complex is this case, because an additional layer of Al is present, which may have an effect on thermal diffusion and therefore, on the ablation depth. However, this approximation should serve as a good starting point for the estimation of the remaining thickness. Figure 4.32 shows the ablation depth measured after front side ablation of a 350 nm thick TP film. The sample corresponds to the donor substrate investigated by shadowgraphy except that no Al layer is present. The other curves correspond to thinner films and will be discussed in the next section.
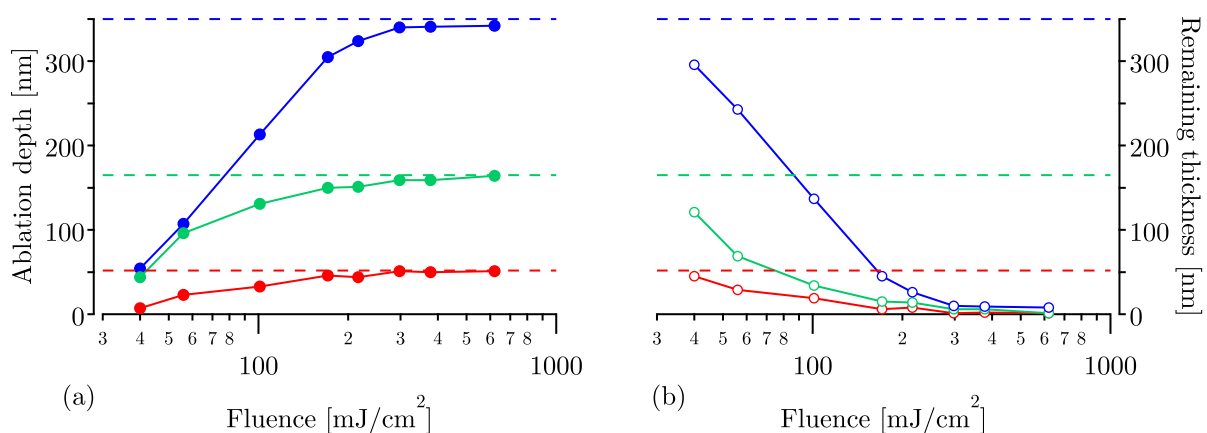

Figure 4.32 (a) Ablation depth and (b) remaining thickness versus fluence for front side ablation of a 350 nm (blue), 150 nm (green) and 50 nm (red) triazene films. The respective film thickness is shown by the dashed lines.

The thickness of the remaining triazene layer, calculated as the film thickness minus the ablated depth, is shown in Figure 4.32 (b) for the three films as well. The ablation curve for a 350 nm thick film shows that the undecomposed thickness is around 70% at 50 mJ/cm^2 and 40% at 90 mJ/cm^2. The undecomposed ratio at a fluence of 160 mJ/cm^2 and above is smaller than 15% and approaches zero when the fluence increases. These values are shown as pie charts next to each sequence on the right part of Figure 4.30.

Apparently, the best flyer is obtained when a substantial triazene thickness is undecomposed. A too thin or too thick remaining layer seems to be not optimal for the flyer. A possible reason may be that the triazene layer reinforces the flyer and allows it to travel intact across a relatively long distance. However, it was shown above that flyers of pure triazene do not stay intact for a long time and start to swell. This suggests that the polymer and the metal layer together may form a composite flyer with improved mechanical properties compared to the metal or the triazene alone.

It is also possible that the Al layer is cracked upon ejection, but is prevented to fall apart because it sticks to the polymer layer, that acts as a "soft" support. This hypothesis is supported by the observation at the highest fluence, where the quasi absence of the triazene layer leads to a fast decomposition of the metal film.

It is surprising that the flyer eventually breaks into parts at the lowest fluence, where a thick layer of triazene should be present. In this case, it is possible that an excessively thick triazene layer is counter-productive. The reasons for this effect are not understood yet, but one should keep in mind that the energy provided to the system is also lower and the sole consideration of the triazene thickness may not be sufficient to explain all the observations.

It is clear from Figure 4.30 that the velocity of the flyer depends on the laser fluence. The position of the flyer versus time is shown in Figure 4.33 (a) (points) together with corresponding fit curves (solid lines) as explained below.

The physical description of the flyer trajectory is not a trivial problem and is still under investigation, but the position can be approximated by a power law of the form

$$x(t) = a \cdot t^b, \tag{4.3}$$

with a and b being the fitting parameters. This equation may not be physically meaningful, but it allows at least to compare the data and to evaluate the curvature of the trajectory through the exponent b. A value of 1 for b is obtained for a constant velocity, while a value above or below 1 indicates an acceleration or a deceleration, respectively. The exponent of the fit, comprised between 0.45 and 0.7, indicates that the flyer slows down with time due to friction in air.

The velocity is given by the derivative of the position fit curve with respect to the time. As the velocity is not constant with time, a reference time of 2 µs was chosen to calculate it. The actual velocity is the value of the derivative taken at the reference time. The reference time is shown graphically in Figure 4.33 (a) (vertical dashed line) and the
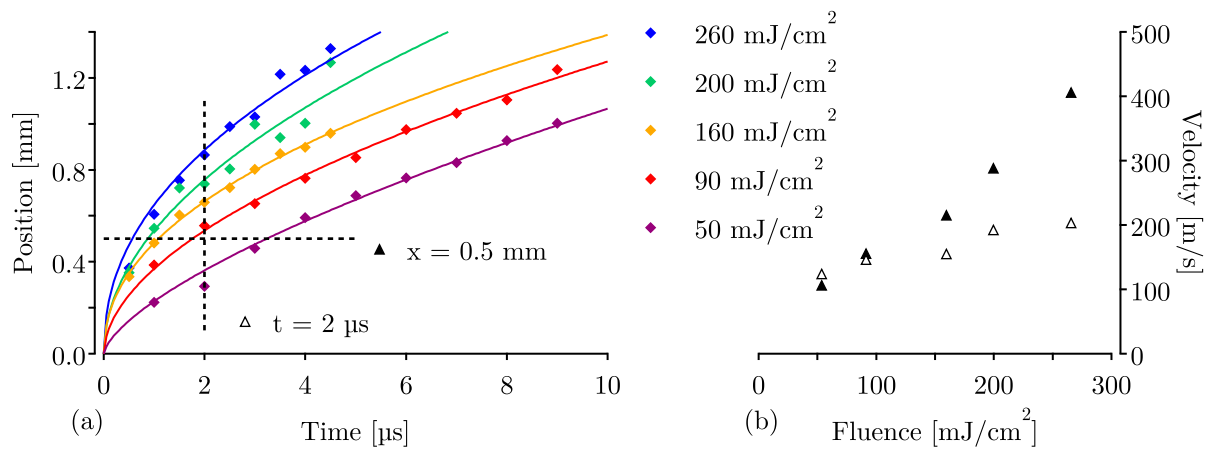
Figure 4.33 (a) Position of the flyer versus time for various fluences (indicated in the graph) obtained from the pictures shown in Figure 4.30 with a 350 nm TP / 80 nm Al sample. The points are the measured data and the solid lines are fits from Equation 4.3. The dashed lines show the reference position or time used to calculate the velocity, shown in part (b). The filled ▲ are velocities at a constant distance ($x = 0.5$ mm) while the empty △ show the velocities at a constant time ($t = 0.2$ μs).

results are shown in Figure 4.33 (b), (△). Flyer velocities in the range of 100 to 200 m/s are obtained. The velocity increases with the laser fluence, as expected.

In the LIFT process, the adjustable parameter is not the time but the distance between the donor and the receiver substrate. For this reason, the velocity at a given position is a valuable information, which is shown in Figure 4.33 (b) as well (▲). Similar to the reference time line, the reference position is shown graphically in Figure 4.33 (a) (horizontal dashed line). The velocities obtained with this calculation range from 100 to 400 m/s, which is different from the value obtained at a fixed time. It shows that the choice of the reference point is crucial if one wants to compare values.

The use of an arbitrary function is of limited interest and only useful for comparison purposes. At this point, it would be very useful to have a model describing the flight and providing a parameter, for instance the initial velocity, to compare different flyers.

Nevertheless, the order of magnitude of the flyer velocity is in the hundreds of meter per second, close and sometimes even above the speed of sound.

4.2.1.3   Effect of the triazene layer thickness

It seems that the triazene thickness plays also a role in the state of the flyer. Therefore, experiments were performed with samples of different triazene thicknesses while keeping the Al layer unchanged in order to understand the system in more detail. Samples made of 50 nm TP / 80 nm Al and 150 nm TP / 80 nm Al were compared to the 350 nm TP / 80 nm Al sample used before. An overview of the comparison is shown in Figure 4.34, where all pictures are taken after the same time delay of 2 μs. The fluence increases from

left to right and the film thickness from bottom to top. The pictures on the top row correspond to Figure 4.30.
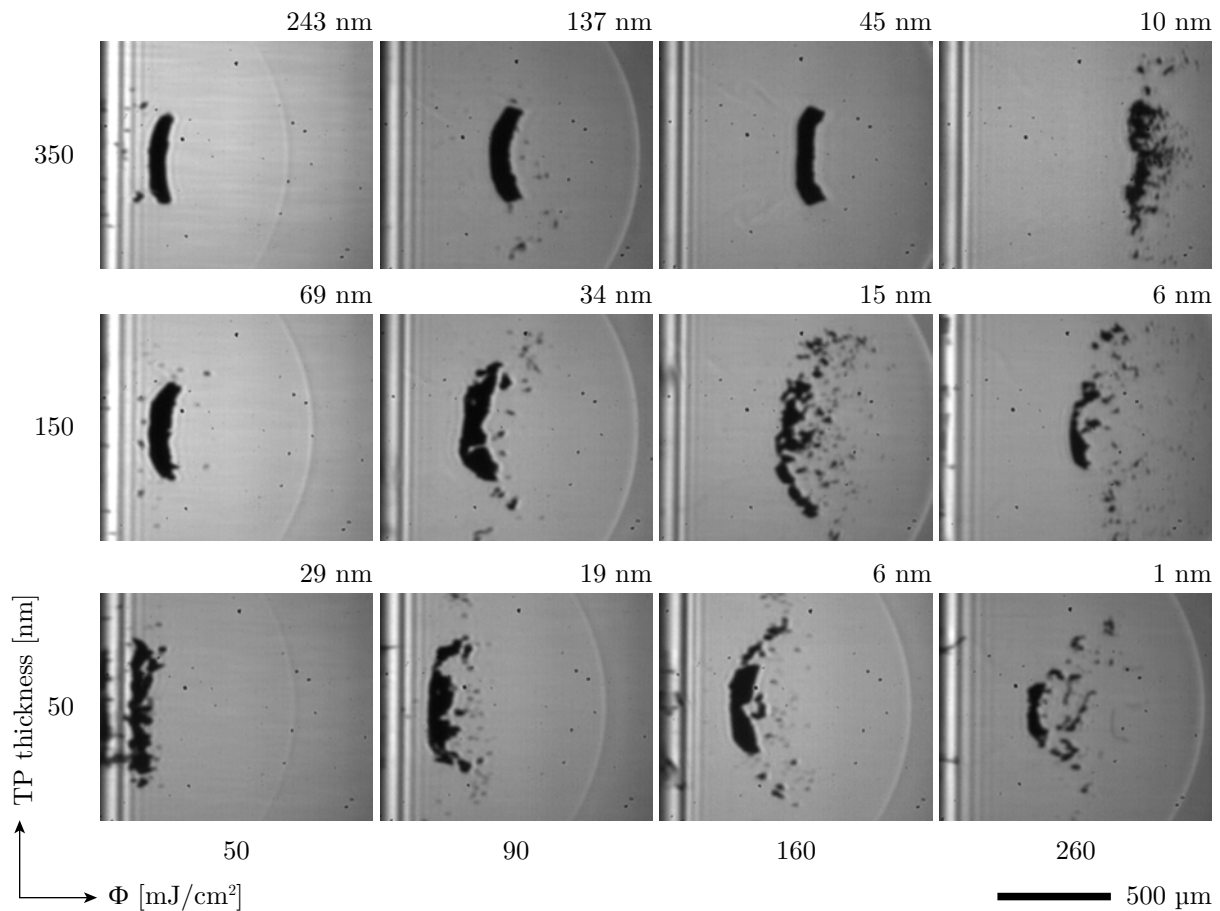
Figure 4.34 Pictures taken after 2 µs at different fluences (increasing from left to right) with samples made of TP (various thicknesses, increasing from bottom to top) and 80 nm Al. The number above each frame is the estimated remaining thickness of triazene in the flyer (from Figure 4.32).

The destruction of the flyer occurs at a lower fluence when the triazene thickness decreases. With a 150 nm thick TP layer, the flyer shows signs of destabilisation at 90 mJ/cm² and is completely destroyed for higher fluences. This effect is even more pronounced with a 50 nm thick triazene layer, where no stable flyer is obtained at all after 2 µs.

These observations can be interpreted with the same analysis involving the remaining triazene thickness, shown above each frame of Figure 4.34. At a given fluence, the thickness of the undecomposed layer depends on the initial triazene film thickness, which is particularly important at the low fluences. Indeed, at 50 mJ/cm² the undecomposed thickness of TP is very different depending on the sample thickness, corresponding to the largest differences in flyer quality. It was suggested above that the ejection of a stable aluminum flyer requires a certain amount of triazene to reinforce it. With thinner fims,

this amount is reached at a lower fluence, and for the 50 nm film, even the starting amount of polymer is not sufficient to provide this supporting function to the flyer.

One goal of the LIFT technique was to achieve multi-layer patterning, i.e. to deposit single layers of material successively. Such a processing requires to completely decompose the sacrificial layer of triazene and avoid its presence on the transferred pixels, in order to prevent any contamination between the layers. More importantly, a good electrical contact can only be established if no remaining TP stays on the transferred material. Now, it seems that a good metal flyer needs to contain a significant layer of TP to fly in a good state. These two contradictory facts may represent a major problem for the application of LIFT for multi-layer deposition.

It appears from the pictures of Figure 4.30 that the front of the shock wave is at different positions depending on the sample thickness. A direct comparison of the shock wave propagation is not appropriate because the ablated depth of triazene is different, which has an impact on the shock wave energy. However, it is possible to compare the samples using the shock wave model shown in Section 3.2 (Equation 3.33). The parameters used are taken from Table 4.3 and the ablated depth from front side measurements (Figure 4.32). The results of the calculation are shown in Figure 4.35, where the shock wave energy is normalised by the total input energy.
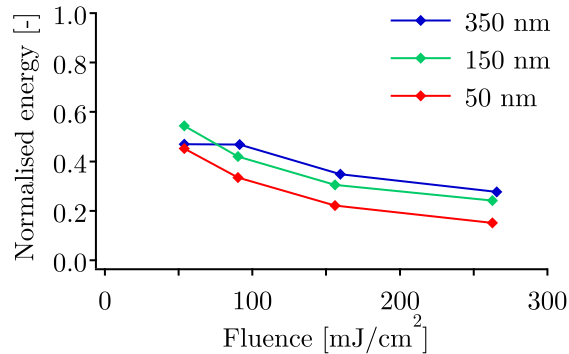
Figure 4.35 Normalised energies of the shock waves for the samples shown in Figure 4.34. The samples are made of TP (thickness shown in the graph) and 80 nm Al.

The values range from 20 to 55%, which is comparable to what was obverved for pure TP (see Figure 4.25). The normalised shock wave energy decreases with increasing fluence for all three samples, except that the curve for 350 nm TP exhibits a maximum at 90 mJ/cm^2, which is again comparable to the pure TP sample. The two thinner samples do not reach a maximum in the investigated range.

It is noteworthy that the thickness of the triazene layer influences the normalised energy value, which increases with increasing film thickness at a given fluence (excepted for the point at 50 mJ/cm^2). There is no reason justifying this fact *a priori*, but it may be that the ratio between the Al and the TP layer, which is different between the samples,

plays a role in the transmission of the shock wave. It was shown in Section 4.1.5.2 that the flyer has a large influence on the shock wave at the low fluences, where the flyer is relatively thick. In this case, differences between the samples are observed at the high fluences as well, but one should keep in mind that an Al flyer is always present.

The second reason for this difference may be the penetration depth of the laser beam, which is larger than the TP thickness for the 50 nm sample. A complete absorption of the laser pulse in the polymer layer is used in the mathematical model, which is probably wrong for thin samples.

4.2.1.4 Effect of the laser pulse duration

Material ejection was investigated with the picosecond 355 nm laser as well for two reasons. The shorter pulse duration has an influence on the heat diffusion, as shown above, and less thermal losses can be expected. LIFT proceeds from ablation in a confined system, where the pulse duration could also have an influence. The other motivation is to study the effect of a beam with a gaussian energy profile on the flyer ejection and shape.

A sample of 350 nm TP / 80 nm Al was investigated with the two different lasers (ns 308 nm and ps 355 nm) under the same conditions. A typical sequence of pictures is shown in Figure 4.36.
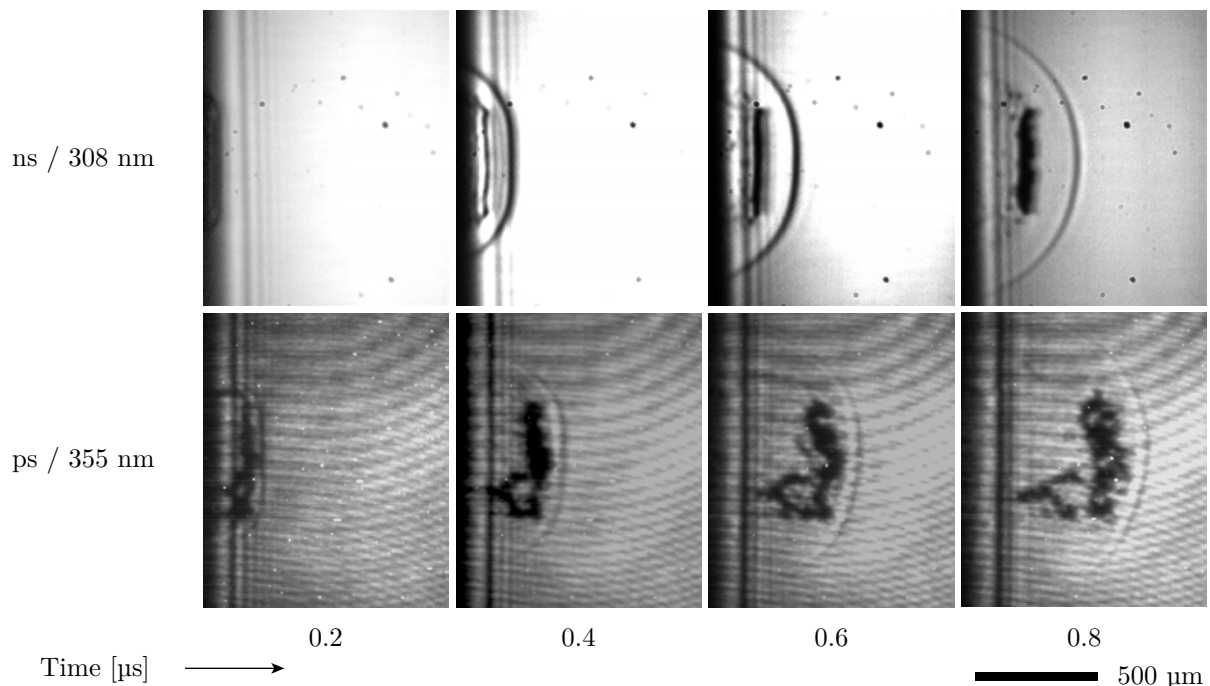

Figure 4.36 Sequence of pictures taken with a 350 nm TP / 80 nm Al sample at 90 mJ/cm^2 with two different lasers, the nanosecond 308 nm (top) and the picosecond 355 nm (bottom).

The difference in image quality originates from the different type of illumination, where a dye illumination (top row) results in a homogeneous background free from interferences

fringes. It is striking that the propagation of the shock wave and the flyer is about twice as fast with the picosecond irradiation. The amount of ablated material must be considered for a proper comparison. Figure 4.13 shows a comparison of the ablation depth of a slightly thicker film for the two lasers. It is clear that the amount of ablated material is lower for the picosecond laser at this fluence.

The origin of this behaviour is not completely elucidated yet and modelling of the system is currently in progress to understand this large difference. Nevertheless, the shorter pulse duration creates a much stronger shock wave and propells the flyer faster, probably because the rate of pressure increase is much higher upon picosecond ablation, which can create a faster ejection of material.

Heat diffusion is reduced upon picosecond ablation, which should also have an influence on the energy balance of the system. Less heat losses should occur, therefore more energy could be available for the mechanical work (shock wave and flyer ejection).

The second major difference between the two lasers is the shape of the flyer. The flyer ejected by picosecond irradiation has an inhomogeneous and expanded shape compared to the nanosecond-generated flyer. It is almost instantaneously destroyed upon ejection, as seen after 0.2–0.4 µs. The material ejected at the bottom of the flyer, which is slower than the main part, consistenly appears on all frames, showing that it is reproducible. This suggest that inhomogeneous ejection is not random but certainely due to the inhomogeneous beam profile of the laser (see Figure 4.8), which inhibits clean delamination of the triazene film upon back side ablation, as shown in Figure 4.18. Microscopy pictures of craters ablated at a lower fluence (40 mJ/cm^2, not shown) reveal a partial ablation in the bottom part of the spot, where the slow propagating material is observed on the shadowgraphs. Consistently, no flat and compact flyer was obtained with picosecond irradiation in the investigated fluence range (30–360 mJ/cm^2).

4.2.1.5   Effect of background pressure

The background gas has an influence on the flyer trajectory, since the flyer decelerates after a certain time. The shape of the flyer is affected as well, to due the air drag. In vacuum it should be different, because there is no resistance from the air.

The influence of the background pressure was studied by material ejection at a pressure less than 10^{-1} mbar (typically 5–8·10^{-2} mbar). A comparison between vacuum and atmospheric pressure is shown in Figure 4.37, where a sample of 350 nm TP / 80 nm Al was ablated at a fluence of 160 mJ/cm^2.

As expected, no shock wave is visible in vacuum. There is still a pressure jump at the ablation spot, but no medium for the propagation of the shock. The flyer evolves faster in vacuum than in air, which was expected as well. The shape of the flyer is interesting, because it does not stay completely flat as one may have expected. It appears thicker than in air, meaning that it is either folded or tilted. The pictures show that it is actually folded, similar to the case in air, but with the difference that the curvature is in the
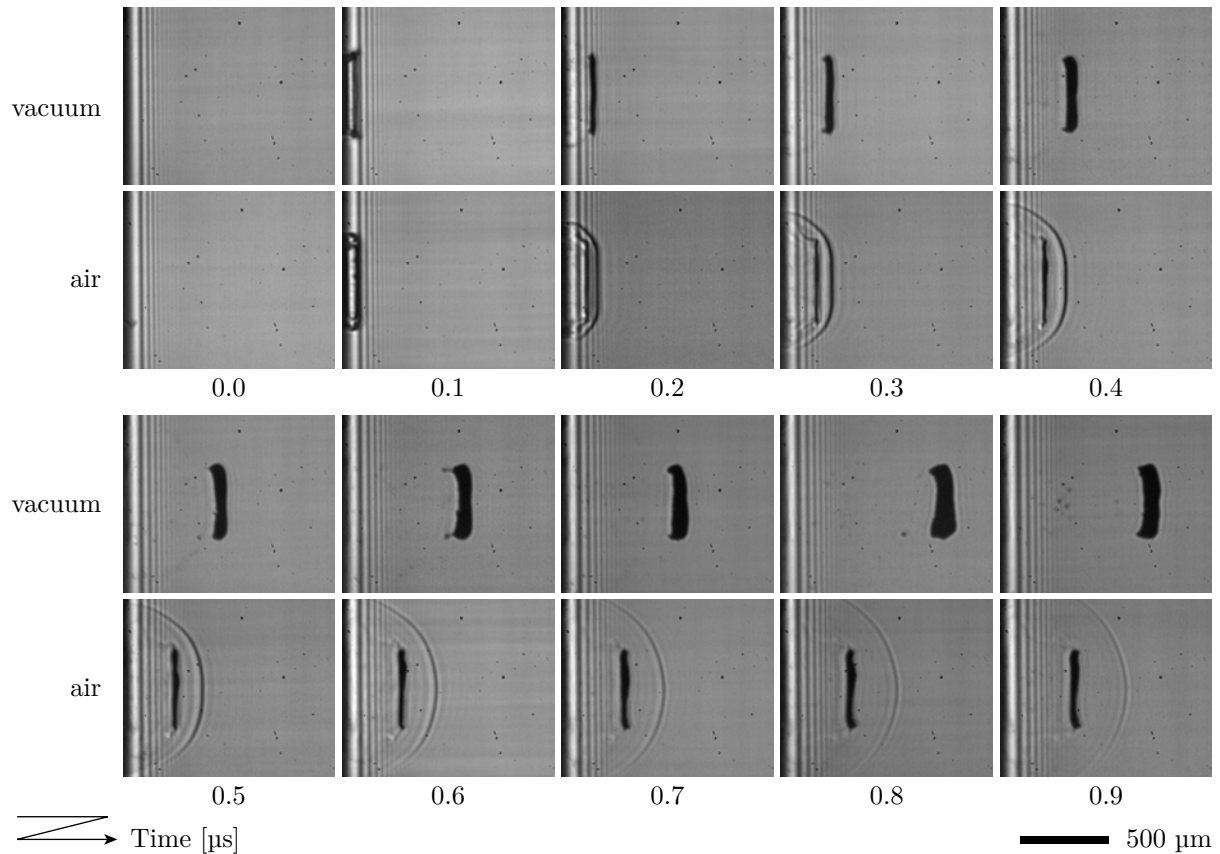
Figure 4.37 Sequence of pictures taken with a 350 nm TP / 80 nm Al sample at 160 mJ/cm^2 under vacuum and atmospheric pressure.

opposite direction. The edges of the flyer are bended backward in vacuum, while in air they are headed forward at early stages ($t < 1$ µs).

This fact is clearly visible when fragments are detaching from the flyer, as it it the case in Figure 4.38, taken with the same sample at a higher fluence (280 mJ/cm^2).

In air, fragments detaching from the flyer are faster than the flyer itself, whereas the flyer is faster than the fragments in vacuum. A possible explanation is that in air, the flyer offers a large surface to air resistance. The central part of the flyer is slowed, but the fragments, offering less resistance to air, are less decelerated and maintain a higher velocity than the central part. In vacuum, the central part of the flyer is not slowed down. It appears then that all parts of the flyer, including fragments, should propagate at the same speed. However it is not the case and fragments are slower than the main part.

The position of the flyer versus time is shown in Figure 4.39 (a) (♦) to analyse this behaviour in more detail. The same power law as for the travel in air (Equation 4.3) was used to fit the positions versus time. The fit curves are shown as lines in Figure 4.39 (a).

In this case, the exponent b is between 1.03 and 1.16, i.e. the velocity of the flyer slightly increases with time. As remainder, the exponents calculated in air range from 0.45 to 0.7.

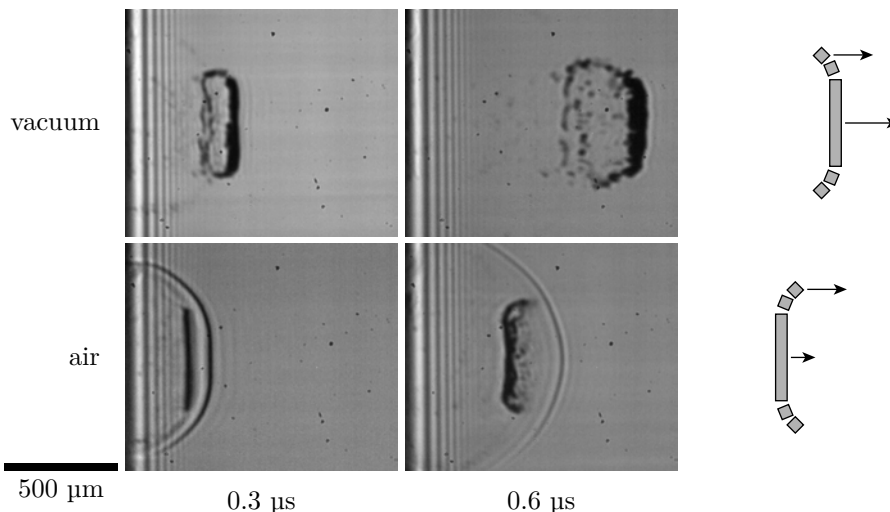The flyer can reach very high velocities, i.e. above 2 km/s. In air, the flyer cannot

Figure 4.38 Sequence of pictures taken with a 350 nm TP / 80 nm Al sample at 280 mJ/cm^2 under vacuum and atmospheric pressure. The scheme on the right shows the relative movement of the flyer and fragments from the egde under both pressure conditions.

reach this velocity, because it attains the shock wave where the flyer is destroyed.

The visible part of the flyer accelerates in vacuum, which is very surprising, because no energy is supplied to the flyer after the ablation pulse. It was shown previously that ablation occured only during the laser pulse and stopped afterwards [43]. In vacuum, no forces can act on the flyer as soon as it is detached from the donor film. A hypothetical explanation to an increase in speed is that the flyer looses a part of its mass, which is ejected at the rear side at a lower speed. The conservation of momentum requires then that the main part of the flyer accelerates.

The fragments detaching behind the flyer at 280 mJ/cm^2 (Figure 4.38) may confirm this hypothesis. At lower fluences, no opaque debris is revealed by shadowgraphy, but it might be possible that products invisible for our observation method are released at the rear of the flyer. The reason why no mass release should occur from the front side of the flyer may be the asymmetry in the composition (TP behind and Al in front) and the temperature (a hotter temperature may be expected on the rear side, which is closer to the ablation spot).

4.2.2   Ejection of a bilayer system

The system of TP and Al was chosen as a model system for studying the transfer and to gain knowledge about the flyer ejection. However, the goal of the work is to transfer pixels for OLED displays and particulary the electroactive layer. For this purpose, the well-known MEH-PPV was selected as electroluminescent material. At this stage, it was not possible to coat MEH-PPV directly onto the triazene layer due to a solvent compatiblity issue. The problem was overcome by preparing samples of TP/Al/MEH-PPV on fused
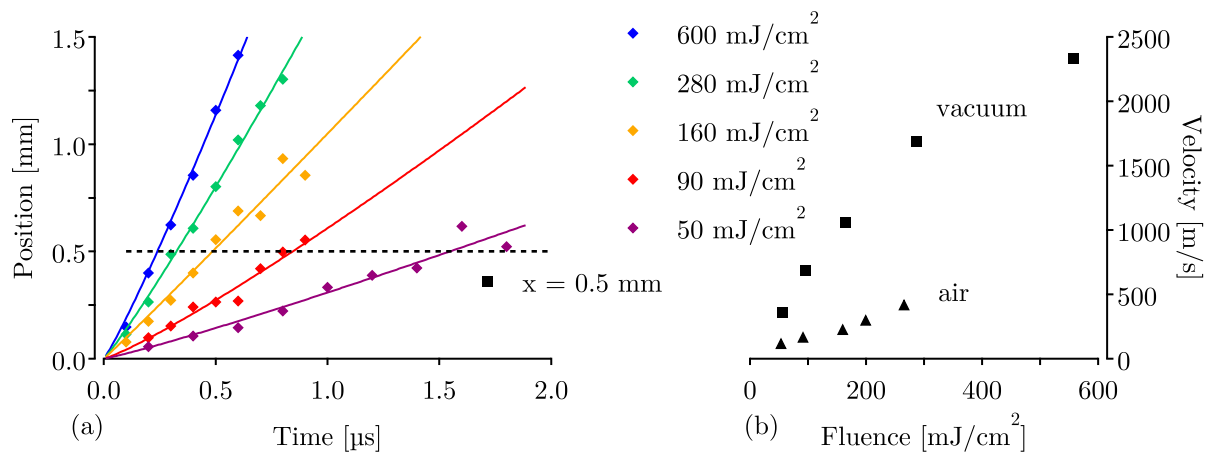
Figure 4.39 (a) Position of the flyer versus time for various fluences (indicated in the graph) measured in vacuum with a 350 nm TP / 80 nm Al sample. The points are the measured data and the solid lines are fits from Equation 4.3. The dashed line show the reference position used to calculate the velocity, shown in part (b). The velocity in vaccum at a constant distance ($x = 0.5$ mm) is shown by the ■. As comparison, the velocity in air is indicated by the ▲ symbols (from Figure 4.33).

silica, which will serve as donor substrates. The material ejection from this system was studied under the same conditions used before to compare the effect of the third layer.

4.2.2.1   Effect of the additional layer

Figure 4.40 shows a comparison of the the flyer ejection from a 350 nm TP / 80 nm Al / $\sim$ 50 nm MEH-PPV film (top) and a 350 nm TP / 80 nm Al film (bottom) at a fluence of 270 mJ/cm^2.

Figure 4.40 Sequence of pictures taken at 270 mJ/cm^2 for two samples with the same layer of 350 nm TP / 80 nm Al. The sample in the top row was additionally coated with $\sim$ 50 nm MEH-PPV.

The shock wave and the flyer propagate at the same velocity for both samples. A

difference appears only after 0.8 µs. The bilayer flyer of Al/MEH-PPV does not exhibit signs of destabilisation while the Al flyer starts to fall apart. Instead, it remains in a good shape until at least 1 µs.

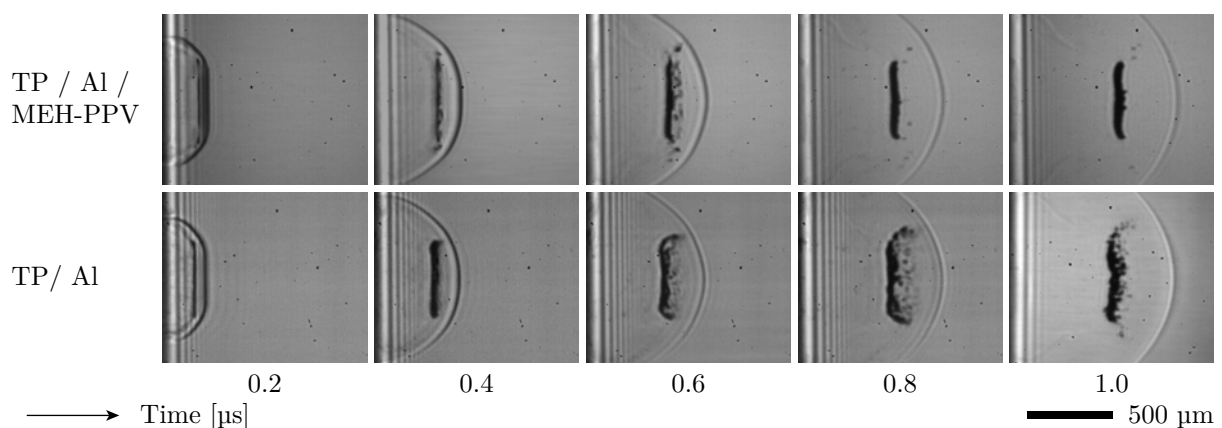The effect of the MEH-PPV layer is similar to the influence of the undecomposed layer of triazene, i.e. it provides mechanical stability to the metal flyer. It was shown previously that at a fluence of 270 mJ/cm^2, only a very thin layer of triazene should be present on the flyer, which is the reason why the TP/Al flyer starts to decompose. Differently, the flyer containing MEH-PPV is not decomposed because the reinforcing role is played by the MEH-PPV, which is on the front side of the metal where it is protected from the laser irradiation and heating.

A comparison was performed at lower fluences as well. Figure 4.41 shows the same samples as above at different fluences. The time delay chosen is not exactly the same for both samples (1.8 and 2.0 µs), nevertheless it allows a qualitative comparison.
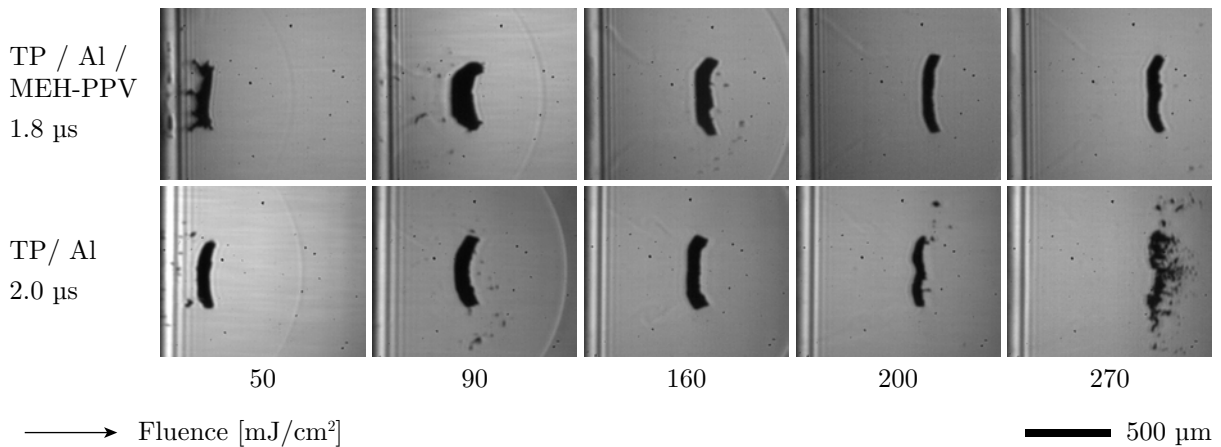
Figure 4.41 Pictures taken at different fluences (increasing from left to right) for two samples with the same layer of 350 nm TP / 80 nm Al. The sample in the top row was additionally coated with ∼ 50 nm MEH-PPV. The time delay is 1.8 µs for the MEH-PPV-coated sample and 2.0 µs for the TP/Al.

The two samples show very similar behaviours at the intermediate fluences, i.e. a rather flat shape and a low amount of debris ejection. At these fluences, the remaining part of triazene adds to the bilayer flyer and the metal layer is sandwiched between two polymer layers. This configuration is probably even more stable against fragmentation. At 90 and even more at 50 mJ/cm^2, large differences appear. At 50 mJ/cm^2, the flyer with MEH-PPV is delaminated in the same way as the pure TP flyer close to the threshold, i.e. with the creation of "threads" from the ablation spot (see Figure 4.21). This behaviour is a sign that the threshold fluence for the complete delamination is very close. Indeed, it is expected that this threshold is higher compared to the TP/Al film, due to the presence of an additional MEH-PPV layer, because there is more mechanical strength to overcome.

In general the ejection of bilayer flyers from Al/MEH-PPV films shows a very clean

behaviour, indicating that the transfer of bilayer systems should not be an additional difficulty compared to pure Al.

4.2.2.2 Effect of the triazene layer thickness

The influence of the triazene film thickness on the bilayer ejection was studied as well. A particularly interesting observation was made at the highest fluence (400 mJ/cm^2), shown is Figure 4.42.
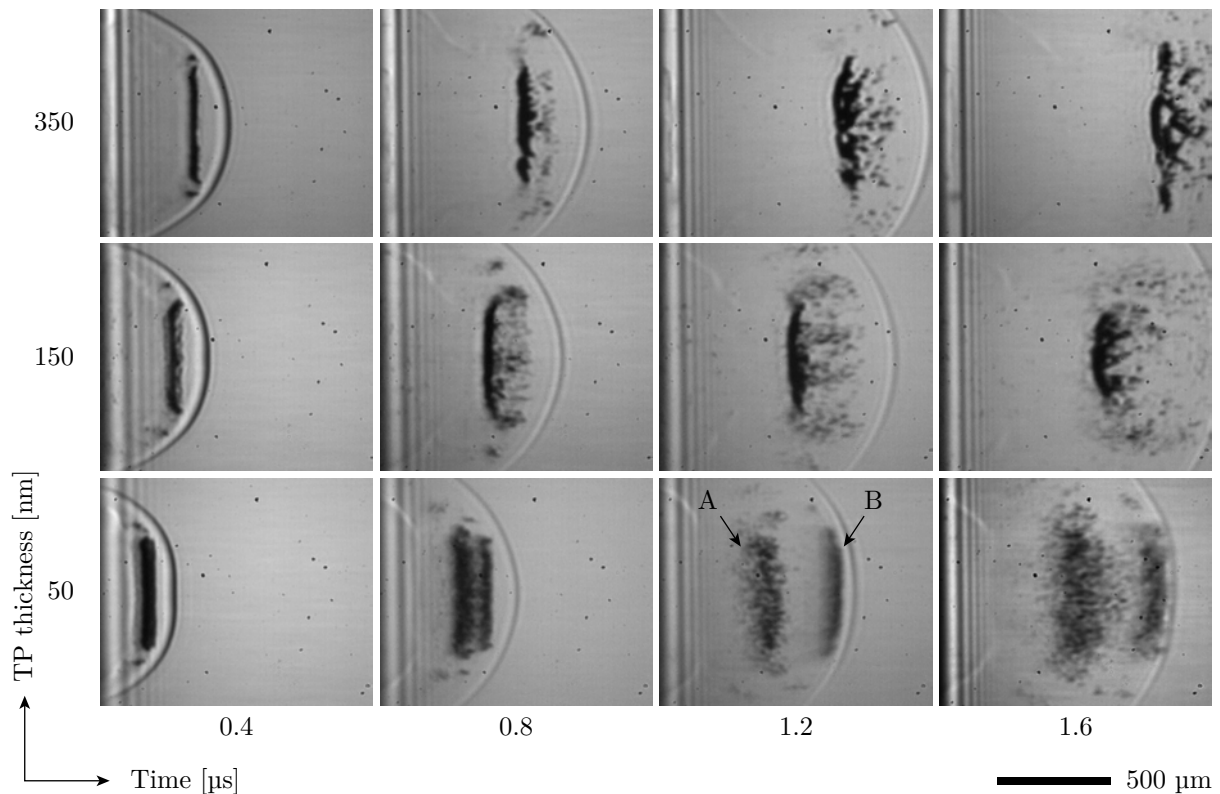
Figure 4.42 Sequences of pictures taken at a fluence of 400 mJ/cm^2 with samples made of TP (various thicknesses, increasing from bottom to top) / 80 nm Al / ~ 50 nm MEH-PPV.

At this fluence the flyer is destabilised and starts to fragment at all TP thicknesses, but the way the thinner TP samples fragment is very surprising. The creation of two material fronts (shown as A and B in Figure 4.42) can be observed, which propagate at two different velocities. The flyer is apparently separated in two upon ejection. This feature was not observed with single Al layers, suggesting that the front B may be attributed to the separation of the MEH-PPV layer from the metal (indicated by arrow A in Figure 4.42). This effect happens only at high fluences and with thin TP layers, i.e. in a situation where the Al layer may absorb a large part of the laser pulse energy. It is possible that the metal layer is sufficiently heated to transfer heat to the MEH-PPV layer, which may in turn be decomposed and readily ejected forward. This effect was not further investigated, but might be used for giving an indication about the temperature of the metal layer.

4.3   Material transfer across a gap

The next step on the way towards pixel depostion is to investigate how the created flyer can be collected onto a receiver substrate. A glass substrate was used as receiver in all the transfer experiments. Two separation distances of 1 and 0.5 mm between the donor and the receiver substrates were investigated by time-resolved shadowgraphy, because these relatively large gaps allow to use lateral imaging to study the effect of the receiver substrate on the flight of the flyer and to follow its deposition. Transfer upon a smaller gap (20 µm) was tested as well, but no lateral imaging was possible.

4.3.1   Transfer of a metal layer

The transfer of the model system made of TP and Al is shown first. As a starting point, the conditions yielding the best flyer upon free ejection in air have been applied.

4.3.1.1   Effect of a receiver substrate

Figure 4.43 (a) shows a sequence of shadowgraphs taken in the presence of a glass receiver substrate placed 1 mm apart from the donor substrate. The sample was a 350 nm TP / 80 nm Al film which was irradiated with a fluence of 160 mJ/cm^2. The donor substrate is on the left side while the receiver is located on the right side. The pictures were cropped laterally to the size of the gap.

The flyer is ejected and propagates in a similar way as for the case without receiver. Within the investigated time, the arrival of the flyer on the receiver plate is not visible. The unsharp shapes visible for times > 0.8 µs on each succesive frame is not the moving flyer, but can be assigned to the final state of all previous flyers. The presence of this object on the picture is explained by Figure 4.43 (b). Each frame is a new spot on the sample, obtained by scanning the sample horizontally with the motorized stage. The viewing axis of the camera is horizontal as well and coincides with the translation axis. For this reason, any ejected material that did not land in a flat way on the receiver substrate is visible in the following pictures. Therefore, each frame shows the current flyer in movement but also the final state of all previous flyers, which appear slightly unsharp because they are out of focus. This explanation is confimed by pictures taken several seconds after the pump pulse, where the deposited flyers are still visible.

Though not wanted, this effect shows clearly that the transfer under these conditions yields a poor depositon because the transferred patterns are not deposited flat on the receiver substrate. The reasons for this may be that the flyer would require more speed to stick properly onto the receiver, or the opposite, that the flyer had too much energy and partially bounced back. It is possible as well that the flyer was not flat enough at the arrival, which prevented a good deposition. The shape of the flyer at 1.6 and 1.8 µs seems to support the last hypothesis.
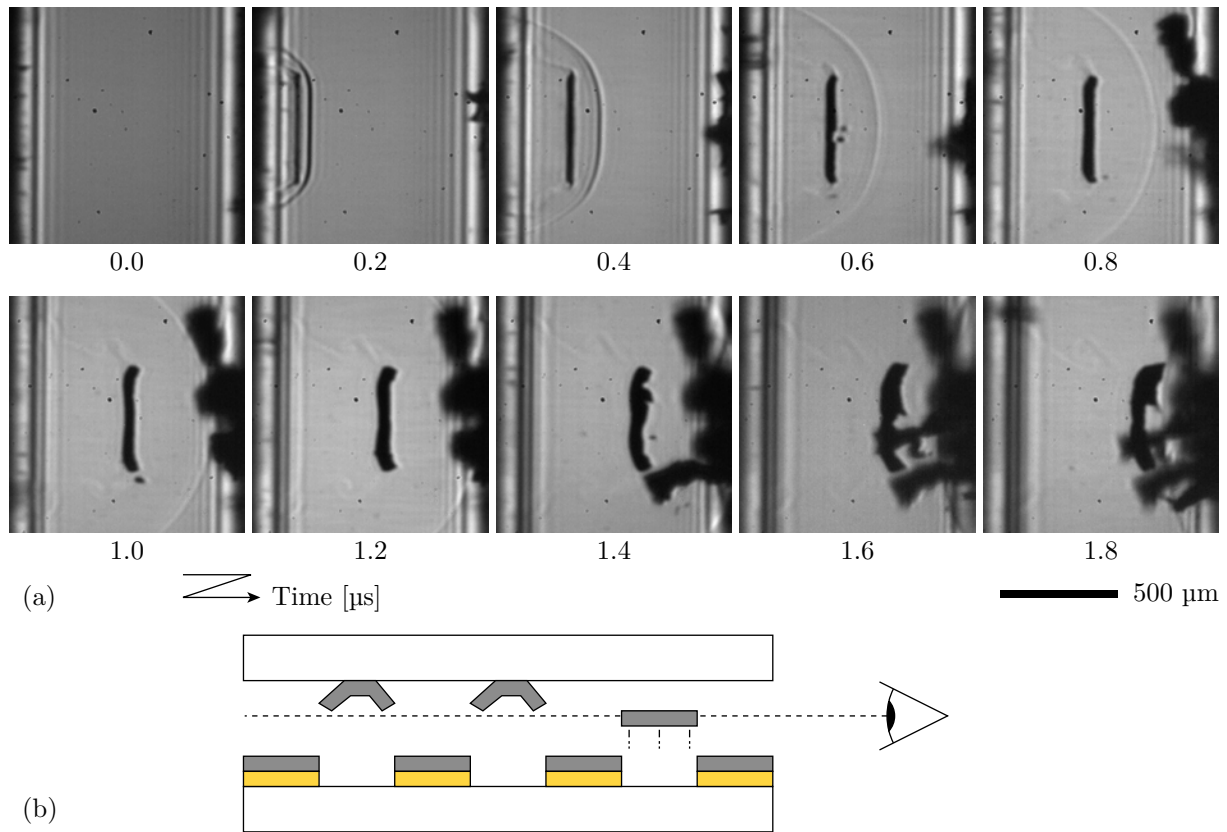
Figure 4.43 (a) Sequence of pictures taken with a 350 nm TP / 80 nm Al sample at 160 mJ/cm² with a receiver substrate at a distance of 1 mm. (b) Scheme explaining the presence of the unsharp objects seen close to the receiver substrate.

An observation of the initial stage or arrival position is very difficult and was not achieved, even when no residual flyer blocks the line of sight, probably due to the tunnel-like geometry of the setup (as shown in Figure 4.43 b) with 1 mm width for 25 mm depth.

4.3.1.2   Effect of the fluence

The effect of the laser fluence on the transfer is shown in Figure 4.44. Pictures of the same sample (350 nm TP / 80 nm Al) were taken at different fluences and time delays. Depending on the fluence, each flyer has a different velocity and the delays were chosen to match the positions at the different fluences. The left column shows the flyers close to the receiver, the second column from left represents the flyers arriving on the receiver and the third column was taken at the end of the sequence. No pictures after 1.8 µs were available for a fluence of 160 mJ/cm², because of the masking effect discussed above. The column on the right shows microscopy pictures of the receiver substrate after transfer (at a different scale).

From the shadowgraphs and the pictures of the receiver after transfer, the fluences can be separated into two domains. In the low fluence regime (50 to 160 mJ/cm²), the flyer
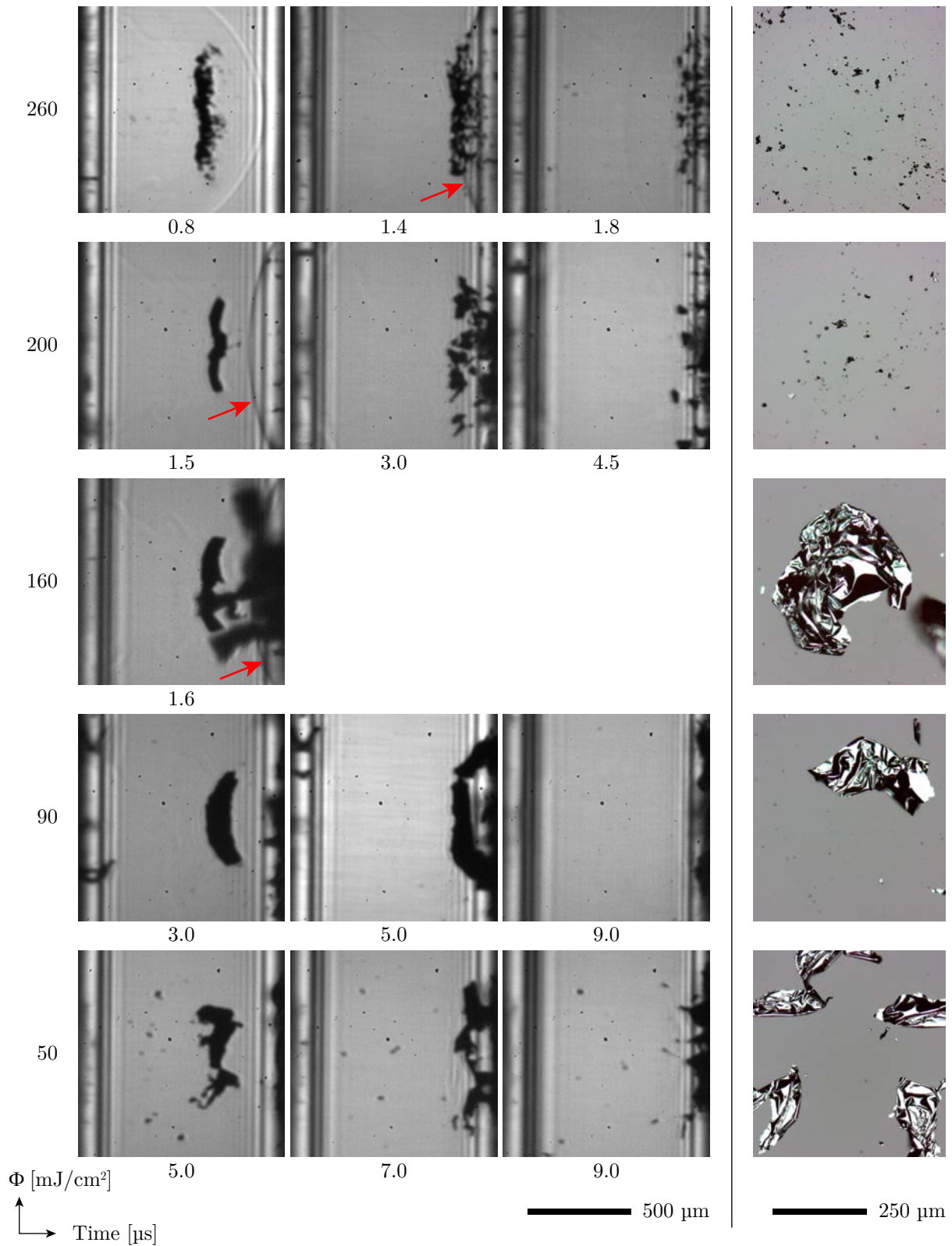
Figure 4.44 Sequence of pictures taken at several fluences (increasing from bottom to top) with a donor sample of 350 nm TP / 80 nm Al and a receiver substrate at a distance of 1 mm. The time delays, increasing from left to right and different at each fluence, were selected to show the flyer at similar positions.The right column shows optical microsopies of the receiver substrate after transfer at the corresponding fluences (different scale). The red arrows show the reflected shock wave.

reached the receiver in one or few big parts, and large metal pieces are identified on the deposition spots. This low fluence range appears to be more appropriate for depositing intact flyers of material, although no satisfactory transfer was achived here. The best result is obtained at 160 mJ/cm^2, where a large metal flyer is detected on the receiver. However, the aspect of the flyer is far from the original square pattern ejected from the donor film, as the flyer is folded, resulting in a smaller size, as shown in Figure 4.43.

When the fluence is decreased, much fewer residues of previous flyers are observed on the shadowgraphs, but only small pieces of the metal are deposited. The frames before arrival show that the flyer did not reach the receiver plate as a compact film, according to the images shown in Figure 4.30 taken without receiver. The way the flyer is split into parts on the shadowgraphs at 50 mJ/cm^2 clearly coincides with the spread pattern found on the receiver.

In the high fluence range (200 and 260 mJ/cm^2), the flyer is broken into small fragments before arrival and correspondingly, only particles are found on the receiver substrate. This is particulary visible at 260 mJ/cm^2, where the flyer falls apart at 0.8 µs already.

The laser fluence determines the velocity of the flyer but also the thickness of the undecomposed triazene layer. Therefore, depending on the fluence, the thickness of the flyer is different, which has an impact on the stability, as shown in Section 4.2.1.2. This suggests that the difference in the deposited flyer quality between the various fluences may be due to the different remaining TP layers as well.

Another interesting feature is visible at these fluences. The shock wave created at the ablation spot is reflected back on the receiver plate and travels backward. This reflection is partially visible at 160 mJ/cm^2 after 1.6 µs but appears clearly after 1.5 and 1.4 µs at 200 mJ/cm^2 and 260 mJ/cm^2, respectively (indicated by the red arrows in Figure 4.44). In this latter case, the shock wave meets the fragmented flyer and passes through it. It is not clear from these pictures whether the flyer is decomposed due to the distance, comparable to the case when no receiver is present, or whether the shock wave contributes to its destruction. To investigate this effect, a comparison of shadowgraphs taken at 200 mJ/cm^2 with and without receiver substrate is shown in Figure 4.45.

The reflection of the shock wave is clearly visible at 1.5 µs, when the corresponding shock wave without receiver is beyond the position of the receiver. At 2 µs, the shock wave crossed the flyer already, without causing visible damages to it. The trajectory does not appear dramatically modified, although a slight deceleration of the flyer is visible. Apparently, the instabilities in the flyer state at this fluence account for the destruction upon arrival on the receiver, and not the impact with the receiver.

4.3.1.3 Effect of the separation distance

The gap of 1 mm seems to be too large to achieve defined material transfer, because the flyer is already falling apart before it has travelled across that distance. On the other

Figure 4.45 Sequence of pictures taken with a sample of 350 nm TP / 80 nm Al at 200 mJ/cm² without and with a receiver substrate at a distance of 1 mm.

hand, a smaller separation between the donor and the receiver may lead to a good transfer. The transfer across a 0.5 mm gap was studied as well to test this possibility.

A sequence of picture taken with a 350 nm TP / 80 nm Al sample at 160 mJ/cm² is shown in Figure 4.46. The separation between the donor and the receiver substrate is 0.5 mm. Again, the pictures were cropped laterally to the size of the gap.

The behaviour of the flyer under these conditions is completely different. Until 0.6 µs, the flyer evolves as expected. At this time, the shock wave has reached the receiver and starts to be reflected. This reflected shock wave "collides" with the flyer at 0.8 µs, resulting in a deformation of the shock front. The central part of the shock wave, which is faster due to the propagation geometry, is slowed down upon contact with the flyer. Indeed, the sides of the shock front, which can travel undisturbed, overtake the middle part after 0.8 µs. This shows clearly the interaction of the shock wave with the solid flyer. The flyer is modified and pushed backward by the shock wave after this interaction. Between 1 and 1.6 µs, the flyer is dramatically deformed and bended backwards. The flyer never reaches the receiver substrate but moves backward, until it eventually falls appart after 1.8 µs.

The fact that the flyer never reaches the receiver is better seen in Figure 4.47, where the position of the shock wave and the flyer was plotted versus time.
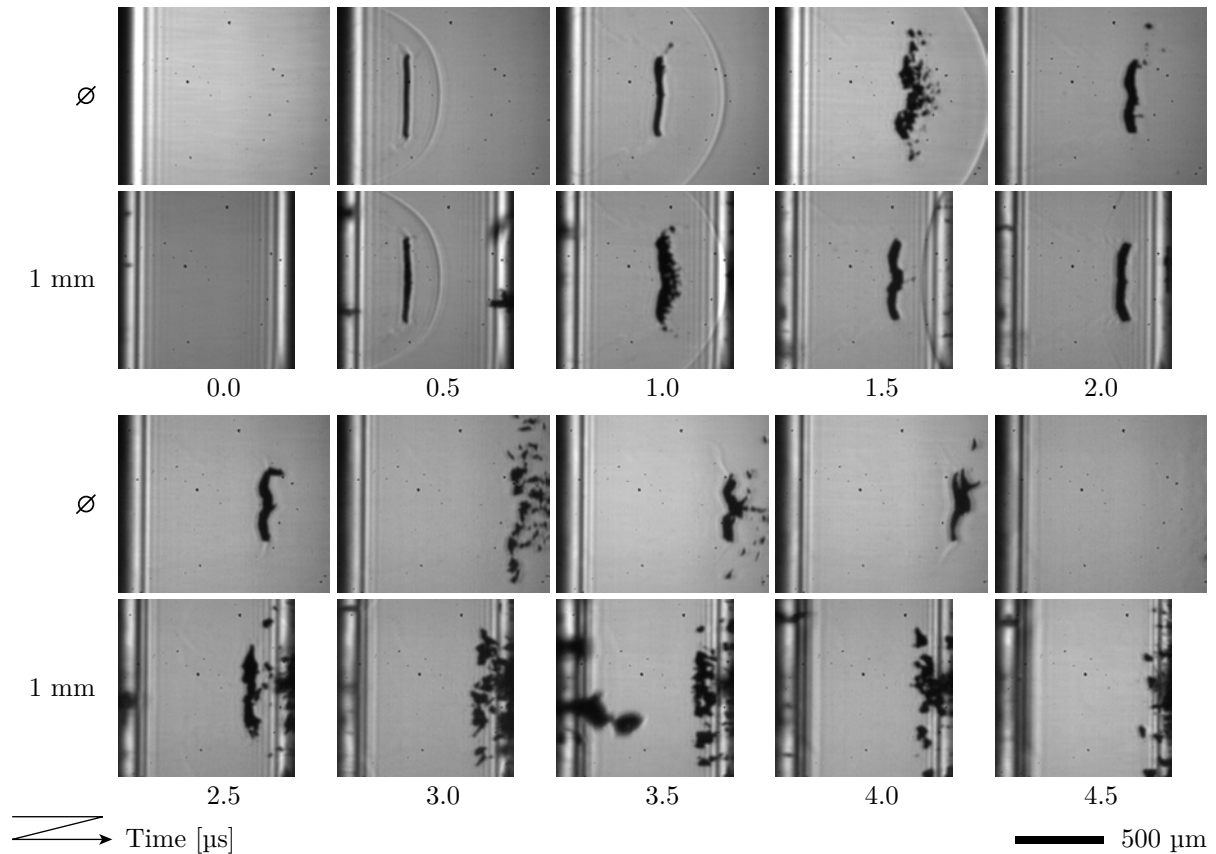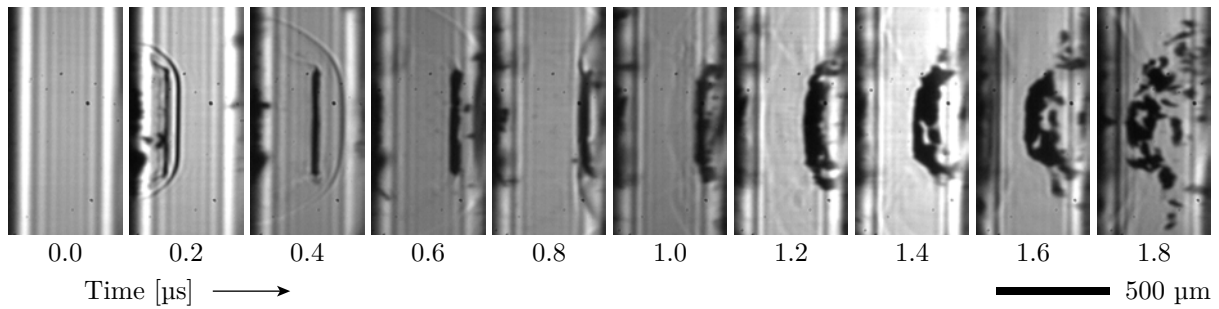
Figure 4.46 Sequence of pictures taken with a 350 nm TP / 80 nm Al sample at 160 mJ/cm^2 with a receiver substrate at a distance of 0.5 mm.
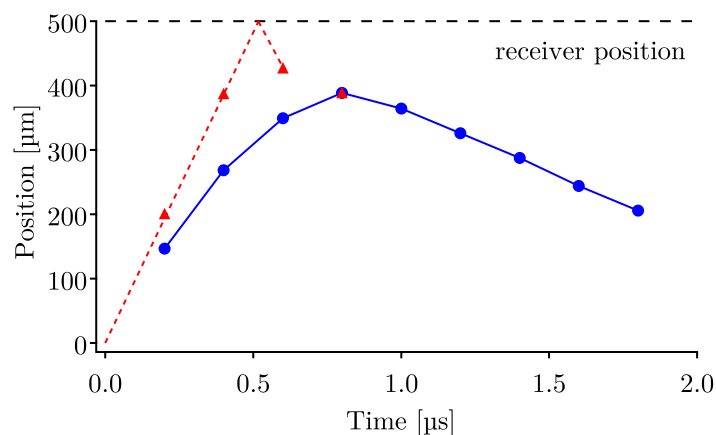
Figure 4.47 Position versus time of the shock wave (▲) and of the flyer (●) measured from Figure 4.46. The lines are guides for the eyes. The position of the receiver is indicated by the horizontal line at 500 µm.

The probable trajectory of the shock wave (▲) is represented by the dashed red line, which includes the reflection at the expected position of the receiver substrate. The actual propagation of the shock wave is not linear with time, but this approximation is precise enough at this early time scale. It is clear from the trajectory of the flyer (●) that the flyer is not fast enough to bounce back from the receiver between 0.6 and 0.8 µs, and that the change in the travel direction occurs due to the interaction with the shock wave.

Different fluences were investigated to see whether this effect can be avoided. The effect of the laser fluence on the transfer is presented in Figure 4.48, where different fluences and time delays are shown. The column on the right shows microscopy pictures of the receiver substrate after transfer (at a different scale).

The fluence range can be divided into two domains according to the way the flyer is affected by the shock wave. The reflection of the shock wave on the receiver substrate causes a destruction and bouncing back of the flyer for fluences $\geq$ 160 mJ/cm^2, in different ways however. The higher the fluence, the more finely dispersed are the flyer fragments visible in the shadowgraphs. The receiver substrate after transfer only contains small
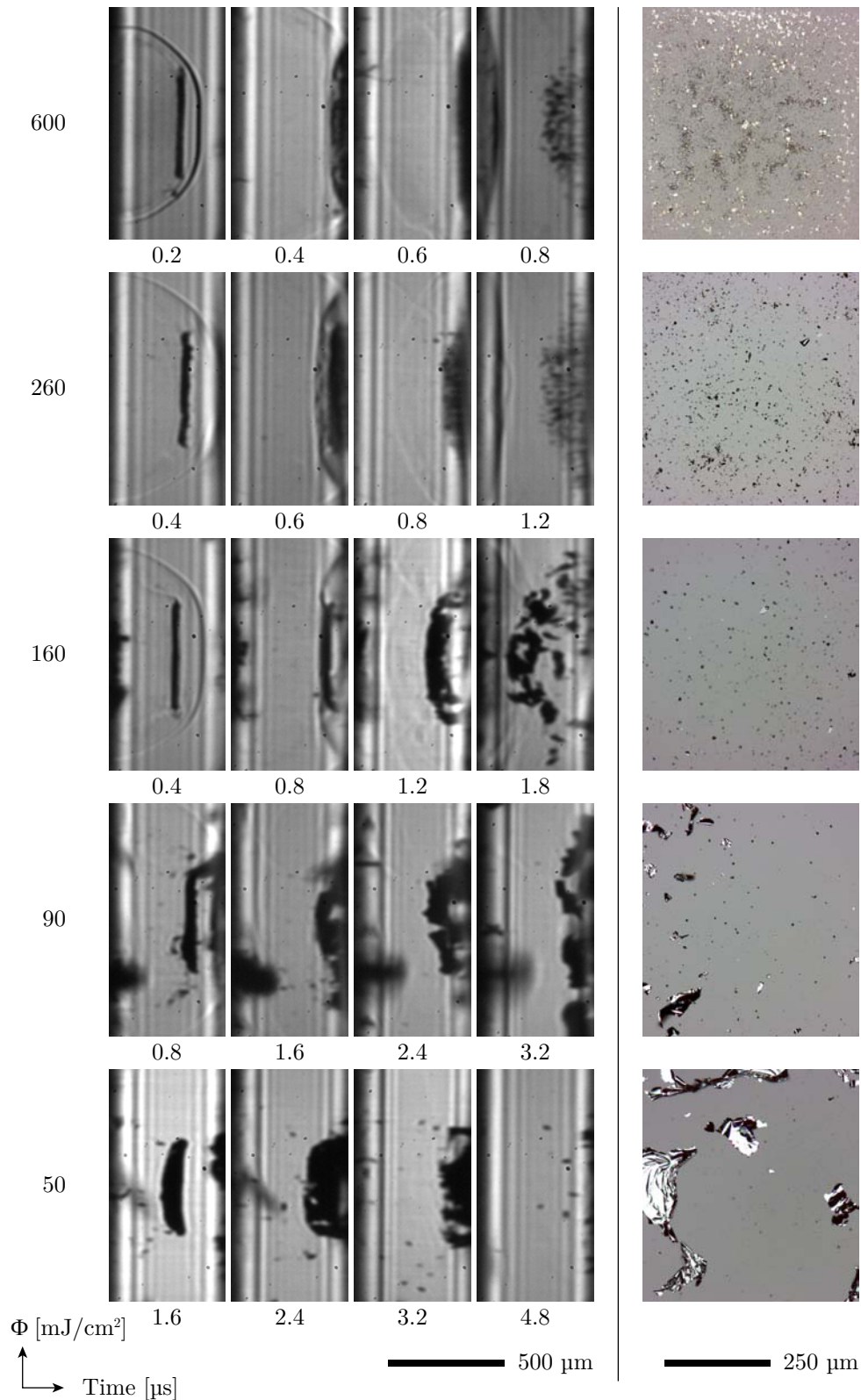
Figure 4.48 Sequence of pictures taken at several fluences (increasing from bottom to top) with a donor sample of 350 nm TP / 80 nm Al and a receiver substrate at a distance of 0.5 mm. The time delays, increasing from left to right and with different values at each fluence, were selected to show the flyer at similar positions. The right column shows optical microsopy images of the receiver substrate after transfer at the corresponding fluences (different scale).

fragments. At the highest fluence, these fragments are shiny and look like melted metal particles, probably due to the violence of the impact and the possible direct irradiation of the metal layer.

Depending on the relative velocity of the shock wave and the flyer, it is possible that the flyer is destroyed and propelled back after impact with the receiver substrate as well. However it is difficult to differentiate in the shadowgraphs between an impact with the shock wave very close to the receiver and an impact with the receiver itself, because the position of the receiver is not well visible.

The low fluence range does not yield good transfer as well, but the flyer is not destroyed by the shock wave, or at least not completely. The flyer reaches the receiver without being propelled back according to the time-resolved pictures. Larger fragments than at the high fluences are found on the receiver plate, with the largest pieces at the lowest fluence (50 mJ/cm^2).

It appears that only strong and fast shock waves affect the flyer. This is the case at high fluences, because the energy and velocity of the shock wave is closely related to the incident laser fluence, as shown before. The shock waves are not strong enough to harm the flyer or propell it back at low fluences.

Transfer was tested as well with a very small gap of 20 µm to see whether such a narrow separation can preserve the integrity of the flyer. In this case, no lateral imaging was possible and only the final state of the transfer is accessible by optical microscopy. A overview of the donor and receiver substrate after the transfer of a 350 nm TP / 80 nm Al film with a 20 µm distance is shown in Figure 4.49, where the fluence increases from left to right. The top row is the donor film while the bottom row shows the receiver substrate. Only a part of the deposition spots is shown, because they all looked similar. For this reason it was not possible to attribute each spot to a precise fluence, which is shown by the arrows on each side of the receiver picture.
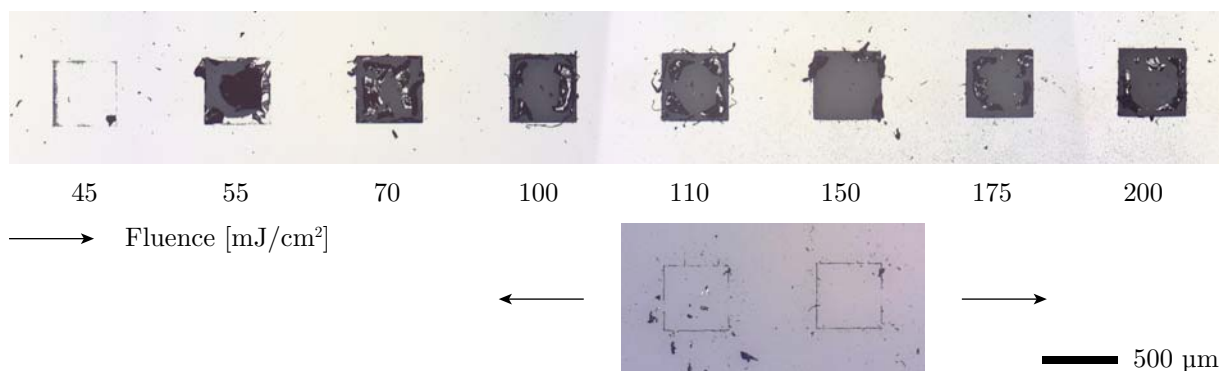

Figure 4.49 Pictures of the donor (top) and receiver substrate (bottom) after transfer from a 350 nm TP / 80 nm Al film across a 20 µm gap at various fluences (increasing from left to right). The position of the receiver cannot be attributed precisely to a fluence since no transfer was obtained and all spot have a very similar aspect.

The film is delaminated between 45 and 55 mJ/cm^2, corresponding to the shadowgraphy observations for larger gaps. Therefore, the threshold fluence for delamination seems not to be affected by the receiver plate in close proximity. There is no material transferred on the receiver substrate and only small fragments are visible. Additionally the edges of the ablated spot are clearly visible on the receiver, which is not yet understood. Large residues of the flyers are found on the donor substrate, showing that the flyer was strongly propelled back by the shock wave and adhered on the donor substrate.

It is clear that the application of a small gap does not improve the deposition of metal flyers. The reflected shock wave has more energy at reduced separations distances and may exert a stronger effect on the flyer. This may explain why no flyer is detected at all on the receiver under these conditions. An investigation by time-resolved front side microscopy would certainly be useful to understand the process.

The shock wave only affects transfer upon a narrow gap (0.5 mm and probably 20 µm as well) because its strength decreases with the travel distance. Indeed, the hemispherical shape and the progression through a medium cause a progessive distribution of the energy in the volume encompassed by the shock front, which is continuously increasing. For a 1 mm separation between the plates, the shock wave is not strong enough anymore to affect the flyer.

At this point, there is a superposition of two counter-productive effects that complicate the problem of the transfer across a gap. First, the state of the flyer depends on the travel distance, and a narrow gap is better for increasing the probability of collecting an intact flyer. Secondly, the shock wave created by the ablation of the triazene layer is affecting the flyer, and the narrower the gap, the stronger this perturbation. Moreover, the fluence yielding an intact and "long-living" flyer is high enough to produce a shock wave which is able to destroy the flyer.

The way of solving this problem could be in the elimination of the shock wave, which is realised in vacuum. The effect of the background pressure on the transfer is now discussed.

4.3.1.4   Effect of the background pressure

The reduction of the background pressure for material ejection showed an increased flyer velocity and no shock wave. The high velocity of the flyer in vacuum could be an issue for a smooth deposition, but the absence of shock wave may solve the problem of the shock wave reflection on the receiver, as discussed above. The transfer was performed in vacuum (typically 5–8·10^{-2} mbar) with the same configuration used in air, i.e. a donor film of 350 nm TP / 80 nm Al and a receiver substrate at a distance of 1 mm to verify these hypotheses. A comparison of two sequences taken in vacuum and in air at a fluence of 160 mJ/cm^2 is shown in Figure 4.50.

The difference between the two pressure conditions is striking. The flyer in vacuum reaches the receiver very quickly (after 1 µs) and a jet of material ejected from the receiver
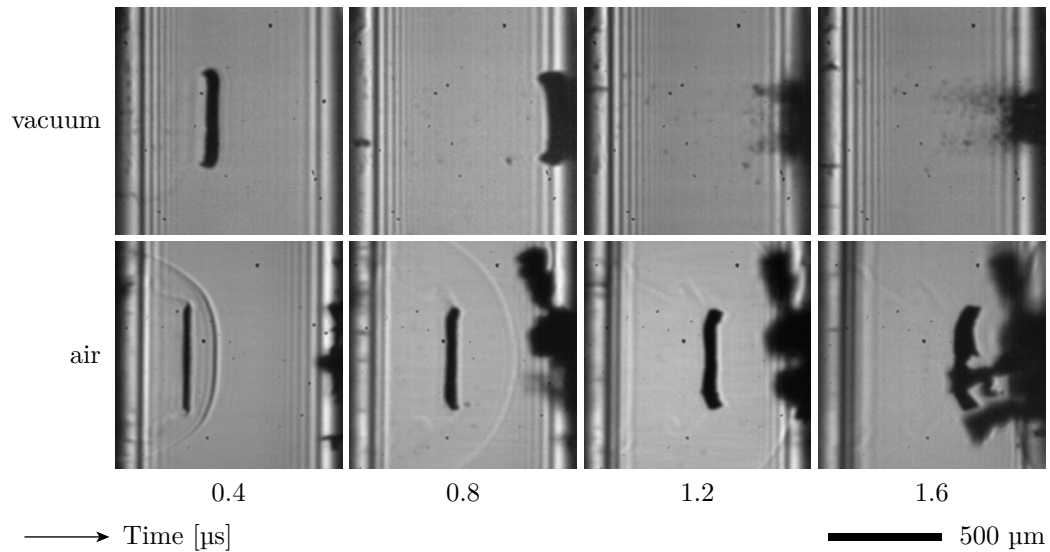
Figure 4.50 Sequence of pictures taken with a donor film of 350 nm TP / 80 nm Al and a receiver substrate at a distance of 1 mm at 160 mJ/cm^2 under vacuum and atmospheric pressure.

substrate is visible immediately after the impact. As comparison, the flyer in air has not arrived on the receiver during the same time.

As shown in Figure 4.39, the flyer reaches the receiver with a velocity of about 1 km/s. In comparison, the velocity in air at this position in only 90 m/s (see Figure 4.33). Assuming that all other conditions are identical, the kinetic energy of the flyer in vacuum is about $(1000/90)^2 \approx 120$ times higher than in air, which may explain why the flyer is immediately disintegrated upon impact and small fragments are ejected backwards.

It is obvious that the conditions resulting in a good flyer in air are not appropriate for smooth deposition under vacuum. The fluence was varied to see whether a good deposition can be obtained for other conditions. Higher fluences (not shown) yield similar results, i.e. strong impact and destruction of the flyer, while a transfer at a lower fluence (90 mJ/cm^2) is shown in Figure 4.51.

The arrival of the flyer follows the same pathway as at 160 mJ/cm^2, but with a weaker impact ($v \approx 700$ m/s). Indeed, the back ejected fragments appear larger and no jet of fine particles is visible as in Figure 4.50. However, the flyer is still destroyed upon arrival. The situation is different at the lowest fluence investigated (50 mJ/cm^2), shown in Figure 4.52.

The flyer is not delaminated in a clean way, as seen after 0.5 µs. The flyer is degraded during the flight and reaches the receiver in a fragmented state resulting in a bad transfer. In this case, the fluence was too close to the ablation threshold and, as shown before, good flyers are not obtained at these conditions.

Although the transfer in vacuum solved the possible problems induced by the reflected shock wave, it introduces a new problem. The flyer travels with such a high velocity that it decomposes upon the impact on the receiver. A decrease of the laser fluence does not seem

Figure 4.51 Sequence of pictures taken in vacuum with a donor film of 350 nm TP / 80 nm Al and a receiver substrate at a distance of 1 mm at a fluence of 90 mJ/cm^2.

to be the solution, because the quality of the ejected flyer is reduced at lower fluences. At this point, no operating window was found to conciliate these two contradictory processes. A solution may be the application of pressure between the applied vacuum and ambient conditions, which may slow down and buffer the flyer before arrival while avoiding a strong and destructive shock wave. The use of other background gases may also be a solution.

4.3.2   Transfer of a bilayer system

The next step towards the deposition of OLED materials is the transfer of bilayer samples of Al/MEH-PPV. It was shown in Section 4.2.2 that the introduction of an additional layer of the MEH-PPV polymer has a positive influence on the quality of the flyer. Therefore, one may expect an improvement of the transfer with a gap for bilayer samples of Al/MEH-PPV.

An overview of the results at atmospheric pressure is shown in Figure 4.53. The left part of the figure shows sequences of pictures of the transfer with a 1 mm gap of a 350 nm TP / 80 nm Al / $\sim$ 50 nm MEH-PPV donor film at different fluences (increasing from bottom to top). The corresponding view of the receiver substrate is shown in the right column at a different scale.

The transfer of flyers of Al/MEH-PPV seems to be much smoother compared to a single Al layer, although no flat deposition is obtained. No fragmentation upon arrival is observed, except at the highest fluence (400 mJ/cm^2). This confirms the previous observations that flyers containing an additional MEH-PPV layer are less brittle. The ejected pixels can fly in a better shape, but are also less sensitive to the impact with the
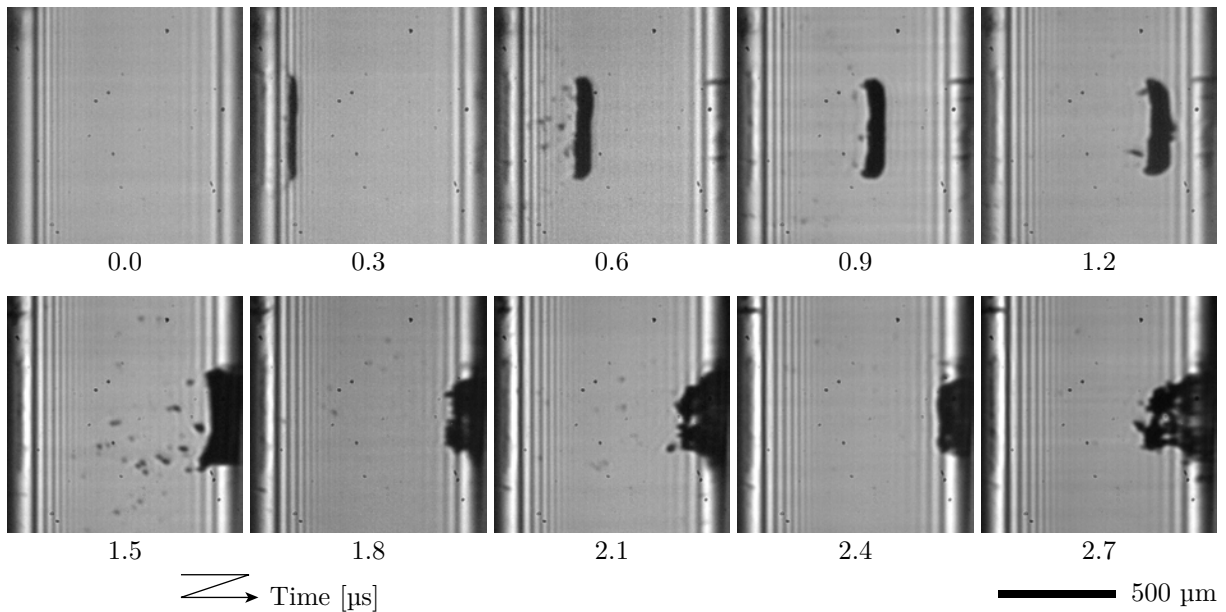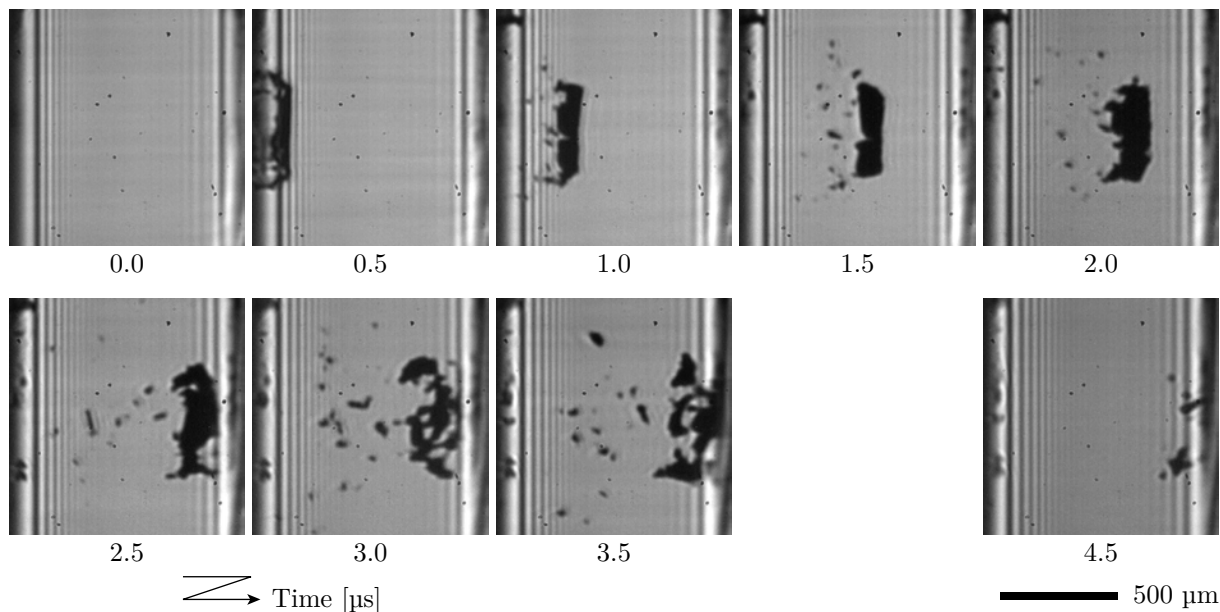
Figure 4.52 Sequence of pictures taken in vacuum with a donor film of 350 nm TP / 80 nm Al and a receiver substrate at a distance of 1 mm at a fluence of 50 mJ/cm^2.

receiver and the reflected shock wave.

It is noteworthy that the shape of the flyer after 4 µs is closely related to the shape of the deposited pixel. For instance the "intact" flyers visible at 180 and 220 mJ/cm^2 clearly correspond to the best depositions. In turn, the flyer "landing" at 280 mJ/cm^2 is split in the center, which yields a pixel in the corresponding state. The hole found in the deposited pixel at 220 mJ/cm^2 may be have been done by an overpressure, created by the flyer compressing air in front of it while reaching the receiver. The funnel-like shape of the flyer after 4 µs seems to indicate that a perforation of the flyer occured, which confirm this hypothesis.

A close-up view of pixels transferred at 160, 180 and 220 mJ/cm^2 is shown in Figure 4.54 (no shadowgraphy data are avaiblable for 160 mJ/cm^2). The top view is taken from the deposition side, while the bottom view is taken through the glass substrate, revealing the orange MEH-PPV layer. The selected spots correspond to other locations than shown in Figure 4.53 (right column) but are obtained at the same fluence.

The deposited pixels reveals a folded and shrunk appearance. A part of the film is flipped over, as visible from the orange part facing upwards. Although the pixels obtained are not perfect and would certainely have short circuits, the whole flyer was transferred in one part, which was almost impossible for a single Al layer (see Figure 4.44). These results are encouraging and it is likely that a better deposition across a gap may be achieved by tuning the parameters such as the gap distance and the background pressure.
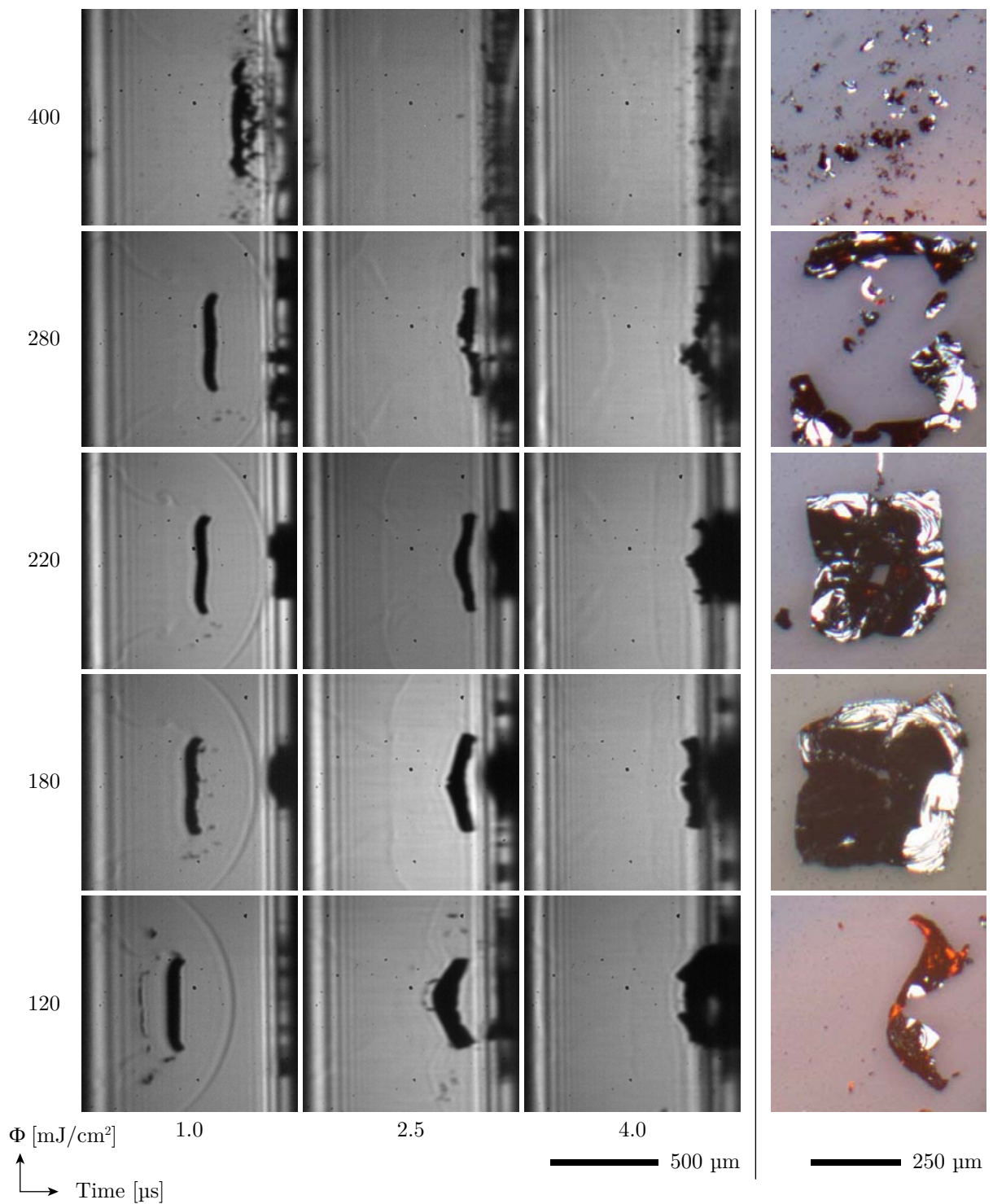
Figure 4.53 Sequence of pictures taken at several fluences (increasing from bottom to top) with a donor sample of 350 nm TP / 80 nm Al / $\sim$ 50 nm MEH-PPV and a receiver substrate at a distance of 1 mm. The time delay increases from left to right. The right column shows optical microsopy pictures of the receiver substrate after transfer at the corresponding fluences (different scale).
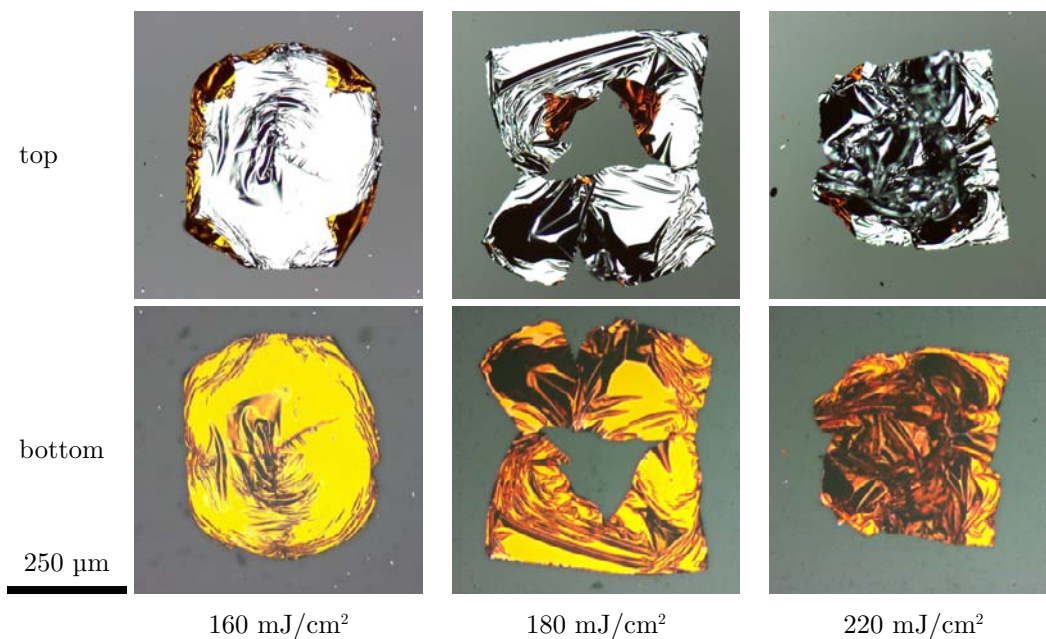
Figure 4.54 Optical microsopy pictures of pixels deposited at three different fluences. The donor film was made of 350 nm TP / 80 nm Al / $\sim$ 50 nm MEH-PPV and the transfer was realised in air with a 1 mm gap. The top view corresponds to the pixel from the deposition side, while the bottom view is obtained through the substrate.

4.4 Material transfer in contact

In the previous section, it was shown that the flyer ejected from a donor film could be deposited onto a receiver substrate placed at a given distance of the donor plate, however without reaching the quality required for an OLED building block. In particular, the folding of the pixel occuring during the flight may be very problematic for an electronic device, due to short circuits created by the Al electrode touching the substrate.

While an improvement of the deposition across a gap may be achieved, it is possible that a better transfer may be achieved when no free space is present between the donor and the receiver substrates. The transfer was therefore investigated without gap, i.e. with the donor and the receiver plates in close contact.

4.4.1 Transfer of a single layer[6]

The transfer of the model system of triazene and aluminum was studied, as well as other donor materials, in order to investigate the influence of the material properties on the quality of the transfer. The metal transfer is discussed first.

---

[6]The content of this section was published in [113].

4.4.1.1   Influence of the laser fluence

The standard 350 nm TP / 80 nm Al sample was transferred with the donor and the receiver substrates in contact. An overview of the donor (up) and receiver substrates (down) after the transfer is presented in Figure 4.55 for various fluences.
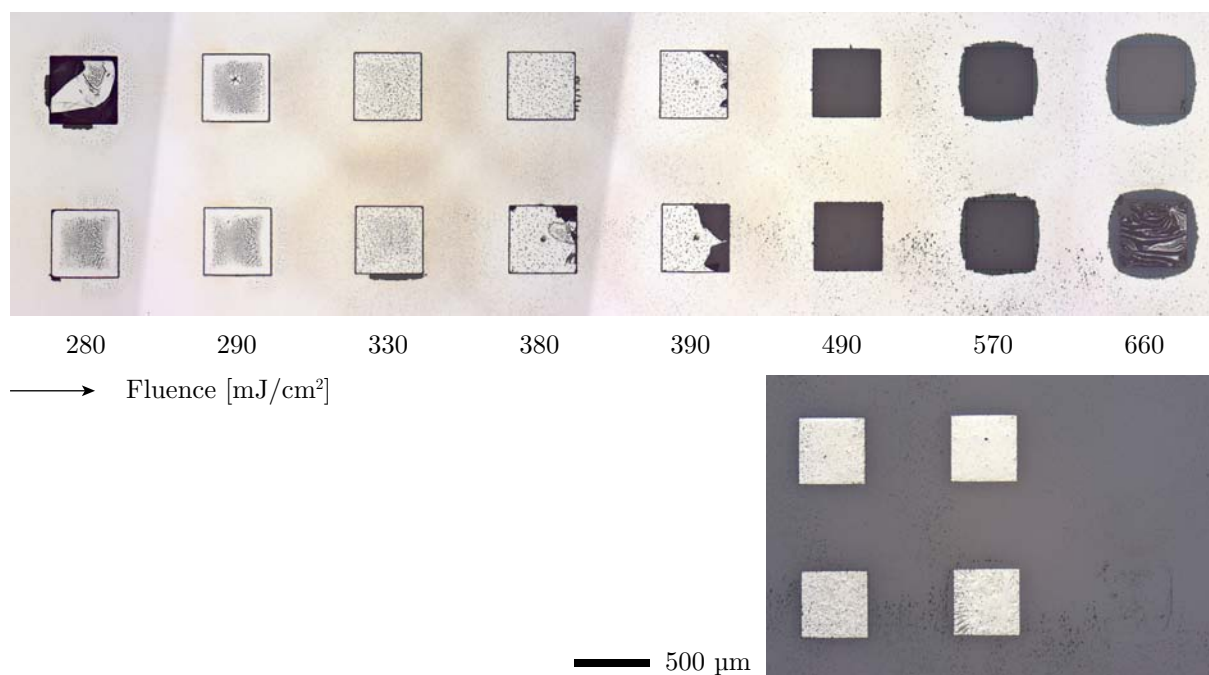
Figure 4.55 Image of a donor (top) and receiver substrate (bottom) after transfer of aluminum. The receiver is shown only for the three highest fluences, as no transfer was observed in the other cases. The donor film was made of 350 nm TP / 80 nm Al. The fluence (indicated) was varied horizontally and repeated twice (vertically).

The triazene layer was 350 nm thick and each fluence was investigated twice. A clean transfer is achieved between 490 and 570 mJ/cm^2. The donor spot is delaminated, i.e. all the material is removed from the irradiated spot, and the material is transferred, i.e. the pixel can be found intact on the receiver. No transfer and delamination occur at lower fluences, although the square edges are clearly cut-out, even at 200 mJ/cm^2. This effect is certainly helpful to avoid a tear-off of the Al film. Above 300 mJ/cm^2, a halo of black particles surrounds each spot. This might be the result of the triazene decomposition and shockwave propagation in the substrate plane, or more probably, direct ablation of the metal layer. Above 660 mJ/cm^2 only delamination occurs but no material is transferred.

There is an optimum fluence between an insufficient burst and an excessive irradiation of the transfer layer. At too low fluences, not enough triazene is decomposed and the generated pressure cannot overcome the mechanical resistance of the overlaying material. On the opposite, when too high fluences are applied, the triazene layer no longer acts as a protecting barrier and the transfer material receives a large amount of the laser energy, resulting in damages by melting or direct ablation of the metal. The top layer is then

fragmented and destroyed upon transfer.

Figure 4.58 (a) shows a magnified view and a profile of the transferred pixel at 570 mJ/cm², upper line. It has well defined edges and no holes. Some black particles are visible on and around the pixel, as mentioned above. The profile is quite smooth except for some spikes originating from ablation debris.

The transfer in contact gives better results than across a gap. One reason may be related to the flyer, which cannot be deformed while trapped between the plates and therefore stays flat. The consequence is that the physical separation of the the donor and receiver substrates at the end of the experiment was critical, because the pixels can be easily deformed or destroyed if the plates slide onto each other. Several samples were destroyed in this way when not enough care was taken to prevent the substrates from sliding onto each other. This problem does not happen for the transfer with a gap. The shock wave, which should still exist, seems not to be an issue here, probably because of the geometrical reasons mentioned above.

It is noteworthy here that the fluence needed to delaminate the film is much higher in contact than upon free ejection ($\sim$ 490 versus $\sim$ 50 mJ/cm² respectively). However, it appears from Figure 4.55 that the ablation spot is already well-cut at fluences lower than 490 mJ/cm², but the pixel was not transferred. As the flyer cannot be really separated from the donor in this geometry, an additional pressure may be necessary to achieve an adhesion of the pixel on the receiver plate. This hypothesis would explain the difference of fluence observed for contact and gap transfer.

4.4.1.2 Influence of the triazene thickness

The thickness of the triazene is also important, because together with the applied fluence, it determines the amount of gas formed and the remaining thickness of non-ablated triazene. Transfer of aluminum was investigated with different triazene thickness (from 0 to 350 nm) while keeping the Al layer unchanged to assess these effects. An example of transfer with a 100 nm TP / 80 nm Al film is shown in Figure 4.56.

No pattern transfer was obtained with a triazene thickness of 100 nm, nor with any other tested thickness, i.e. from 0 to 200 nm (not shown). A clean transfer was only achieved with a thick layer of triazene (350 nm). The first hypothesis was that a part of the triazene layer would stay on the metal film and mechanically stabilise it, which is beneficial for the transfer, as shown by the shadowgraphy observations, where the best flyers were obtained with the thickest triazene layer (see Figure 4.34).

The transferred pixel would be thicker than the donor Al layer for this mechanism. The data in Table 4.4 reveal that this is not true, the pattern on the receiver is slightly thinner than the starting film. Indeed, the expected thickness of undecomposed triazene at 570 mJ/cm² is very low, as seen from Figure 4.32.

Transfer of Al without release layer did not yield satisfactory results for the investigated conditions. Only particles appearing dark were deposited on the receiver.
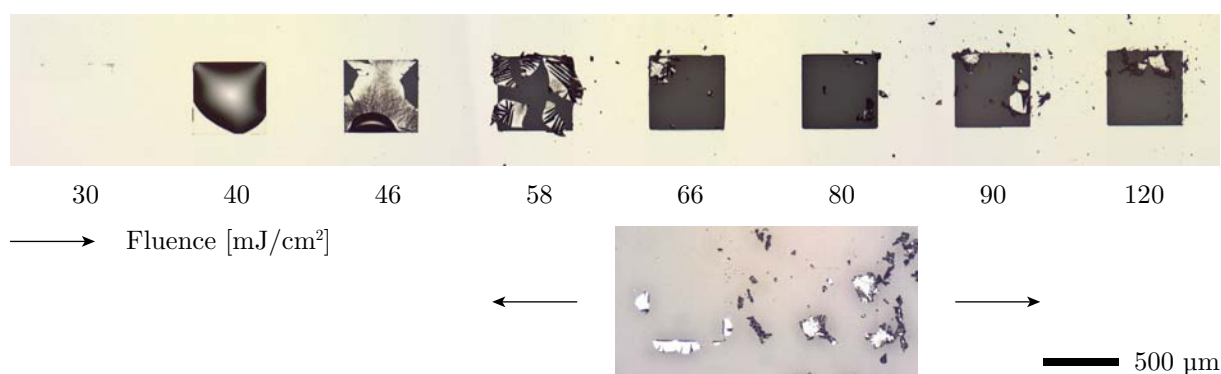
Figure 4.56 Image of a donor (top) and receiver substrate (bottom) after transfer of aluminum from a 100 nm TP / 80 nm Al film at various fluences (increasing from left to right). The position of the receiver cannot be attributed precisely to a fluence since no transfer was obtained and all spot have a very similar aspect.

More information can be gained from these experiments. For each sample, the fluence at which a complete delamination of the irradiated spot occurs was determined by visual inspection of the donor substrates. These delamination fluences are summarised in Figure 4.57.
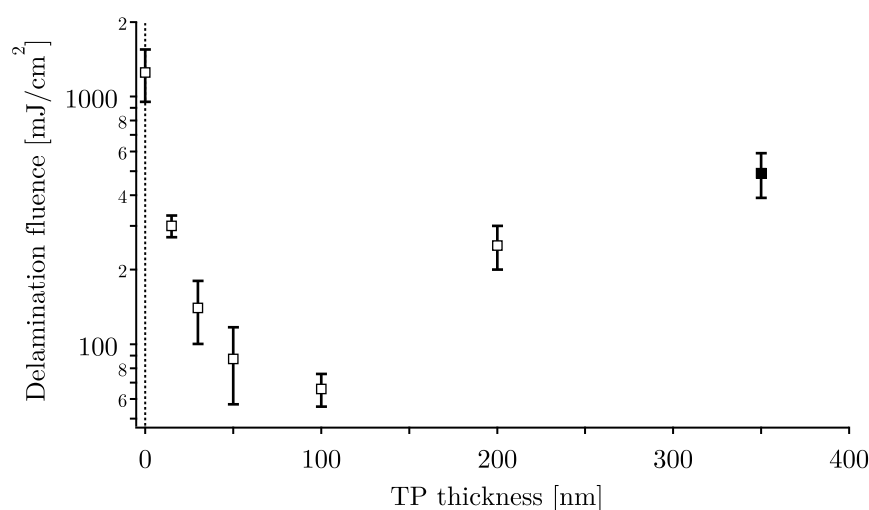
Figure 4.57 Minimal fluence required for the delamination of Al donor pixels as a function of triazene thickness. The succesful transfer condition is indicated by the filled symbol.

They depend strongly on the thickness of the release layer. For layers above 100 nm, the fluence increases with film thickness. A minimum is reached around 100 nm. Below that thickness, the fluence increases again with decreasing film thicknesses, up to the value measured without triazene layer. A comparison with the delamination fluence of pure triazene would certainly yield a good correlation and will be further investigated.

The trend between 100 and 350 nm is easily understandable, because a thicker film needs a larger fluence to be fully ablated. The values between 50 and 15 nm are also in accordance with the ablation behaviour of very thin triazene films. It was shown in Section 4.1.2.1 that the ablation threshold of films thinner than 50 nm strongly increased with decreasing thicknesses, due to thermal diffusion into the substrate and reduced absorbed energy. As the delamination fluence depends on the ablation threshold, the former will increase as well. A thin triazene film can therefore not play its protecting role for the Al layer, and a large amount of energy is deposited in the metal. Another effect may be important: for too thin layers, the amount of triazene becomes too small to provide the thrust needed for overwhelming the mechanical resistance of the metal. Therefore, delamination occurs by a mixture of triazene decomposition and metal ablation, which turns completely into the latter for a pure Al donor. The delamination fluence increases as Al has a higher threshold fluence than triazene.

The triazene thickness appears to be a crucial parameter for the process, because it determines the fluence needed for delamination, which is a necessary but not sufficient condition to get clean transfer. For minimising damages to the transfer layer, it is desired to work at the lowest possible fluence, thus with a triazene layer of ~ 100 nm in this case. Thinner films are not advantageous because the ratio between needed fluence and fluence transmitted is completely defavorable and the benefit of using a sacrificial release layer is almost lost. The upper thickness range is clearly the interesting zone, and further investigations may be needed to understand why transfer of Al requires a thick release layer.

4.4.1.3 Influence of the transfer material

Our LIFT method is not only intended to transfer metal layers, but many other materials, in particular polymers. These have to be spin coated on the triazene layer to prepare the donor substrates. Therefore, they must be soluble in a different solvent than chlorobenzene or cyclohexanone, otherwise the release layer would be washed out during spin-coating of the polymer. To avoid this, two water-soluble polymers were chosen, gelatine and methylcellulose. Besides having different mechanical properties than metals, they are also possible carrier materials for the transfer of biological molecules or even cells.

The thicknesses of the triazene and top layers are given in Table 4.4, together with typical elastic moduli, tensile strengths and elongations of the top layer materials, taken from literature. Similar thicknesses were used for both samples, in order to allow a direct comparison. Figure 4.58 (b) shows a transferred pixel of eosine-dyed gelatine with its corresponding profile obtained at 140 mJ/cm². The eges are sharp and the pixel is full, however with a very rough surface. Gelatine is a protein and may have undergone denaturation and conformational change during the transfer, which leads to a possible spatial rearrangement and roughening of the surface. Another explanation is that the residual water trapped in the polymer network was brought to boil and produced bubbles
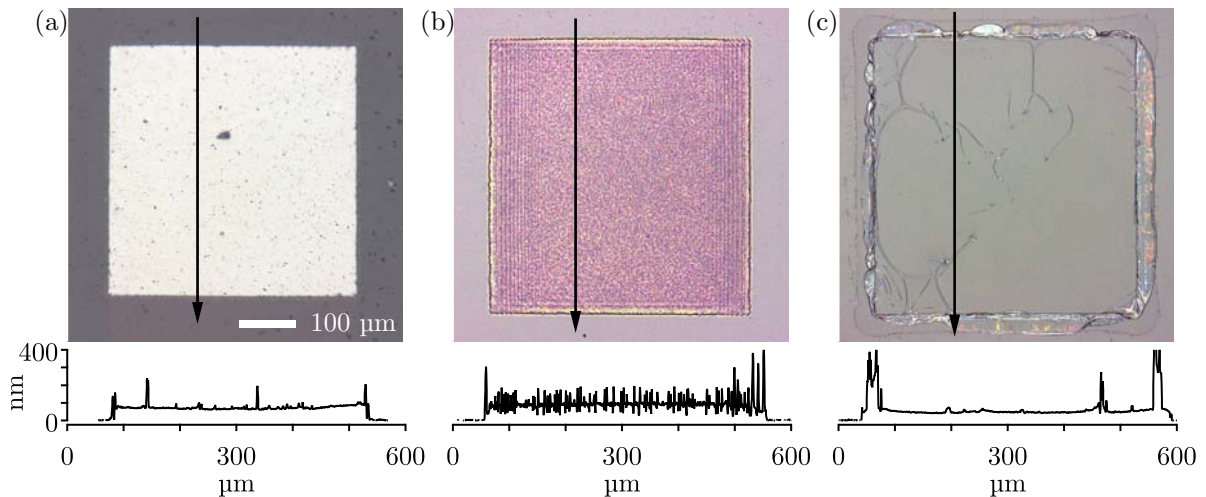
Figure 4.58 Pictures and corresponding profiles of transferred pixels: (a) aluminum at 570 mJ/cm^2, (b) gelatine dyed with eosin at 140 mJ/cm^2, (c) methylcellulose at 620 mJ/cm^2. The location of the profile is indicated by the arrow.

within the layer. In both cases, this material is a very good indicator of the thermal stress induced by the process. A non-reproducible, partial pixel of gelatine (not shown) was obtained at a lower fluence (45 mJ/cm^2) and the microsopy as well as the surface profilometry revealed a very smooth surface in this case. Unfortunately, the required fluence to get a full transfer is higher than what the transfer material can support without damages.

A transferred methylcellulose pixel is shown in Figure 4.58 (c) with its profilometry trace. The donor film had approximately the same thickness as for gelatine, but the fluence needed to achieve a good transfer was much higher, namely 620 mJ/cm^2. Clearly, the shape of the pixel is not so well delimited. The edges consist of teared out film that did not adhere to the receiver substrate. The profile of the donor substrate (not shown) indicates that the square of delaminated methylcellulose was larger than the laser spot size, defined by the triazene ablation crater. As seen from Table 4.4, the methylcellulose film is less stiff than gelatine but much more ductile. Instead of breaking into pieces, the pixel edges get folded upon transfer, which yields the ripples observed in Figure 4.58 (c). Except this, the film is very smooth and also visually free of defects.

An issue related to the large difference in fluence is the thickness of the transferred films. These values are summarised in Table 4.4 as well. While the transferred film of gelatine is almost as thick as the donor layer, the pixel of methylcellulose lost half of its thickness upon transfer. Obviously, a part of the methylcellulose layer was directly ablated by the high fluence pulse. One way to improve the transfer would be to use a thicker triazene layer, which would provide stronger propulsion while keeping a sufficient barrier to irradiation.

From these first experiments, it appears that a certain stiffness is required to get a

Table 4.4 Layer thickness and mechanical properties of the materials

	aluminum	gelatine	methylcellulose
Thicknesses [nm]			
triazene	350	100	90
donor top layer	82	110	100
transferred pixel	76	97	48
Elastic modulus [GPa]	28-71[a]	3.0-5.6[b]	1.2[c]
Tensile strength [MPa]	151-166[a]	77-115[b]	10-12[c]
Elongation to break [%]	18-23[a]	3.0-4.7[b]	7-14[c]

[a]From [114, 115]
[b]From [116–119]
[c]From [120, 121]

sharp cut of the pixel. If the material is too soft, like methylcellulose, it will absorb the energy and deform. Aluminum and gelatine films allow sharp pixel transfer while the transfer of soft methylcellulose results in ill-defined pixels. As infered from the mechanical properties given in Table 4.4, the elastic modulus of methylcellulose is significantly smaller than the one of aluminum or gelatine. Consequently, the burst induced by the laser pulse will be largely dissipated in the soft methylcellulose film by deformation. Only a strong burst can induce the transfer, with the consequence that the top material absorbs laser energy.

On the opposite, stiff materials like metals allow an easy delamination but have the tendency to break into pieces. Although the mechanical properties of films under fast strain rate (impact) may be very different from the static properties of the bulk, available in the literature, there is a hint that stiffness is an important parameter for controlling the transfer process. In correlation with the elastic moduli, high tensile strengths will result in sharp pixel transfer, while elongation to break does not seem to be critical in the present work.

The influence of the mechanical properties may also depend on the triazene film thickness, because the latter changes the mechanical properties of the flyer. Therefore, a more comprehensive study of the process, including a systematic analysis of various triazene film thicknesses at a different fluences, would certainly help to get a clear picture of the mechanism. In that sense, it is most probable that the additon of a second donor layer influences the transfer. The case is now discussed with the transfer of bilayer films.

4.4.2 Transfer of a bilayer film

The deposition of metal was successful and the next step is to deposit OLED building blocks, i.e. a bilayer film of Al/MEH-PPV. The 308 nm excimer laser as well as the

picosecond Nd:YAG (355 nm) were used to study the influence of the energy beam profile and pulse length on the deposition.

4.4.2.1 Excimer laser

Different triazene film thicknesses were studied beside the standard 350 nm. The result of a transfer with a 100 nm TP / 80 nm Al / ~ 20 nm MEH-PPV is shown in Figure 4.59.
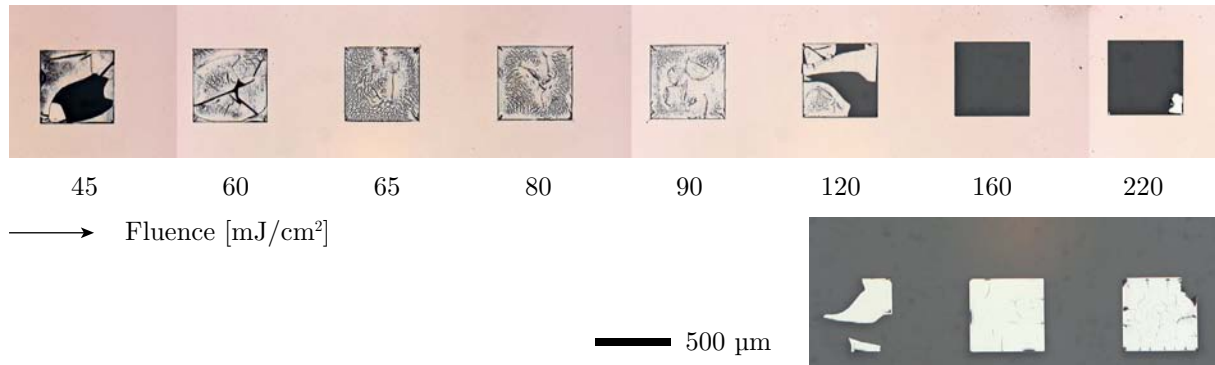

Figure 4.59 Image of a donor (top) and receiver substrate (bottom) after transfer of Al/MEH-PPV at various fluences (increasing from left to right). The receiver is shown only for the three highest fluences, as no transfer was observed in the other cases. The donor film was made of 100 nm TP / 80 nm Al / ~ 20 nm MEH-PPV.

A good pixel transfer is observed at 160 mJ/cm^2. Below that fluence, no delamination occured, similar to what was observed for the TP/Al sample, however at a different fluence range. At the highest fluence (215 mJ/cm^2), the pixel is almost integrally transferred, but some cracks are visible on the surface. This fluence is therefore too high for achieving a soft transfer.

A successful transfer was obtained with a relatively thin TP film (100 nm), where no good Al transfer was obtained (see Figure 4.56). The improved mechanical stability brought by the additional MEH-PPV layer is here again playing an important role, although the pixel does not have to fly across a gap in this case. Additional, the MEH-PPV is softer than the metal, which may also help to "land" smoothly on the reciever and to improve the adhesion.

A detail view of a pixels transferred at 160 mJ/cm^2 is shown in Figure 4.60 together with the corresponding ablated spot. The deposited pixel is shown from the top and from the bottom (through the glass substrate).

The shape of the deposited pixel is very regular with sharp-defined edges, corresponding well to the ablated area, where a clean delamination occured. Some cracks are visible on the pixel, which are in the Al layer and maybe in the MEH-PPV as well, which is difficult to determine.

The deposited pixel appears to be very good and the last step is to verify if such a pixel is functional. Before this, the transfer with the picosecond laser is shown.
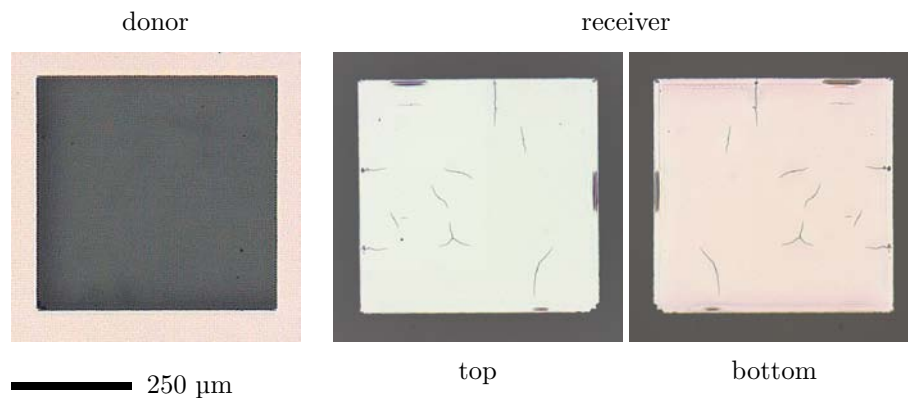
Figure 4.60 Detailed view of the donor film and of the deposited pixel (seen from both sides) after irradiation at 160 mJ/cm^2. The donor film was made of 100 nm TP / 80 nm Al / $\sim$ 20 nm MEH-PPV.

4.4.2.2 Picosecond Nd:YAG laser

As mentioned previously, material deposition using a solid-state laser is interesting for an industrial application of the technique, because higher throughput can possibly be achieved with this kind of laser, due to the higher possible repetition rate. It was shown in the previous sections that the poor energy profile of the ps / 355 nm laser laser beam has a negative influence on the quality of the TP ablation craters as well as on the ejected flyers. The question arising now is whether a good transfer in contact can nevertheless be achieved with this laser.

Figure 4.61 shows an overview of the transfer performed with a 100 nm TP / 80 nm Al / $\sim$ 60 nm MEH-PPV sample at different fluences (increasing from left to right). The reproducibility is compared with the two identical lines. The colour difference with the sample shown in Figure 4.59 is due to the different MEH-PPV thickness.

The transfer upon picosecond irradiation is different than observed with the excimer laser. The film is delaminated at all investigated fluences, but only partially. It is likely that the delamination threshold is lower than the investigated fluence range, however no data are available below 40 mJ/cm^2.

There is no apparent link between the fluence and the quality of the shape of the ablated spot or transferred pattern, except that a lower transfer quality is observed at the highest fluences (above 90 mJ/cm^2). The reproducibility of the transfer at the same fluence supports this observation.

A detailed view of a pixel transferred at 60 mJ/cm^2 is shown in Figure 4.62 together with the corresponding ablated spot. The deposited pixel is shown from the top and from the bottom (through the glass substrate).

The edges of the pixel are very irregular, corresponding to the shape of the ablated crater. On the other hand, the surface of the pixel appears very smooth and no cracks are visible. The nanosecond-deposited pixel shown in Figure 4.60 for comparison have a very
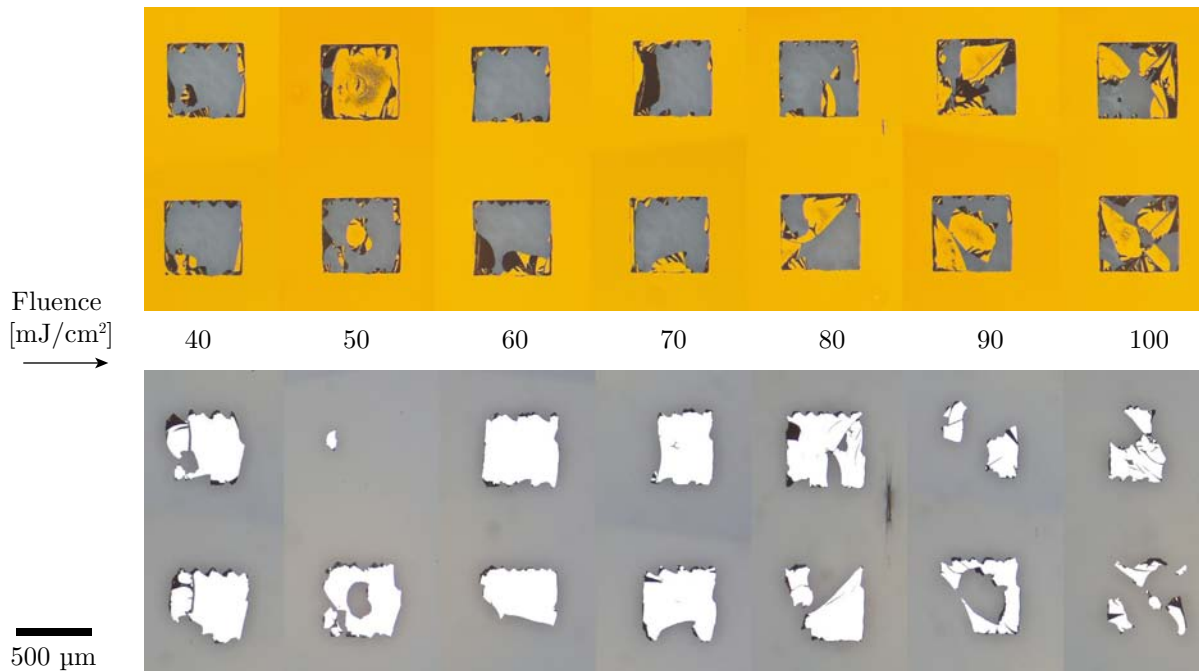
Figure 4.61 Image of a donor (top) and receiver substrate (bottom) after transfer of Al/MEH-PPV at various fluences (increasing from left to right, repeated twice) with the ps / 355 nm laser. The donor film was made of 100 nm TP / 80 nm Al / ~ 60 nm MEH-PPV.

well-defined shape but exhibits cracks on the surface. A much higher fluence was needed to achieve the transfer (160 versus 60 mJ/cm²) with the ns laser, which may explain the difference in the surface quality.

A white border is visible on the MEH-PPV-coated side of the pixel, which may be an artifact of the observation or the sign that the pixel does not adhere well at the border. It may also indicate a bleaching of the MEH-PPV at this location, but this seems less probable.

Two conclusions can be drawn here. The use of an inhomogeneous laser beam yields very poor edge quality and only a partial pattern transfer. However, the transfer can be achieved with a picosecond laser at a lower fluence compared to the nanosecond laser. This fact is very promising for material transfer with a very limited heat load, in addition to the lower heat diffusion discussed in Section 4.1.2.3. Further investigations with a homogenised ps laser beam may be a very positive direction for LIFT.
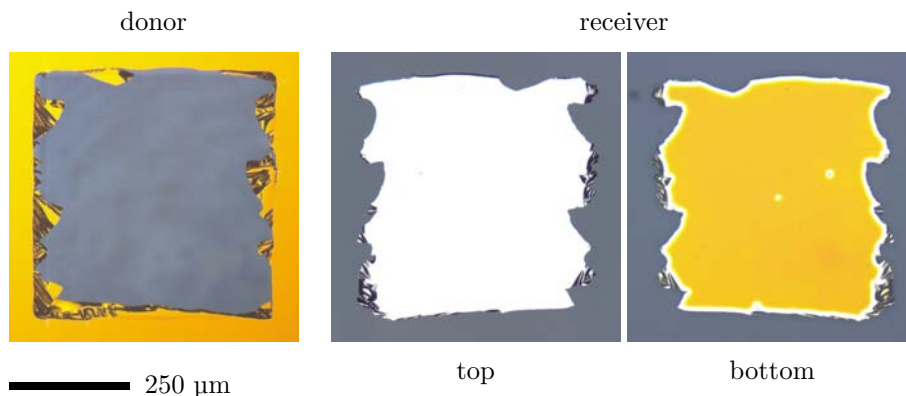
Figure 4.62 Detailed view of the donor film and of the deposited pixel after irradiation at 60 mJ/cm^2 with the ps / 355 nm laser. The donor film was made of 100 nm TP / 80 nm Al / $\sim$ 60 nm MEH-PPV.

4.5 Fabrication of OLED pixels[7]

The last step of this work is the fabrication and characterisation of functional OLED pixels. The system chosen is described in Section 2.1.3 and is based on the luminescent polymer MEH-PPV.

4.5.1 Transfer of pixels

A succesful transfer of an Al/MEH-PPV bilayer was demonstrated in the previous section. The last part of the work is to complete the OLED architecture. The MEH-PPV is the electroluminescent material and the Al layer is the cathode. To build an OLED, the system has to be transferred onto an anode, in order to yield a sandwich architecture of MEH-PPV between two electrodes.

The anode has to be transparent, because light is emitted through one of the electrodes and the Al cathode is opaque. The selected anode material is tin-doped indium oxide (ITO), a transparent and conducting oxide, whose energy level match the HOMO level of the MEH-PPV.

In order to build a functional pixel, the bilayer has to be transferred onto an ITO layer but in a way that allows to establish an electrical connection. One possible design allowing such a connection is shown in Figure 4.63.

Electrical contact is made by metal pins touching the film from the bottom. The thicknesses of the layers is in the sub-micrometer range, where a problem can arise if the metal pin crosses all layers down to the ITO. If a contact with Al is done with the ITO layer below, it is highly probable that a short circuit will occur between the Al and the ITO though the metal pin. The Al/MEH-PPV pixel is transferred across an ITO edge, therefore creating an active zone with ITO below and a contacting zone without ITO. The

---

[7]The content of this section was published in [122].

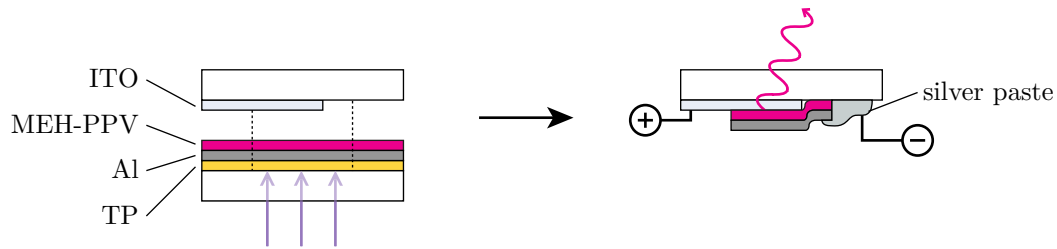**Figure 4.63** Building principle of the OLED: an Al/MEH-PPV pixel is transferred across the ITO layer. A conductive path of silver is painted on the pixel part which is not in contact with the ITO. This configuration allows to avoid short circuits between the silver paste and the ITO. The diode is then electrically contacted through the ITO and the silver paste.

electrical contact to the Al layer is then achieved at a location where no ITO is present. The location of the metal pin has to be linked for practical reasons to the pixel with a silver paste line. The contact to the ITO is established outside the pixel area as well.

The layers of MEH-PPV transferred previously had a thickness between 20 and 60 nm. With such thin layers, dust particles that may be present on the donor film or on the receiver before transfer would very easily create short circuits in the device. Therefore, thicker layers of MEH-PPV were used, i.e. 100 nm TP / 80 nm Al / 90 nm MEH-PPV, to avoid additional problems with dust. Optimal transfer conditions in contact were obtained with this sample at a fluence of 250 mJ/cm^2 (308 nm excimer laser), which is higher than for the samples containing a 20 nm MEH-PPV layer (160 mJ/cm^2 in that case).

While all the steps of donor sample preparation and device characterisation were done under inert atmosphere, the samples had to be exposed to air during the laser transfer, i.e. for about 15–30 minutes. A picture of pixels transferred in this way is shown in Figure 4.64.

The pixels were transferred across the ITO stripe, which is visible in the center of the substrate in Figure 4.64 (b). A selected pixel is shown in Figure 4.64 (c). The Al layer is visible on top, below is the MEH-PPV layer and the round dark shape on the right is silver paste. Interestingly there is a thin MEH-PPV border surrounding the aluminum pixel. The ablation crater on the donor substrate confirms that the MEH-PPV pixel is slightly larger than the Al pixel. We attribute this feature to the different mechanical behaviour of the polymeric layer compared to the aluminum film. This effect is particularly helpful in the construction of light-emitting diodes, since it avoids short circuits between the transferred aluminum electrode and the ITO.

A bottom view from the ITO side of two pixels is shown in Figure 4.64 (d). The square on the right of the pixels in contact with the ITO anode is the active area. The left part is on glass, where the contact to the Al layer was obtained by using silver paste.

The final part now deals with the testing of the device by applying a voltage.
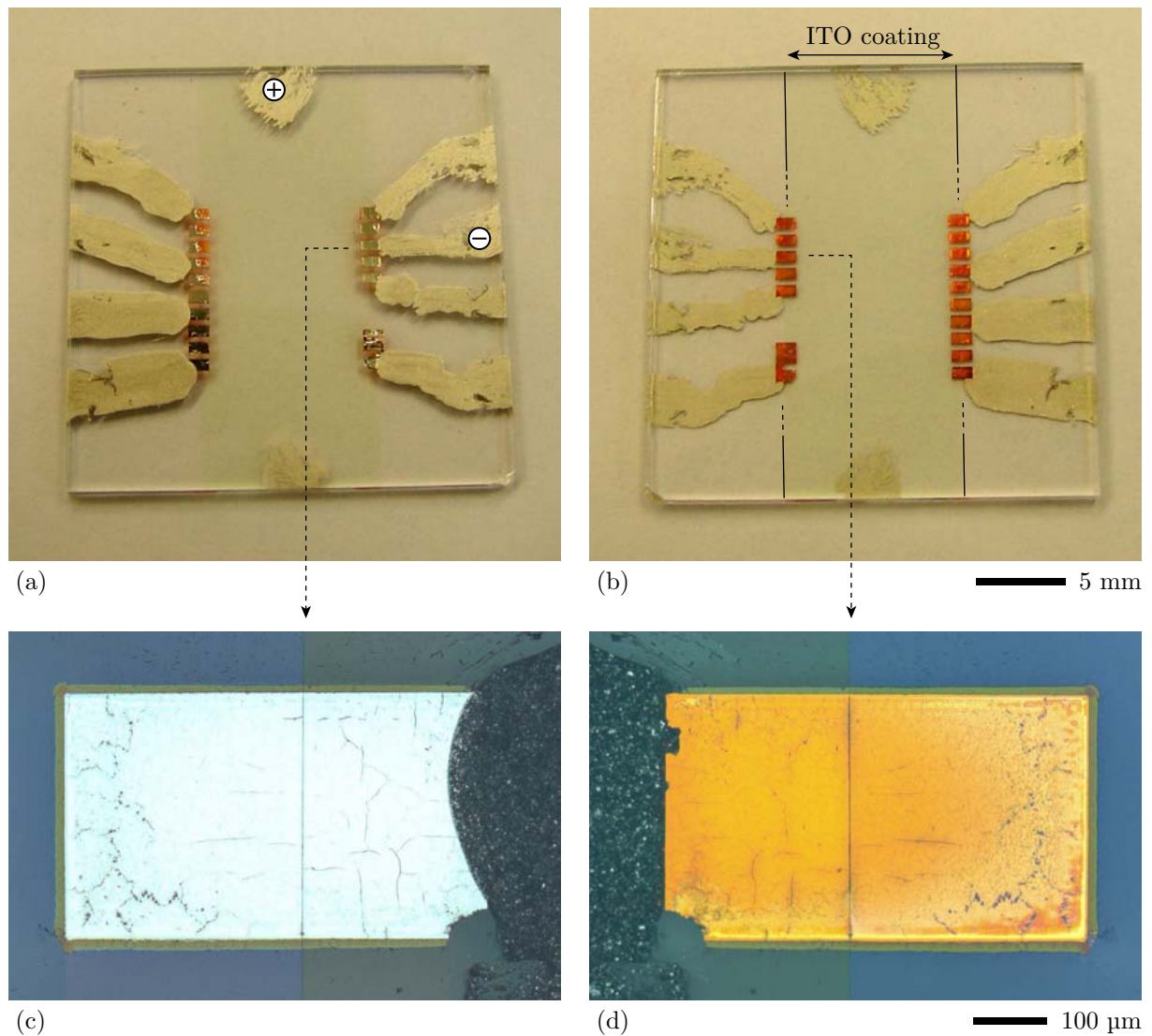
Figure 4.64 Overview of an OLED realised by laser transfer: top view (a) and bottom view (b) of the entire receiver substrate after painting of the silver paste for electrical contact (grey bands between the pixels and the edges). The central ITO-coated stripe is outlined in (b). The locations of the electrical contacts are shown in (a) by the ⊕ and ⊖ symbols. The pixel indicated by the arrows is magnified in the bottom row, where a top (c) and bottom view (d) are shown.

4.5.2   Characterisation of the pixels

A diode pixel in operation (under voltage) is shown in Figure 4.65. Other non-contacted pixels can be recognized as well on the picture. The pixel emits light, demonstrating that the device is functional after the transfer.
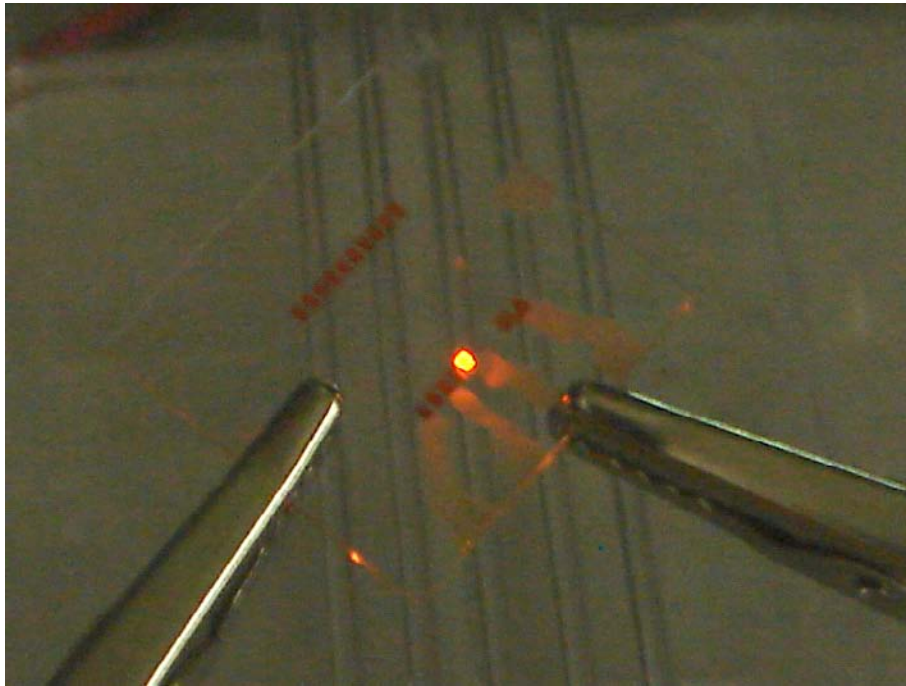
Figure 4.65 Pixel in operation under inert atmosphere. Non-contacted pixels are visible as well.

Operating devices were then characterized by current-voltage (I-V) and electroluminescence (EL) measurements. Figure 4.66 (a) presents a typical current-voltage curve.

The I-V curve exhibits a smooth, rectifying shape up to 16 V, which is free from short-circuit spikes, indicating that the transferred diodes are of good quality and no layer mixing occurs upon transfer.

Simultaneous I-V and EL measurements were also carried out. The luminance-current characteristics are linear, which is a typical diode behaviour (see Figure 4.66 b). A luminance of 6 cd/m^2 was measured at 14 V. This value is not very high and reflects the yet unoptimized device architecture. In particular, the high current and high light onset voltage are due to the poor electron injection at the aluminum cathode as well as the rather thick MEH-PPV layer which limits charge transport. The luminous efficiency at 14 V of $2 \cdot 10^{-2}$ cd/A is typical of simple MEH-PPV light-emitting diodes using a simple Al cathode [123]. However, the choice of this device architecture offers the advantage of being well characterized in the literature.

Most importantly, the MEH-PPV emission spectrum depends strongly on thermal annealing [124], which permits the assessment of possible heating effects occurring during laser transfer. Photoluminescence (PL) and EL spectra are presented in Figure 4.67.
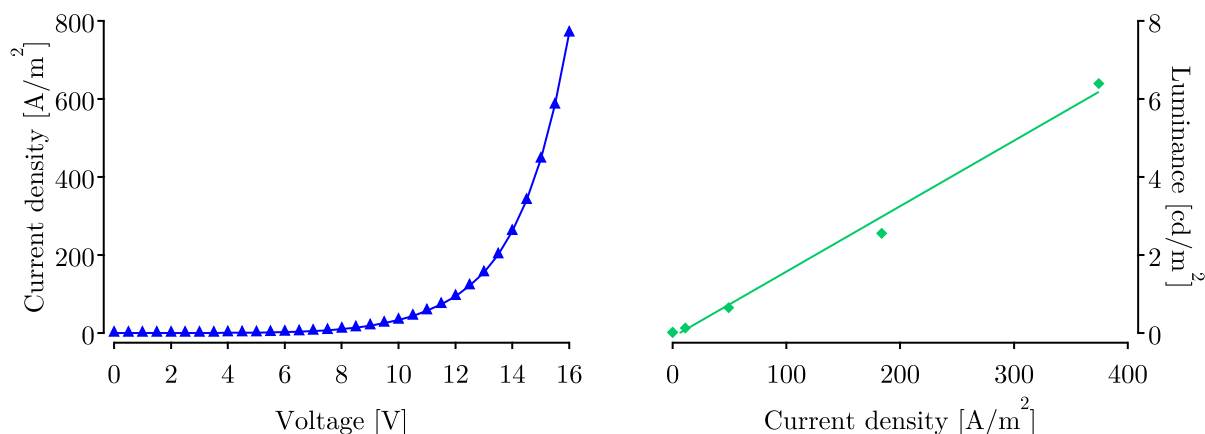
Figure 4.66 (a) Current-voltage curve of a typical pixel device. (b) Electroluminescence intensity (luminance) versus current density (from another sample).
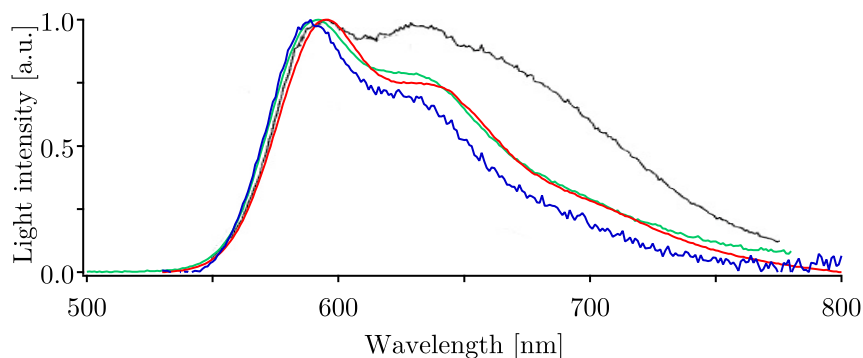
Figure 4.67 Photoluminescence spectra of a donor film (red) and a transferred pixel (blue), and electroluminescence spectrum of the same pixel (green). Photoluminescence spectrum of an annealed MEH-PPV film (black, from [124]). All curves are normalised.

The PL spectra were taken from both a donor film and a transferred pixel, which was also used for measuring the EL. The vibronic structure of the spectrum is characteristic of the interchain packing of the polymer and origins from the aggregation state of the polymer in the spin coating solution [124]. If annealed, the emission spectrum of the film exhibits a very broad red-shifted peak at 650 nm with poor emission efficiency. No such peak is observed neither in the EL nor in the PL spectrum of the transferred pixel. The recombination and EL emission zone is very close to the aluminum cathode due to poor electron injection in the single layer devices. The EL spectrum is therefore particularly sensitive to structural changes occurring in the vicinity of the aluminum electrode. The fact that both PL and EL spectra of the pixel are similar suggests that the thermal load during laser transfer is very limited.

Chapter 5

Conclusions

The goal of this work was to develop and study a transfer technique that allows to achieve patterned multi-layer deposition of sensitive materials. The investigation of the process required a systematic study of the different aspects involved, which are the ablation of the sacrificial layer, the ejection and flight of the material flyer, the deposition of this flyer onto a receiver substrate, and finally the characterisation of the OLED pixels created with the technique. The major findings in the different aspects of this work and their implications are presented below.

5.1   Ablation of the sacrificial layer

Ablation of the sacrificial triazene polymer (TP) layer is the driving force of the transfer. It is therefore of primary importance to understand the ablation behaviour of the polymer quantitatively. The analysis of the ablation threshold of very thin polymer layers was carried out for the first time in this work. A dramatic increase of the ablation threshold fluence for decreasing film thicknesses was found for films thinner than 50 nm, which could be explained by a model combining thermal and optical effects. The modelling revealed that the ablation threshold strongly depends on heat diffusion into the substrate and the reduced light absorption for films thinner than the penetration depth of the laser light. This effect was confirmed by testing substrates with different thermal conductivities and laser pulses with different durations.

This effect is also observed for material delamination upon back side ablation, where a strong increase of the delamination fluence is detected with samples containing a very thin TP layer. The lower limit of the triazene thickness required for efficient material transfer is around 100 nm.

Laser ablation of the sacrifical layer was investigated also for back side ablation, i.e. with the laser beam arriving through the substrate at the polymer film, which is also the configuration used for laser-induced forward transfer (LIFT). The investigations showed that partial ablation occurs, revealed by an undecomposed triazene polymer skin layer which is visible on the ablation spot. This skin layer is observed when the fluence is not

sufficient to decompose the complete layer. Time-resolved shadowgraphy was used for lateral imaging of the back side ablation process. A shock wave and the ejection of a flyer of undecomposed TP were observed. The flyer is created at fluences just above the threshold for delamination, while no flyer is observed and the complete triazene layer is decomposed at very high fluences.

An energy balance for the ablation of the triazene was calculated form the measured trajectories of the shock wave and flyer. The analysis shows that a large part of the energy is used to generate the shock wave, although a considerable part is lost into thermal and mechanical processes. A pronounced difference for the energy of the shock wave generated upon front side and back side irradiation was observed when a triazene polymer flyer was present. The kinetic energy of the flyer itself cannot account for that difference, because its amount represents only a marginal part of the total energy. However, the undecomposed material that forms the flyer has an effect on the creation and/or propagation of the shock wave, which travels through that remaining polymer film prior to propagate in air.

A more detailed energy calculation can be achieved by including the mechanical energy required to detach the flyer from the film. Further calculations are currently in progress to understand the process of flyer creation in more detail.

5.2   Mechanisms of the transfer

The formation of a material flyer from a donor film and its ejection and deposition onto a receiver substrate were investigated systematically to understand the conditions required to obtain a good material transfer. The effects of the laser fluence, triazene film thickness, separation distance, background pressure and donor material are summarised below.

The ejection of a material flyer from an aluminum donor film was investigated by time-resolved shadowgraphy. The flyer is in a good state over a relatively large distance (500 µm), suggesting that it can be collected onto a receiver substrate. The conditions required to create a "good" material flyer correspond to fluences where an undecomposed layer of TP should be a part of the flyer. The presence of this remaining triazene polymer layer probably stabilises the flyer mechanically by forming a kind of composite film. A thick initial TP layer produces therefore the best flyer, while an early flyer desintegration is observed for a thin triazene polymer layer. This suggests that it may be difficult to achieve a transfer with a complete removal of the sacrificial layer, i.e. of the TP. This may be a problem, because one goal of the technique is to achieve a multi-layer deposition from the successive transfer of several layers, which requires a complete removal of the sacrifical layer from the transferred layer.

An intermediate fluence is required to produce a "good" flyer, because too high fluences result in the desintegration of the flyer, while too low fluences do not produce a well-defined delamination of the flyer, which again results in an early desintegration.

The creation of a shock wave was also observed and its influence on the transfer was investigated by time-resolved shadowgraphy. The transfer was investigated with various separation distances between the donor and the receiver, revealing that the shock wave is reflected from the receiver substrate. This is a problem for the transfer with small distance because the reflected shock wave destroys the flyer. For large distances the flyer falls apart before reaching the receiver.

One possible solution to the problem caused by the reflected shock wave is to perform the transfer is vacuum, where no shock wave is propagating. The flyer is in this case not slowed down by air and reaches a velocity of up to 2 km/s at the arrival on the receiver, which is for example twice as fast as the initial velocity of a rifle bullet. Under these conditions, the flyer is instantaneously destroyed upon impact on the receiver, suggesting that a transfer in vacuum is not suitable for achieving a smooth deposition.

There is an apparent predicament as vacuum may be needed to avoid the destructive shock wave and air is required to decelerate the flyer. The solution to this problem may be found in between, i.e. with the application of an intermediate pressure between vacuum and ambient, or by employing other gases in which the propagation of the shock wave is different. The receiver hardness may be another tunable parameter to improve the transfer with a gap.

The use of a bilayer donor film made of aluminum and the luminescent polymer MEH-PPV revealed an improved stability of the flyer upon ejection. This effect is most probably due to the additional polymer layer, which improves the mechanical stability of the flyer. The best flyer was detected when an undecomposed layer of the TP should be present as well. This suggests that the metal layer is stabilised between the two polymer layers, which seems to be the optimum situation for a stable metal flyer.

A fairly good pixel deposition has been obtained with this system with a 1 mm gap in air, although not yet with a quality sufficient to build an OLED. Nevertheless, these results are very promising and suggest that it may be possible to achieve a transfer across a gap by optimising the parameters that can control the flyer velocity, in-flight shape, and stability. These parameters include the background gas and pressure, but also the separation distance, the donor film materials and maybe the material of the receiver substrate.

Although the transfer of pixels across a gap is desirable for possible industrial applications, we could show that the transfer in contact is easier to achieve than across a gap, certainely due to the fact that the flyer cannot be deformed. The transfer of an intact Al/MEH-PPV pixel was achieved with this approach.

The influence of the laser pulse duration and energy profile on the transfer was studied as well. The application of the inhomogeneous beam of a solid-state picosecond laser is not adequate for the transfer because the material ejection as well as the pattern transfer in contact mode do not occur homogeneously. However, the partial OLED pixels that have been transferred so far were obtained at much lower fluences than with the excimer

laser and reveal a smooth and crack-free surface. This suggests that a homogenised ps 355 nm laser beam may be a very promising way for LIFT and further investigations are carried out.

5.3 Application to OLED transfer

The first transfer of functional OLED pixels using a LIFT technique could be demonstrated for the transfer in contact of an Al/MEH-PPV layer using the 308 nm irradiation of a sacrifical TP layer. The characterisation of the transferred pixels by luminance and emission spectroscopy revealed the same characteristics as a similar device made by well-established techniques. The fact that sensitive materials such as MEH-PPV can be transferred without altering the functional properties proves that the LIFT technique with a triazene polymer as sacrificial layer is very well suited to the transfer of sensitive materials. This work suggests that an industrial developement of a new technique for the deposition of OLED pixels may be possible.

The application of this new technique has raised interest in the laser transfer community, and during this work, collaborations with other groups have shown the benefit of using the triazene polymer as sacrificial layer for LIFT with the transfer of micrometer-size ceramic patterns [106]. The transfer of sensor polymers is currently under investigation and shows very promising results as well. In the meantime, the transfer of nanocrystal quantum dots [125] and living mammalian cells embedded in a matrix [126] was demonstrated as well, showing very promising perspectives for the the LIFT technique based on triazene polymers as sacrificial layer.

5.4 Outlook

The next steps in this project may include the testing of state-of-the-art luminescent materials and device achitectures, which should confirm the applicability of the LIFT technique for an industrial developement. As a matter of fact some companies have already shown their interest.

The successive transfer of single layers to achieve a multi-layer pattern is also an important goal and must be investigated in more detail. An undecomposed layer of the triazene polymer may be a problem and may require a careful analysis of the residues on the transferred pixel. An investigation of the smallest feature size that can be deposited is of interest as well.

The developement of new triazene polymers which are soluble in polar solvents is now required to coat the electroactive materials directly on the triazene polymer layer and test the transfer without the metal layer. Additionally, an important improvement of the experimental setup will be the application of time-resolved front side imaging, which

will help to follow the flyer evolution and complete the information obtained by lateral imaging. This type of setup is currently being realised.

Bibliography

[1] T. A. Skotheim, R. L. Elsenbaumer, and J. R. Reynolds, *Handbook of conducting polymers*, Dekker, New York, 2nd edition, 1998.

[2] A. J. Heeger, Angew. Chem. **40**, 2591 (2001).

[3] R. Christie, *Colour chemistry*, Royal Society of Chemistry, Cambridge, 2007.

[4] T. James, *The theory of the photographic processes*, Macmillan, New York, 4th edition, 1977.

[5] M. Pope and C. E. Swenberg, *Electronic Processes in Organic Crystals and Polymers*, Monographs on the Physics and Chemistry of Materials, Oxford University Press, 2nd edition, 1999.

[6] H. S. Nalwa, *Charge-transfer salts, fullerenes and photoconductors*, Wiley, Chichester, 1997.

[7] J. Kovac, L. Peternai, and O. Lengyel, Thin Solid Films **433**, 22 (2003).

[8] C. W. Tang and S. A. VanSlyke, Appl. Phys. Lett. **51**, 913 (1987).

[9] J. Burroughes, D. Bradley, A. Brown, R. Marks, K. MacKay, R. Friend, P. Burns, and A. Holmes, Nature **347**, 539 (1990).

[10] R. Friend, R. W. Gymer, A. B. Holmes, J. Burroughes, R. N. Marks, C. Taliani, D. Bradley, D. A. Dos Santos, J. L. Bredas, M. Logdlund, and W. R. Salaneck, Nature **397**, 121 (1999).

[11] H. Hoppe and N. S. Sariciftci, J. Mater. Res. **19**, 1924 (2004).

[12] S. Sze, *Physics of Semiconductor Devices*, John Wiley and Sons, New York, 2nd edition, 1981.

[13] G. Horowitz, J. Mater. Res. **19**, 1946 (2004).

[14] D. A. Pardo, G. E. Jabbour, and N. Peyghambarian, Adv. Mater. **12**, 1249 (2000).

[15] G. E. Jabbour, R. Radspinner, and N. Peyghambarian, IEEE J. Selected Topics in QE **7**, 769 (2001).

[16] C. Müller, A. Falcou, N. Reckefuss, M. Rojahn, V. Wiederhirn, P. Rudati, H. Frohne, O. Nuyken, H. Becker, and K. Meerholz, Nature **421**, 829 (2003).

[17] M. Wolk, J. Baezold, E. Bellmann, T. R. Hoffend Jr., S. Lamansky, Y. Li, R. R. Roberts, V. Savvateev, J. S. Staral, and W. A. Tolbert, Proc. SPIE **5519**, 12 (2004).

[18] T. H. Maiman, Nature **187**, 493 (1960).

[19] P. L. Bender, D. G. Currie, R. H. Dicke, D. H. Eckhardt, J. E. Faller, W. M. Kaula, J. D. Mulholland, H. H. Plotkin, S. K. Poultney, E. C. Silverberg, D. T. Wilkinson, J. G. Williams, and C. O. Alley, Science **182**, 229 (1973).

[20] A. Rüdiger, Nuclear Physics B - Proceedings Supplements **48**, 96 (1996).

[21] M. W. Sigrist, R. Bartlome, D. Marinov, J. M. Rey, D. E. Vogler, and H. Wächter, Appl. Phys. B **90**, 289 (2008).

[22] G. Sansone, E. Benedetti, F. Calegari, C. Vozzi, L. Avaldi, R. Flammini, L. Poletto, P. Villoresi, C. Altucci, R. Velotta, S. Stagira, S. De Silvestri, and M. Nisoli, Science **314**, 443 (2006), 10.1126/science.1132838.

[23] D. Bäuerle, *Laser Processing and Chemistry*, Springer, Berlin, 3rd edition, 2000.

[24] A. Schawlow, Science **149**, 13 (1965).

[25] R. Srinivasan and V. Mayne-Banton, Appl. Phys. Lett. **41**, 576 (1982).

[26] Y. Kawamura, K. Toyoda, and S. Namba, Appl. Phys. Lett. **40**, 374 (1982).

[27] T. Lippert, A. Wokaun, J. Stebani, O. Nuyken, and J. Ihlemann, Angew. Makromol. Chem. **206**, 97 (1993).

[28] T. Lippert and J. Dickinson, Chem. Rev. **103**, 453 (2003).

[29] T. Lippert, Adv. Polym. Sci. **168**, 51 (2004).

[30] K. Suzuki, M. Matsuda, T. Ogino, N. Hayashi, T. Terabayashi, and K. Amemiya, Excimer ablation lithography (eal) for tft-lcd, in *Excimer Lasers, Optics, and Applications*, volume 2992, pages 98–107, San Jose, CA, USA, 1997, SPIE.

[31] N. Hayashi, K. Suzuki, M. Matsuda, T. Ogino, and Y. Tomita, Polyurethane resins as resist materials for excimer ablation lithography (eal), in *Excimer Lasers, Optics, and Applications*, volume 2992, pages 129–134, San Jose, CA, USA, 1997, SPIE.

[32] N. M. Bityurin, B. Luk'yanchuk, M. Hong, and T. Chong, Chem. Rev. **103**, 519 (2003).

[33] S. Anisimov and B. Luk'yanchuk, Phys. Usp. **45**, 293 (2002).

[34] M. Prasad, P. F. Conforti, and B. J. Garisson, J. Appl. Phys. **101**, 103113 (2007).

[35] N. Mansour and K. Jamshidi-Ghaleh, J. Phys. D: Appl. Phys. **38**, 852 (2005).

[36] M. Castex and N. M. Bityurin, Appl. Surf. Sci. **197-198**, 805 (2002).

[37] H. Schmidt, J. Ihlemann, B. Wolff-Rottke, K. Luther, and J. Troe, J. Appl. Phys. **83**, 5458 (1998).

[38] G. Pettit and R. Sauerbrey, Appl. Phys. A **56**, 51 (1993).

[39] G. Pettit, M. Ediger, D. Hahn, B. Brinson, and R. Sauerbrey, Appl. Phys. A **58**, 573 (1994).

[40] T. Lippert, L. Bennett, T. Nakamura, H. Niino, A. Ouchi, and A. Yabe, Appl. Phys. A **63**, 257 (1996).

[41] S. Küper and M. Stuke, Appl. Phys. A **49**, 211 (1989).

[42] R. Srinivasan, B. Braren, and K. Casey, J. Appl. Phys. **68**, 1842 (1990).

[43] M. Hauer, D. J. Funk, T. Lippert, and A. Wokaun, Appl. Surf. Sci. **208**, 107 (2003).

[44] N. Bityurin, Appl. Surf. Sci. **138-139**, 354 (1999).

[45] G. Bounos, A. Selimis, S. Georgiou, E. Rebollar, M. Castillejo, and N. M. Bityurin, J. Appl. Phys. **100**, 114323 (2006).

[46] N. M. Bityurin, Proc. SPIE **4423**, 197 (2001).

[47] N. Arnold, N. M. Bityurin, and D. Bäuerle, Appl. Surf. Sci. **138-139**, 212 (1999).

[48] N. M. Bityurin, N. Arnold, B. Luk'yanchuk, and D. Bäuerle, Appl. Surf. Sci. **127-129**, 164 (1998).

[49] B. Luk'yanchuk, N. M. Bityurin, S. Anisimov, A. Y. Malyshev, N. Arnold, and D. Bäuerle, Appl. Surf. Sci. **106**, 120 (1996).

[50] N. Arnold and N. Bityurin, Appl. Phys. A **68**, 615 (1999).

[51] C. Latkoczy and D. Günther, J. Anal. At. Spectrom. **17**, 1264 (2002).

[52] J. Koch, M. Wälle, J. Pisonero, and D. Günther, J. Anal. At. Spectrom. **21**, 932 (2006).

[53] M. Tanner and D. Günther, J. Anal. At. Spectrom. **21**, 941 (2006).

[54] P. R. Willmott, Appl. Phys. A **69**, 437 (1999).

[55] V. S. Ban and D. A. Kramer, J. Mater. Sci. **5**, 978 (1970).

[56] S. Hansen and T. Robitaille, Appl. Phys. Lett. **50**, 359 (1987).

[57] D. H. Lowndes, D. B. Geohegan, A. A. Puretzky, D. P. Norton, and C. M. Rouleau, Science **273**, 898 (1996).

[58] N. Matsumoto, H. Shima, T. Fujii, and F. Kannari, Appl. Phys. Lett. **71**, 2469 (1997).

[59] X. Yang, Y. Tang, M. Yu, and Q. Qin, Thin Solid Films **358**, 187 (2000).

[60] G. Blanchet, Macromolecules **28**, 4603 (1995).

[61] D. Chrisey, A. Piqué, R. McGill, J. Horwitz, B. Ringeisen, D. Bubb, and P. Wu, Chem. Rev. **103**, 553 (2003).

[62] D. Chrisey, A. Piqué, J. Fitz-Gerald, R. Auyeung, R. McGill, H. Wu, and M. Duignan, Appl. Surf. Sci. **154-155**, 593 (2000).

[63] B. Toftmann, M. R. Papantonakis, R. C. Y. Auyeung, W. Kim, S. M. O'Malley, D. M. Bubb, J. S. Horwitz, J. Schou, P. M. Johansen, and R. F. Haglund, Thin Solid Films **453-454**, 177 (2004).

[64] S. Johnson, C. Bowie, B. Ivanov, H. Park, and R. Haglund Jr., Proc. SPIE **6486**, 64860G (2007).

[65] S. L. Johnson, H. K. Park, and R. F. Haglund Jr, Appl. Surf. Sci. **253**, 6430 (2007).

[66] K. Kyrkis, A. Andreadaki, D. Papazoglou, and I. Zergioti, Direct transfer and microprinting of functional materials by laser-induced forward transfer, in *Recent Advances in Laser Processing of Materials*, edited by J. Perrière, E. Millon, and E. Fogarassy, volume 241, pages 213–241, Elsevier, Amsterdam, 2006.

[67] C. Arnold, P. Serra, and A. Piqué, MRS Bull. **32**, 23 (2007).

[68] J. Bohandy, B. F. Kim, and F. J. Adrian, J. Appl. Phys. **60**, 1538 (1986).

[69] H. Esrom, J. Zhang, U. Kogelschatz, and A. Pedraza, Appl. Surf. Sci. **86**, 202 (1995).

[70] I. Zergioti, S. Mailis, N. Vainos, C. Fotakis, S. Chen, and C. Grigoropoulos, Appl. Surf. Sci. **127-129**, 601 (1998).

[71] H. Yamada, T. Sano, T. Nakayama, and I. Miyamoto, Appl. Surf. Sci. **197-198**, 411 (2002).

[72] D. P. Banks, C. Grivas, J. D. Mills, R. W. Eason, and I. Zergioti, Appl. Phys. Lett. **89**, 193107 (2006).

[73] R. Wartena, A. Curtright, C. Arnold, A. Piqué, and K. Swider-Lyons, J. Power Sources **126**, 193 (2004).

[74] P. Serra, J. Fernández-Pradas, F. Berthet, M. Colina, J. Elvira, and J. Morenza, Appl. Phys. A **79**, 949 (2004).

[75] A. Piqué, D. Chrisey, R. Auyeung, J. Fitz-Gerald, H. Wu, R. McGill, S. Lakeou, P. Wu, V. Nguyen, and M. Duignan, Appl. Phys. A **69**, S279 (1999).

[76] B. Ringeisen, D. Chrisey, A. Piqué, H. Young, R. Modi, M. Bucaro, J. Jones-Meehan, and B. Spargo, Biomaterials **23**, 161 (2002).

[77] W. A. Tolbert, I.-Y. Sandy Lee, M. M. Doxtader, E. W. Ellis, and D. D. Dlott, J. Imaging Sci. Technol. **37**, 411 (1993).

[78] J. Fernández-Pradas, M. Colina, P. Serra, J. Domínguez, and J. Morenza, Thin Solid Films **453-454**, 27 (2004).

[79] T. Smausz, B. Hopp, G. Kecskeméti, and Z. Bor, Appl. Surf. Sci. **252**, 4738 (2006).

[80] S. G. Koulikov and D. D. Dlott, J. Imaging Sci. Technol. **44**, 111 (2000).

[81] N. T. Kattamis, P. E. Purnick, R. Weiss, and C. B. Arnold, Appl. Phys. Lett. **91**, 171120 (2007).

[82] T. Mito, T. Tsujita, H. Masuhara, N. Hayashi, and K. Suzuki, Jpn. J. Appl. Phys., Part 2 **40**, L805 (2001).

[83] D. Karnakis, T. Lippert, N. Ichinose, S. Kawanishi, and H. Fukumura, Appl. Surf. Sci. **127-129**, 781 (1998).

[84] T. Lippert, A. Wokaun, S. Langford, and J. Dickinson, Appl. Phys. A **69**, 655 (1999).

[85] T. Lippert, S. Langford, A. Wokaun, S. Georgiou, and J. Dickinson, J. Appl. Phys. **86**, 7116 (1999).

[86] T. Lippert, C. David, J. Dickinson, M. Hauer, U. Kogelschatz, S. Langford, O. Nuyken, C. Phipps, J. Robert, and A. Wokaun, J. Photochem. Photobiol. A **145**, 145 (2001).

[87] L. Bennett, T. Lippert, H. Furutani, H. Fukumura, and H. Masuhara, Appl. Phys. A **63**, 327 (1996).

[88] M. Nagel, R. Hany, T. Lippert, M. Molberg, F. Nüesch, and D. Rentsch, Macromol. Chem. Phys. **208**, 277 (2007).

[89] A. V. Finkelstein and O. B. Ptitsyn, *Protein physics : A course of lectures*, Soft condensed matter complex fluids and biomaterials, Academic Press, Amsterdam, 2002.

[90] G. Settles, *Schlieren and shadowgraphy techniques: visualizing phenomena in transparent media*, Springer-Verlag, Berlin, 2001.

[91] R. Fardel, M. Nagel, F. Nüesch, T. Lippert, A. Wokaun, and B. Luk'yanchuk, Appl. Phys. A **90**, 661 (2008).

[92] L. Landau and E. Lifshitz, *Electrodynamics of Continuous Media*, Butterworth-Heinemann, Ofxord, 1984.

[93] Y. Ben-Eliahu, Y. Haas, and S. Welner, J. Phys. Chem. **99**, 6010 (1995).

[94] D. A. Freiwald, J. Appl. Phys. **43**, 2224 (1972).

[95] D. A. Freiwald and R. A. Axford, J. Appl. Phys. **46**, 1171 (1975).

[96] R. Fardel, P. Feurer, T. Lippert, M. Nagel, F. Nüesch, and A. Wokaun, Appl. Surf. Sci. **254**, 1332 (2007).

[97] T. Lippert, C. David, M. Hauer, T. Masubuchi, H. Masuhara, K. Nomura, O. Nuyken, C. Phipps, J. Robert, T. Tada, K. Tomita, and A. Wokaun, Appl. Surf. Sci. **186**, 14 (2002).

[98] Z. Ball, T. Feurer, D. L. Callahan, and R. Sauerbrey, Appl. Phys. A **62**, 203 (1996).

[99] R. Srinivasan, E. Sutcliffe, and B. Braren, Appl. Phys. Lett. **51**, 1285 (1987).

[100] A. Costela, J. M. Figuera, F. Florido, I. García-Moreno, E. P. Collar, and R. Sastre, Appl. Phys. A **60**, 261 (1995).

[101] G. Daminelli, S. Pentzien, A. Hertwig, and J. Krüger, Appl. Phys. A **83**, 89 (2005).

[102] N. M. Bityurin, Annu. Rep. Prog. Chem., Sect. C, Phys. Chem. **101**, 216 (2005).

[103] K. Hatanaka, M. Kawao, Y. Tsuboi, and H. Fukumura, J. Appl. Phys. **82**, 5799 (1997).

[104] M. Nagel, R. Fardel, P. Feurer, M. Häberli, F. Nüesch, T. Lippert, and A. Wokaun, Appl. Phys. A **92**, 781 (2008).

[105] F. Zimmermann, T. Lippert, C. Beyer, J. Stebani, O. Nuyken, and A. Wokaun, Appl. Spectrosc. **47**, 986 (1993).

[106] D. P. Banks, K. Kaur, R. Gazia, R. Fardel, M. Nagel, T. Lippert, and R. W. Eason, EPL **83**, 38003 (2008), 0295-5075.

[107] J. Bonse, J. Solis, L. Urech, T. Lippert, and A. Wokaun, Appl. Surf. Sci. **253**, 7787 (2007).

[108] R. Fardel, M. Nagel, F. Nüesch, T. Lippert, and A. Wokaun, Appl. Surf. Sci. **255**, 5430 (2009).

[109] Y. B. Zel'dovich and Y. P. Raizer, *Physics of shock waves and high-temperature hydrodynamic phenomena*, Dover Publications, Mineola, N.Y, 2002.

[110] M. Ohkoshi, T. Yoshitake, and K. Tsushima, Appl. Phys. Lett. **64**, 3340 (1994).

[111] J. Gonzalo, C. N. Afonso, and I. Madariaga, J. Appl. Phys. **81**, 951 (1997).

[112] L. Urech, M. Hauer, T. Lippert, C. Phipps, E. Schmid, A. Wokaun, and I. Wysong, Proc. SPIE **5448**, 52 (2004).

[113] R. Fardel, M. Nagel, F. Nüesch, T. Lippert, and A. Wokaun, Appl. Surf. Sci. **254**, 1322 (2007).

[114] Y.-W. Cheng, D. T. Read, J. D. McColskey, and J. E. Wright, Thin Solid Films **484**, 426 (2005).

[115] W. Wong, M. Gupta, and C. Lim, Materials Science and Engineering, A: Structural Materials: Properties, Microstructure and Processing **423**, 148 (2006).

[116] A. Tsou, J. Hord, G. Smith, and R. Schrader, Polymer **33**, 2970 (1992).

[117] I. Yakimets, N. Wellner, A. C. Smith, H. Wilson, Reginlad, I. Farhat, and J. Mitchell, Polymer **46**, 12577 (2005).

[118] C.-A. Dai and M.-W. Liu, Materials Science and Engineering, A: Structural Materials: Properties, Microstructure and Processing **423**, 121 (2006).

[119] N. Cao, Y. Fu, and J. He, Food Hydrocolloids **21**, 575 (2007).

[120] M. A. García, A. Pinotti, M. N. Martino, and N. E. Zaritzky, Carbohydr. Polym. **56**, 339 (2004).

[121] F. Debeaufort and A. Voilley, J. Agric. Food Chem. **45**, 685 (1997).

[122] R. Fardel, M. Nagel, F. Nüesch, T. Lippert, and A. Wokaun, Appl. Phys. Lett. **91**, 061103 (2007).

[123] T. F. Guo, F. S. Yang, Z. J. Tsai, T. C. Wen, S. N. Hsieh, and Y. S. Fu, Appl. Phys. Lett. **87**, 013504 (2005).

[124] T. Q. Nguyen, I. B. Martini, J. Liu, and B. J. Schwartz, J. Phys. Chem. B **104**, 237 (2000).

[125] J. Xu, J. Liu, D. Cui, M. Gerhold, A. Y. Wang, M. Nagel, and T. K. Lippert, Nanotechnology **18**, 025403 (2007).

[126] A. Doraiswamy, R. Narayan, T. Lippert, L. Urech, A. Wokaun, M. Nagel, B. Hopp, M. Dinescu, R. Modi, R. Auyeung, and D. Chrisey, Appl. Surf. Sci. **252**, 4743 (2006).

Nomenclature

Acronyms

ETL	electron transporting layer
FEL	free electron laser
FWHM	full width at half maximum
HOMO	highest occupied molecular orbital
HTL	hole transporting layer
ICCD	intensified charge-coupled device
IR	infrared
ITO	tin-doped indium oxide
LCD	liquid crystal display
LED	light emitting diode
LIFT	laser-induced forward transfer
LITI	laser-induced thermal imaging
LUMO	lowest unoccupied molecular orbital
MAPLE	matrix-assisted pulsed laser evaporation
MAPLE-DW	matrix-assisted pulsed laser evaporation direct write
Nd:YAG	neodymium-doped yttrium aluminum garnet
OLED	organic light emitting diode
PLD	pulsed laser deposition
PLED	polymer light emitting diode
PMMA	polymethyl methacrylate
TP	triazene polymer
UV	ultraviolet

Symbols

a	decadic linear absorption coefficient
A	ablation spot area
c	speed of light in vacuum
C_4, C_5	fit constants of the shock wave equation

d	ablated depth
E	energy
F	spatial distribution of the absorbed laser intensity
g	temporal distribution of the laser intensity
h	Planck constant
h	film thickness
k	extinction coefficient
M_n	molar mass
n	refractive index
p	Laplace space variable
q	normalised spatial distribution of the absorbed laser intensity
Q	distribution of the absorbed laser intensity
r	reflection coefficient
R	reflectivity
t	time
t_0	apparent delay of the shock wave origin
t_{FWHM}	laser pulse duration
t_l	characteristic pulse duration
T	transmittance
T	temperature
$T_{\max}$	peak temperature
T_0	peak temperature at infinite film thickness
$\tilde{T}$	Lapace transform of the temperature
U	voltage
U_D	driving voltage
U_G	date voltage
v	velocity
x, z	distance across the sample

α	natural linear absorption coefficient
α_{eff}	effective absorption coefficient
γ	adiabatic ratio
$\Delta_{\mathrm{dec}} H$	decomposition enthalpy
ϵ	dielectric permittivity
η	normalised energy
κ	thermal conductivity
λ	wavelength

ρ density

ρ_E energy density

Φ fluence

Φ_{th} threshold fluence

Φ_0 incident fluence

χ thermal diffusivity

Indices

dec   decompostion

f   film

fs   film/substrate boundary

g   gas

m   medium

mf   medium/film boundary

s   substrate

Curriculum vitae

Personal

Romain Fardel, born on 10th May 1982 in Yverdon-les-Bains (Switzerland)
Swiss, citizen of Mutrux (VD)

Education

2005 – 2009	PhD thesis at ETH Zurich, under the direction of Prof. Alexander Wokaun
	◇ "Laser-Induced Forward Transfer for the Fabrication of Patterned Organic Light-Emitting Diodes"
	◇ work carried out at Empa, Laboratory for Functional Polymers (supervisor Dr Frank Nüesch) and Paul Scherrer Institut, Materials Group in the General Energy Research Department (supervisor PD Dr Thomas Lippert)
2000 – 2005	Master of Science in Chemical and biological engineering at the Swiss Federal Institute of Technology (EPFL), Lausanne
	◇ diploma work in electrochemical synthesis carried out at BASF, Ludwigshafen (D)
1997 – 2000	Federal maturity, scientific type Gymnase d'Yverdon (VD)

Publications

Publications as first author

○ R. Fardel, M. Nagel, F. Nüesch, T. Lippert and A. Wokaun, Fabrication of organic light-emitting diode pixels by laser-assisted forward transfer, *Applied Physics Letters* **91**, 061103 (2007).

○ R. Fardel, M. Nagel, F. Nüesch, T. Lippert, A. Wokaun and B. Luk'yanchuk, Infuence of thermal diffusion on the laser ablation of thin polymer films, *Applied Physics A* **90**, 661–667 (2008).

○ R. Fardel, L. Urech, T. Lippert, C. Phipps, J. Fitz-Gerald and A. Wokaun, Laser ablation of energetic polymer solutions: effect of viscosity and fluence on the splashing behavior, *Applied Physics A* **94**, 657–665 (2009).

○ R. Fardel, M. Nagel, F. Nüesch, T. Lippert and A. Wokaun, Laser forward transfer using a sacrificial layer: Influence of the material properties, *Applied Surface Science* **254**, 1322–1326 (2007).

○ R. Fardel, P. Feurer, T. Lippert, M. Nagel, F. Nüesch and A. Wokaun, Laser ablation of aryltriazene photopolymer films: effect of polymer structure on ablation properties, *Applied Surface Science* **254**, 1332–1337 (2007).

○ R. Fardel, M. Nagel, F. Nüesch, T. Lippert and A. Wokaun, Shadowgraphy investigation of laser-induced forward transfer: front side and back side ablation of the triazene polymer sacrificial layer, *Applied Surface Science* **255**, 5430–5434 (2009).

Publications as co-author

○ M. Nagel, R. Fardel, P. Feurer, M. Häberli, F. Nüesch, T. Lippert and A. Wokaun, Aryltriazene photopolymer thin films as sacrificial release layers for laser-assisted forward transfer systems: study of photoablative decomposition and transfer behavior, *Applied Physics A* **92**, 781–789 (2008).

○ D. P. Banks, K. Kaur, R. Gazia, R. Fardel, M. Nagel, T. Lippert and R. W. Eason, Triazene photopolymer dynamic release layer-assisted femtosecond laser-induced forward transfer with an active carrier substrate, *EPL (Europhysics Letters)* **83**, 38003 (2008).

○ B. C. Seyfang, R. Fardel, T. Lippert, G. G. Scherer and A. Wokaun, Micro-patterning for polymer electrolyte fuel cells: Single pulse laser ablation of aluminum films from glassy carbon, *Applied Surface Science* **255**, 5471–5475 (2009).

○ T. Lippert, L. Urech, R. Fardel, M. Nagel, C. R. Phipps and A. Wokaun, Materials for laser propulsion: "liquid" polymers, *Proceedings of SPIE* **7005**, 700512 (2008).

In preparation

○ R. Fardel, M. Nagel, F. Nüesch, T. Lippert and A. Wokaun, Energy balance by shadowgraphy on the sacrifical layer in laser-induced forward transfer, submitted.

Conferences

Talks

- R. Fardel, M. Nagel, F. Nüesch, T. Lippert, A. Wokaun and B. Luk'yanchuk
  Influence of thickness on the laser ablation of a triazene polymer
  E-MRS 2007 Spring Meeting, 28.5–1.6.2007, Strasbourg (France)
  ⋆ Young Scientist Award for the best paper presented

- R. Fardel, M. Nagel, F. Nüesch, T. Lippert and A. Wokaun
  Shadowgraphy analysis of the laser-induced forward transfer process
  E-MRS 2008 Spring Meeting, 26–30.5.2008, Strasbourg (France)

- R. Fardel, M. Nagel, F. Nüesch, T. Lippert and A. Wokaun
  Polymer light-emitting diodes fabrication by laser-assisted forward transfer
  Plastic Electronics 08, 27-29.10.2008, Berlin (Germany)

Posters

- R. Fardel, M. Nagel, F. Nüesch, T. Lippert and A. Wokaun
  Patterned organic LED fabrication using laser-induced forward transfer
  SCS Fall Meeting 2006, 13.10.2006, Zurich

- R. Fardel, M. Nagel, F. Nüesch, T. Lippert and A. Wokaun
  Laser-induced forward transfer applied to OLED fabrication
  COLA 2007, 24–28.9.2007, Tenerife (Spain)